6-19-2014

The Scattering of Partially Coherent Electromagnetic Beam Illumination from Statistically Rough Surfaces

Mark F. Spencer

THE SCATTERING OF PARTIALLY COHERENT ELECTROMAGNETIC BEAM ILLUMINATION FROM STATISTICALLY ROUGH SURFACES

DISSERTATION

Mark F. Spencer

AFIT-ENG-DS-14-J-7

DEPARTMENT OF THE AIR FORCE
AIR UNIVERSITY

AIR FORCE INSTITUTE OF TECHNOLOGY

Wright-Patterson Air Force Base, Ohio

AFIT-ENG-DS-14-J-7

THE SCATTERING OF PARTIALLY COHERENT ELECTROMAGNETIC BEAM ILLUMINATION FROM STATISTICALLY ROUGH SURFACES

DISSERTATION

Presented to the Faculty

Graduate School of Engineering and Management

Air Force Institute of Technology

Air University

Air Education and Training Command

In Partial Fulfillment of the Requirements for the

Degree of Doctor of Philosophy

Mark F. Spencer, BS, MS

June 2014

AFIT-ENG-DS-14-J-7

THE SCATTERING OF PARTIALLY COHERENT ELECTROMAGNETIC BEAM ILLUMINATION FROM STATISTICALLY ROUGH SURFACES

DISSERTATION

Mark F. Spencer, BS, MS

Approved:

//signed//	29 April 2014
Milo W. Hyde IV, Maj, USAF, PhD (Chairman)	Date
//signed//	29 April 2014
Michael A. Marciniak, PhD (Member)	Date
//signed//	29 April 2014
Timothy W. Zens, Maj, USAF, PhD (Member)	Date
//signed//	29 April 2014
Michael J. Havrilla, PhD (Member)	Date

Accepted:

//signed//	02 May 2014
ADEDEJI B. BADIRU, PhD Dean, Graduate School of Engineering and Management	Date

Abstract

Much of the rough surface scattering theory developed to date considers only the effects of fully coherent and fully incoherent illumination in the formation of solutions—a problem studied in earnest since the late 1800's. In response, this dissertation extends the theory currently available in modeling rough surface scattering to include the effects of partially coherent illumination. Such illumination plays a pivotal role in our understanding of active-illumination systems, similar to those found in directed-energy and remote-sensing applications, which use the light scattered from distant targets for tactical purposes. Specifically, this dissertation uses the physical optics approximation (Kirchhoff boundary conditions) to determine a 3D vector solution for the far-field scattering of electromagnetic beam illumination with partial spatial coherence from statistically rough surfaces. The analysis considers three different material substrates: dielectrics, conductors, and a perfect electrical conductor. It also makes use of a Gaussian Schell-model form for the incident-field cross-spectral density matrix. In so doing, this dissertation develops closed-form expressions for the scattered field cross-spectral density matrix with two analytical forms—one applicable to smooth-to-moderately rough surfaces and the other applicable to very rough surfaces. The analysis shows that these closed-form expressions are, in general, complicated functions of both the source (size and coherence properties) and surface parameters (surface height standard deviation and correlation length). Under appropriate conditions, the analysis also compares the 3D vector solution to previously validated solutions and empirical measurements. The results show good agreement.

To all my influential teachers, you really made the difference

Acknowledgments

First and foremost, I would like to thank my dissertation advisor, Maj Hyde. He took me on as an out of department advisee and never complained once, despite the extra paperwork! Furthermore, he believed in me. His insight into my dissertation problem was the catalyst for my success, and despite the hand cramps from doing a theory-based dissertation, I am extremely grateful for all the help and advice that I received—I look forward to our future collaborations.

I would also like to thank my committee members for the time committed to this document. In particular, I would like to thank Dr. Marciniak. He was my professor for multiple optics courses at the Air Force Institute of Technology (AFIT), and I am very appreciative of his efforts. With that said, I would also like to thank Dr. Cox, Dr. DeWeerd, Dr. Hawks, Dr. Hill, and Dr. Schmidt for their teaching efforts throughout my collegiate career—my research abilities would not have grown into what they are today without their dedication to the classroom.

The support that I received from my fellow researchers, both at AFIT and abroad, cannot go without praise as well. Thank you so much to Dr. Basu, Dr. Bos, Ms. Poulin-Girard, Dr. Louthain, Dr. McCrae, Dr. Merritt, Dr. Nauyoks, Dr. Perram, Mr. Steinbock, and Capt Thornton for serving as sounding boards to an over-caffeinated graduate student. I must also thank my fellow classmates in the PhD-14 Section at AFIT. They provided the support system needed for my success. Especially the members of the PhD Outhouse—Maj Crowe, Capt Patel, Mr. Pennington, and Capt Showalter—thank you!

I would also like to thank my sponsors. My graduate career is indebted to the support I received early on from the Center for Directed Energy at AFIT. This support

includes the sponsorship of my BS thesis research in stimulated Brillouin scattering with Lt Col Russell and Lt Col Massey; my MS thesis research in adaptive optics and thermal blooming with Dr. Cusumano and Dr. Fiorino; and my Small Business Technology Transfer (STTR) research in optical phased arrays with Mr. Marker and Mr. Green of the Air Force Research Laboratory Directed Energy Directorate (AFRL/RD) and Dr. Tyler and Dr. Mann of the Optical Sciences Company. These experiences/relationships shaped me into the scientist I am today and gave me the skill set needed to take on this dissertation topic. I can honestly say that without this support, I would not have received my Science, Mathematics, and Research for Transformation (SMART) Scholarship.

The ongoing support my SMART Scholarship provides is truly awesome, and upon the completion of my doctoral studies, I am excited to work for my sponsoring facility, AFRL/RD. Working for AFRL/RD in Maui during my two SMART Internships was a phenomenal experience. I truly enjoyed my research in inverse synthetic aperture LADAR, and I would like to thank Dr. Williams, Lt Col Phillips, and my SMART Mentor and friend, Capt Pellizzari, for the time they spent mentoring a young scientist.

Lastly, I would like to thank SPIE, the International Society for Optics and Photonics, and the Directed Energy Professional Society for their financial support in the form of additional scholarships. I would also like to thank the Air Force Office for Scientific Research for their financial support in the form of a research grant. This support of my graduate education/research was much appreciated and I look forward to long-lasting relationships with each organization.

For all the support that I received, I am extremely grateful.

Mark F. Spencer

Table of Contents

Page

List of Figures

Page

THE SCATTERING OF PARTIALLY COHERENT ELECTROMAGNETIC BEAM ILLUMINATION FROM STATISTICALLY ROUGH SURFACES

1 Introduction

In 1960, Theodore Maiman invented the first working laser [1], which originally boasted only a few milliwatts of power. Yet, by the 1970s, laser powers reached the megawatt level and the directed-energy (DE) research community came to life [2]. The technology found in DE applications is inspiring in that it presents game-changing capabilities by offering systems with varying lethality, speed-of-light delivery, and unparalleled precision [3-5]. With this in mind, the analysis presented in this dissertation hopes to aid the burgeoning DE research community and bring us one step closer to fielding an operational system [6, 7].

1.1 Problem statement

When using active-illumination systems, more often than not a highly coherent laser beam propagates from the source through the atmosphere resulting in partially coherent beam illumination on the target. This topic plays a key role in DE and remote-sensing applications which use the light scattered from distant targets for tactical purposes [8, 9]. Interestingly enough, not much literature exists pertaining to the scattering of partially coherent light from rough surfaces.

In an effort to bridge this gap, recent publications derived a 2D scalar-equivalent solution for the scattering of partially coherent beams from statistically rough surfaces

using the physical-optics (PO) approximation (Kirchhoff boundary conditions) [10, 11]. Specifically, the analysis made use of a Gaussian Schell-model (GSM) form in creating the incident field cross-spectral density function (CSDF). This allows one to vary the size and spatial coherence properties of the incident radiation. In so doing, the analysis developed closed-form expressions for the scattered field CSDF to observe the size and spatial coherence properties of the scattered radiation in the far field. The analysis also validated these analytical expressions through computational simulations and showed good agreement between the theoretical predictions and the numerical results.

While the 2D scalar-equivalent solution is a convenient tool for gaining insight into rough surface scattering, a complete understanding of the problem requires a 3D vector solution. With that said, this dissertation makes use of the PO approximation to determine a 3D vector solution for the far-field scattering of electromagnetic beam illumination with partial spatial coherence from statistically rough surfaces. By formulating the analysis in a manner consistent with Wolf's unified theory of coherence and polarization [12, 13], all physical implications inherent in Wolf's work apply here.

The 3D vector solution developed in this dissertation considers three different material substrates: dielectrics, conductors, and a perfect electrical conductor. In addition, it uses a GSM form in creating the incident field cross-spectral density matrix (CSDM). This allows for the formulation of closed-form expressions for the scattered field CSDM. As such, the analysis shows that two analytical forms result for the scattered field CDSM—one applicable to smooth-to-moderately rough surfaces and the other applicable to very rough surfaces.

Both analytical forms for the scattered field CSDM contain complicated functions of the source parameters (size and coherence properties) and the surface parameters (surface height standard deviation and correlation length). In particular, the closed-form expression applicable to smooth-to-moderately rough surfaces is expressed as an infinite series. This infinite series is slowly convergent; however, one can still gather physical intuition from its analytical form. On the other hand, the closed-form expression applicable to very rough surfaces is incredibly physical, and under certain circumstances, maintains a GSM form. Based on these circumstances, the analysis develops closed-form expressions for the angular spectral degree of coherence (SDoC) and spectral density (SD) radii. These analytical expressions also contain complicated functions of both the source and the surface parameters. The analysis demonstrates that for many scenarios of interest, one can approximate/simplify the SDoC radius as a function of just the source parameters and the SD radius as a function of just the surface parameters.

1.2 Dissertation overview

Chapters 2 and 3 of this dissertation provide background information in the form of theory and literature reviews, respectively. The goal here is to provide future research efforts with a thorough investigation of the problem at hand. Chapter 4 provides the methodology used to obtain the 3D vector solution proposed above. Here, the analysis states all simplifying assumptions and explains their physical implications. Chapter 5 provides an exploration of the 3D vector solution. The analysis given here visually demonstrates aspects of the closed-form expressions and shows that the results are consistent with previously validated solutions and empirical measurements. Chapter 6 provides a conclusion for this dissertation with a roadmap for future research efforts.

2 Background electromagnetic and optics theory review

Electromagnetic theory and subsequently optics theory involves the application of Maxwell's equations to the geometry of a specific problem. As such, the solutions obtained from Maxwell's equations determine the electromagnetic vector fields present within a region of interest. With these vector fields, one can then calculate quantities of importance to their work. The following chapter reviews the necessary electromagnetic and optics theory needed to undertake the problem proposed above in Chapter 1.

2.1 Surface equivalence

There are many approaches to solving Maxwell's equations for the vector fields present in an electromagnetic scattering problem. One robust approach uses surface equivalence. According to Balanis [14], Schelkunoff was the first to introduce surface equivalence in 1936 [15]. In essence, surface equivalence is a more rigorous extension of Huygen's principle [16], which, according to Hecht [17], states that "Every point on a propagating wavefront serves as the source of spherical secondary wavelets, such that the wavefront at some later time is the envelope of these wavelets." With this in mind, surface equivalence effectively defines equivalent sources in the form of surface current densities on a scattering object. Appropriately defined, these surface current densities, in addition to other sources, replicate the fields present in a region of interest.

To make this concept manifest, first consider the generic electromagnetic scattering problem depicted in Figure 1 [18]. As shown, a primary source with current densities, $\mathbf{J}^{pri}$ and $\mathbf{M}^{pri}$, radiates incident fields, $\mathbf{E}^{inc}$ and $\mathbf{H}^{inc}$, which propagate in free space with index of refraction $n_0 = 1$ and impedance $\eta_0 = \sqrt{\mu_0/\varepsilon_0}$, where ε_0 and μ_0 are

the free-space permittivity and permeability, respectively[1]. These known incident fields illuminate a homogeneous, penetrable scattering object of volume V with index of refraction n and impedance η[2]. This illumination produces secondary sources in the form of current densities, $\mathbf{J}^{sec}$ and $\mathbf{M}^{sec}$, which radiate scattered fields, $\mathbf{E}^{sct}$ and $\mathbf{H}^{sct}$. It is important to note that these scattered fields are unknown. Furthermore, a closed surface S with an outward pointing unit-normal vector $\hat{\mathbf{n}}$ creates both an interior and exterior region of interest. The interior region contains the fields, $\mathbf{E}^{int}$ and $\mathbf{H}^{int}$, found inside the closed surface S, whereas the exterior region contains the fields, $\mathbf{E}^{ext}$ and $\mathbf{H}^{ext}$, found outside the closed surface S. These two regions of interest create an interior and exterior problem when using surface equivalence.

---

1. The analysis presented throughout this dissertation uses the MKS system of units so that $\varepsilon_0 = 8.854\times10^{-12}$ (farads per meter) and $\mu_0 = 4\pi\times10^{-7}$ (henries per meter) [14]. In addition, the analysis uses the engineering sign convention for the time-harmonic variations, i.e., $\mathbf{u}(\mathbf{r},t) = \mathbf{U}(\mathbf{r},\omega)\exp(j\omega t) = \mathbf{U}(\mathbf{r},\omega)\mathrm{e}^{j\omega t}$, where $\mathbf{U}(\mathbf{r},\omega)$ is a position $\mathbf{r}$ and angular frequency ω dependent vector field of interest within the analysis. Note that sometimes the analysis omits the $\mathbf{r}$ and ω dependence in writing the vector fields. This is done for brevity in the notation. Also note that formulations which use the physics sign convention, i.e., $\mathbf{u}(\mathbf{r},t) = \mathbf{U}(\mathbf{r},\omega)\exp(-i\omega t) = \mathbf{U}(\mathbf{r},\omega)\mathrm{e}^{-i\omega t}$, relate to this work by a complex conjugate, where $j = i = \sqrt{-1}$.

2. Within a homogeneous space, the index of refraction n and impedance η relate to the permittivity ε and permeability μ, where $n = \sqrt{\varepsilon\mu/(\varepsilon_0\mu_0)}$ and $\eta = \sqrt{\mu/\varepsilon}$ [14].

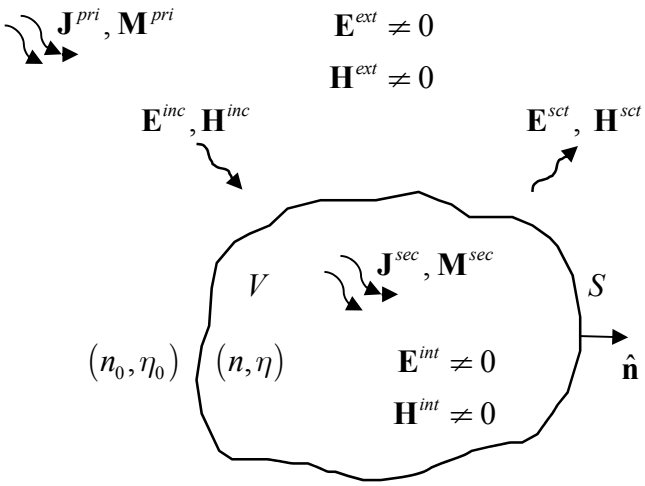

Figure 1. A generic electromagnetic scattering problem. Here, a closed surface surrounds a scattering object creating an interior and exterior region of interest.

2.1.1 Interior problem

Figure 2 describes the interior problem when using surface equivalence [18]. As shown, electric and magnetic surface current densities, $\mathbf{J}_S^{int}$ and $\mathbf{M}_S^{int}$, exist just on the inside of the closed surface S and satisfy the following definitions [14, 19]:

$$\mathbf{J}_S^{int} = -\hat{\mathbf{n}} \times \mathbf{H}^{int} \tag{1}$$

and

$$\mathbf{M}_S^{int} = \hat{\mathbf{n}} \times \mathbf{E}^{int}. \tag{2}$$

These equivalent sources radiate in the absence of the primary source and the exterior fields, i.e., $\mathbf{E}^{ext} = \mathbf{H}^{ext} = 0$. Since the exterior fields equate to zero, this allows the interior region to extend throughout the exterior region creating an unbounded homogeneous space with index of refraction n and impedance η. In addition, the interior fields, $\mathbf{E}^{int}$ and $\mathbf{H}^{int}$, satisfy Maxwell's equations, such that [19]

$$\mathbf{E}^{int} = -\nabla \times \mathbf{F}^{int} - j\frac{\eta}{nk_0}\left(n^2 k_0^2 + \nabla\nabla\cdot\right)\mathbf{A}^{int} \tag{3}$$

and $$\mathbf{H}^{int} = \nabla \times \mathbf{A}^{int} - j\frac{\eta}{nk_0}\left(n^2 k_0^2 + \nabla\nabla\cdot\right)\mathbf{F}^{int}, \tag{4}$$

where $\mathbf{A}^{int}$ and $\mathbf{F}^{int}$ are the interior magnetic and electric vector potentials, respectively, $k_0 = 2\pi/\lambda_0$ is the free-space wavenumber, and λ_0 is the free-space wavelength[3]. Since $\mathbf{J}_S^{int}$ and $\mathbf{M}_S^{int}$ reside on a closed surface S, the vector potentials in Eqs. (3) and (4) satisfy the following convolution integrals [19]:

$$\mathbf{A}^{int} = \mathbf{A}^{int}(\mathbf{r}) = \iint_S \mathbf{J}_S^{int}(\mathbf{r}')G(\mathbf{r};\mathbf{r}')\,ds' \tag{5}$$

and $$\mathbf{F}^{int} = \mathbf{F}^{int}(\mathbf{r}) = \iint_S \mathbf{M}_S^{int}(\mathbf{r}')G(\mathbf{r};\mathbf{r}')\,ds', \tag{6}$$

where $\mathbf{r}'$ is the source vector, $\mathbf{r}$ is the observation vector, and $G(\mathbf{r};\mathbf{r}')$ is the unbounded Green's function, such that

$$G(\mathbf{r};\mathbf{r}') = \frac{\exp\left(-jnk_0\left|\mathbf{r}-\mathbf{r}'\right|\right)}{4\pi\left|\mathbf{r}-\mathbf{r}'\right|}. \tag{7}$$

As a result, the interior problem involves equivalent sources, $\mathbf{J}_S^{int}$ and $\mathbf{M}_S^{int}$, which replicate the interior fields, $\mathbf{E}^{int}$ and $\mathbf{H}^{int}$, in an unbounded homogeneous space.

---

3. Free-space wavelengths in the optical regime typically range from $\lambda_0 = 10^{-2}$ μm in the extreme ultraviolet to $\lambda_0 = 300$ μm in the far infrared [20]; thus, the analysis presented throughout this dissertation assumes that the free-space wavenumber is much, much greater than one, $k_0 = 2\pi/\lambda_0 \gg 1$.

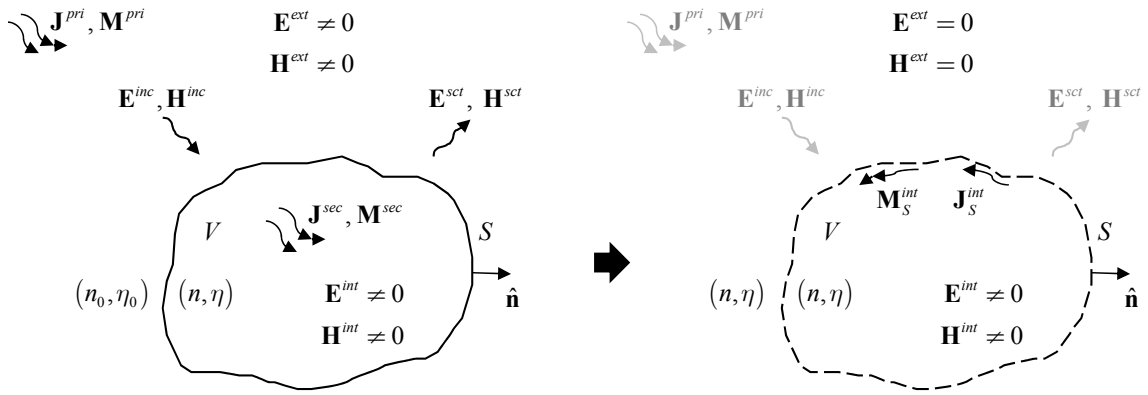

Figure 2. The interior problem associated with using surface equivalence. Here, the exterior region contains null fields; consequently, equivalent sources in the form of surface current densities replicate the interior fields. These equivalent sources effectively radiate in an infinite homogeneous space.

2.1.2 Exterior problem

Similar to the analysis presented for the interior problem, Figure 3 describes the exterior problem using surface equivalence [18]. Here, the electric and magnetic current densities, $\mathbf{J}_S^{ext}$ and $\mathbf{M}_S^{ext}$, exist just on the outside of the closed surface and satisfy the following relationships [14, 19]:

$$\mathbf{J}_S^{ext} = \hat{\mathbf{n}} \times \mathbf{H}^{ext} \tag{8}$$

and

$$\mathbf{M}_S^{ext} = -\hat{\mathbf{n}} \times \mathbf{E}^{ext} . \tag{9}$$

These equivalent sources radiate in the presence of the primary source while the fields in the interior region are nulled, i.e., $\mathbf{E}^{int} = \mathbf{H}^{int} = 0$. Since the interior fields equate to zero, this allows the exterior region to extend throughout the interior region creating an unbounded free space. Moreover, the exterior fields, $\mathbf{E}^{ext}$ and $\mathbf{H}^{ext}$, satisfy the following superposition relationships:

$$\mathbf{E}^{ext} = \mathbf{E}^{inc} + \mathbf{E}^{sct} \tag{10}$$

and

$$\mathbf{H}^{ext} = \mathbf{H}^{inc} + \mathbf{H}^{sct} . \tag{11}$$

Solving Maxwell's equations for the unknown scattered fields, $\mathbf{E}^{sct}$ and $\mathbf{H}^{sct}$, in Eqs. (10) and (11), provides [19]

$$\mathbf{E}^{ext} = \mathbf{E}^{inc} - \nabla \times \mathbf{F}^{ext} - j\frac{\eta_0}{k_0}\left(k_0^2 + \nabla\nabla\cdot\right)\mathbf{A}^{ext} \tag{12}$$

and

$$\mathbf{H}^{ext} = \mathbf{H}^{inc} + \nabla \times \mathbf{A}^{ext} - j\frac{\eta_0}{k_0}\left(k_0^2 + \nabla\nabla\cdot\right)\mathbf{F}^{ext}, \tag{13}$$

where $\mathbf{A}^{ext}$ and $\mathbf{F}^{ext}$ are the exterior magnetic and electric vector potentials, respectively. Since $\mathbf{J}_S^{ext}$ and $\mathbf{M}_S^{ext}$ reside on a closed surface S, the vector potentials in Eqs. (12) and (13) satisfy the following convolution integrals [19]:

$$\mathbf{A}^{ext} = \mathbf{A}^{ext}\left(\mathbf{r}\right) = \iint_S \mathbf{J}_S^{ext}\left(\mathbf{r}'\right) G_0\left(\mathbf{r};\mathbf{r}'\right) ds' \tag{14}$$

and

$$\mathbf{F}^{ext} = \mathbf{F}^{ext}\left(\mathbf{r}\right) = \iint_S \mathbf{M}_S^{ext}\left(\mathbf{r}'\right) G_0\left(\mathbf{r};\mathbf{r}'\right) ds', \tag{15}$$

where here, $G_0\left(\mathbf{r};\mathbf{r}'\right)$ is the free-space Green's function, such that

$$G_0\left(\mathbf{r};\mathbf{r}'\right) = \frac{\exp\left(-jk_0\left|\mathbf{r}-\mathbf{r}'\right|\right)}{4\pi\left|\mathbf{r}-\mathbf{r}'\right|}. \tag{16}$$

Consequently, the exterior problem involves equivalent sources, $\mathbf{J}_S^{ext}$ and $\mathbf{M}_S^{ext}$, which radiate the scattered fields, $\mathbf{E}^{sct}$ and $\mathbf{H}^{sct}$, in the presence of the known incident fields, $\mathbf{E}^{inc}$ and $\mathbf{H}^{inc}$. Together these fields replicate the exterior fields, $\mathbf{E}^{ext}$ and $\mathbf{H}^{ext}$, which propagate throughout free space.

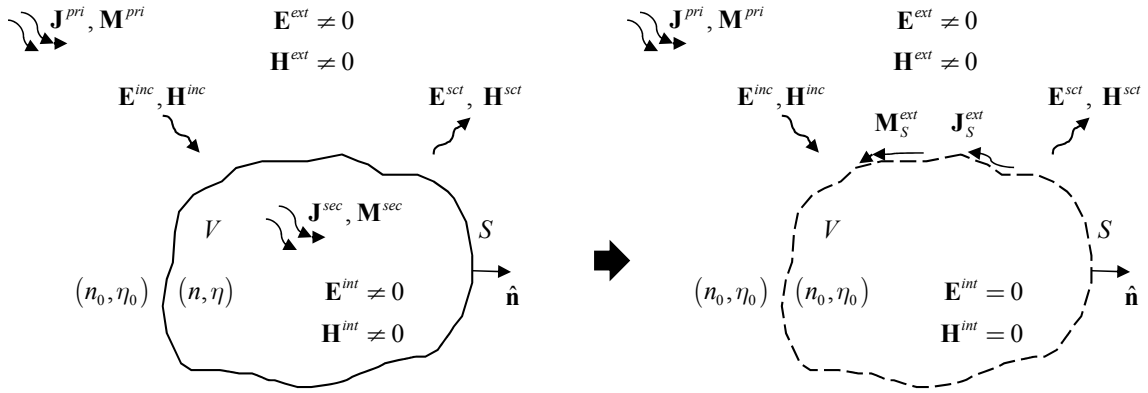

Figure 3. The exterior problem associated with using surface equivalence. Here, the interior region contains null fields; thus, equivalent sources in the form of surface current densities radiate the scattered fields. These equivalent sources radiate in the presence of the primary source and incident fields. Superposition of the incident and scattered fields replicate the exterior fields which propagate throughout free space.

2.1.3 Specialization to a perfect electrical conductor

Figure 4 describes the use of surface equivalence with a perfect electrical conductor (PEC) [18]. Within a perfectly conducting material the interior fields vanish, $\mathbf{E}^{int} = \mathbf{H}^{int} = 0$, so that only an exterior problem exists [19]. In general, a PEC has infinite conductivity, $\sigma = \infty$, and the tangential electric field goes to zero all along its surface, i.e., $\hat{\mathbf{n}} \times \mathbf{E}^{ext} = 0$ [14]. Based on this knowledge, the relationships given in Eqs. (8) and (9) simplify to the following expressions for a PEC:

$$\mathbf{J}_S^{ext} = \hat{\mathbf{n}} \times \mathbf{H}^{ext} \tag{17}$$

and

$$\mathbf{M}_S^{ext} = 0 . \tag{18}$$

Furthermore, Eqs. (12) and (13) simplify, such that

$$\mathbf{E}^{ext} = \mathbf{E}^{inc} - j \frac{\eta_0}{k_0} \left(k_0^2 + \nabla \nabla \cdot \right) \mathbf{A}^{ext} \tag{19}$$

and

$$\mathbf{H}^{ext} = \mathbf{H}^{inc} + \nabla \times \mathbf{A}^{ext} . \tag{20}$$

Provided Eqs. (17)-(20), only an equivalent source $\mathbf{J}_S^{ext}$ is needed to radiate the scattered fields, $\mathbf{E}^{sct}$ and $\mathbf{H}^{sct}$. Superposition with the known incident fields, $\mathbf{E}^{inc}$ and $\mathbf{H}^{inc}$, replicates the exterior fields, $\mathbf{E}^{ext}$ and $\mathbf{H}^{ext}$, which propagate throughout free space.

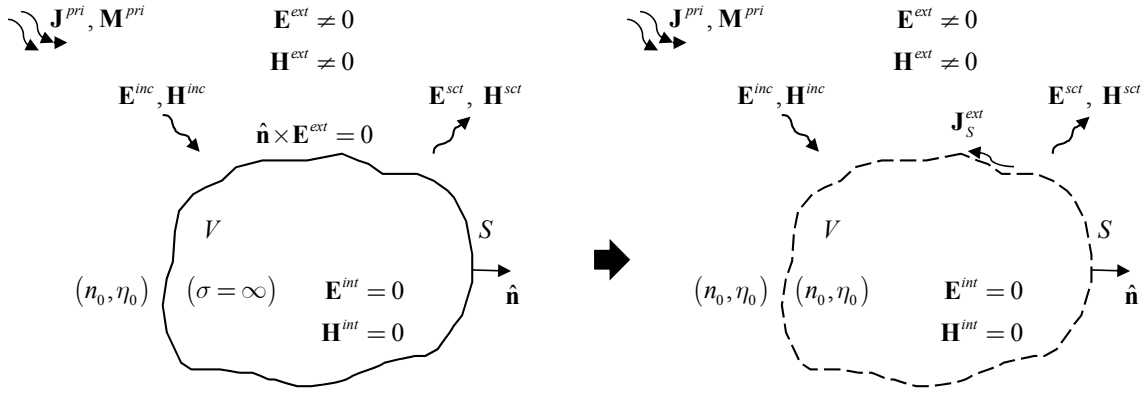

Figure 4. The interior region within a perfect electrical conductor contains null fields. As such, only an exterior problem exists when using surface equivalence. The resulting electric current density radiates the scattered fields and superposition with the known incident fields replicates the exterior fields which propagate throughout free space.

2.2 Integral equations

The continuity of the tangential fields at the interface between the exterior and interior regions dictates that [19]

$$\hat{\mathbf{n}}\times\left(\mathbf{E}^{ext}-\mathbf{E}^{int}\right)=0\Rightarrow\hat{\mathbf{n}}\times\mathbf{E}^{ext}=\hat{\mathbf{n}}\times\mathbf{E}^{int}\Rightarrow\mathbf{J}_S^{ext}=-\mathbf{J}_S^{int}=\mathbf{J}_S^{eq} \tag{21}$$

and

$$\hat{\mathbf{n}}\times\left(\mathbf{H}^{ext}-\mathbf{H}^{int}\right)=0\Rightarrow\hat{\mathbf{n}}\times\mathbf{H}^{ext}=\hat{\mathbf{n}}\times\mathbf{H}^{int}\Rightarrow\mathbf{M}_S^{ext}=-\mathbf{M}_S^{int}=\mathbf{M}_S^{eq}. \tag{22}$$

As such, in an electromagnetic scattering problem using surface equivalence, $\mathbf{J}_S^{eq}$ and $\mathbf{M}_S^{eq}$ readily become the primary unknowns and integral equations result. Numerical techniques help in solving these integral equations for the unknown equivalent surface current densities, $\mathbf{J}_S^{eq}$ and $\mathbf{M}_S^{eq}$.

2.2.1 Electric-field integral equations

Provided the continuity relationship found in Eq. (21), the tangential components of Eqs. (3) and (12) simplify, such that

$$-\mathbf{M}_S^{eq} - \hat{\mathbf{n}} \times \left[-\nabla \times \mathbf{F}^{ext} - j \frac{\eta_0}{k_0} \left(k_0^2 + \nabla \nabla \cdot \right) \mathbf{A}^{ext} \right] = \hat{\mathbf{n}} \times \mathbf{E}^{inc} \tag{23}$$

and

$$\mathbf{M}_S^{eq} - \hat{\mathbf{n}} \times \left[-\nabla \times \mathbf{F}^{int} - j \frac{\eta}{n k_0} \left(n^2 k_0^2 + \nabla \nabla \cdot \right) \mathbf{A}^{int} \right] = 0 \,. \tag{24}$$

These coupled integro-differential equations serve as the electric-field integral equations (EFIEs) for the unknown equivalent surface current densities, $\mathbf{J}_S^{eq}$ and $\mathbf{M}_S^{eq}$. Together, Eqs. (23) and (24) represent a linear system of equations with two equations and two unknowns. It is important to note that for a PEC, the tangential electric field goes to zero all along its surface, i.e., $\hat{\mathbf{n}} \times \mathbf{E}^{ext} = 0$; thus, the following EFIE results from Eq. (19):

$$\hat{\mathbf{n}} \times \mathbf{E}^{inc} = -\hat{\mathbf{n}} \times \left[-j \frac{\eta_0}{k_0} \left(k_0^2 + \nabla \nabla \cdot \right) \mathbf{A}^{ext} \right] . \tag{25}$$

This EFIE is an integro-differential equation for the unknown equivalent surface current density $\mathbf{J}_S^{eq}$.

2.2.2 Magnetic-field integral equations

Magnetic-field integral equations (MFIEs) result from the continuity relationship given in Eq. (22). Specifically, the tangential components of Eqs. (4) and (13) simplify, so that

$$\mathbf{J}_S^{eq} - \hat{\mathbf{n}} \times \left[\nabla \times \mathbf{A}^{ext} - j \frac{\eta_0}{k_0} \left(k_0^2 + \nabla \nabla \cdot \right) \mathbf{F}^{ext} \right] = \hat{\mathbf{n}} \times \mathbf{H}^{inc} \tag{26}$$

and $$-\mathbf{J}_S^{eq} - \hat{\mathbf{n}} \times \left[\nabla \times \mathbf{A}^{int} - j \frac{\eta}{n k_0} \left(n^2 k_0^2 + \nabla \nabla \cdot \right) \mathbf{F}^{int} \right] = 0 \,. \tag{27}$$

These coupled integro-differential equations are the MFIEs for the unknown equivalent surface current densities, $\mathbf{J}_S^{eq}$ and $\mathbf{M}_S^{eq}$. One should note that Eqs. (26) and (27) represent a system of linear equations with two equations and two unknowns. Moreover, the tangential components of Eq. (20) create the following MFIE for a PEC:

$$\mathbf{J}_S^{eq} - \hat{\mathbf{n}} \times \nabla \times \mathbf{A}^{ext} = \hat{\mathbf{n}} \times \mathbf{H}^{inc} \,. \tag{28}$$

This MFIE is an integro-differential equation for the unknown equivalent surface current density $\mathbf{J}_S^{eq}$.

2.2.3 Method of moments

The method of moments (MoM) is a robust numerical approach that solves EFIEs or MFIEs for the unknown equivalent surface current densities, $\mathbf{J}_S^{eq}$ and $\mathbf{M}_S^{eq}$ [14, 19, 21]. In using the MoM, a series of finite terms or basis functions with unknown amplitude coefficients effectively replace $\mathbf{J}_S^{eq}$ and $\mathbf{M}_S^{eq}$. This creates a number of algebraic expressions which matrix algebra techniques readily solve. As a result, the MoM has the potential to formulate high-fidelity numerical solutions for the unknown equivalent surface current densities, $\mathbf{J}_S^{eq}$ and $\mathbf{M}_S^{eq}$.

2.3 Physical optics approximation

It is important to remember that when using surface equivalence in an electromagnetic scattering problem, the equivalent surface current densities, $\mathbf{J}_S^{eq}$ and $\mathbf{M}_S^{eq}$, radiate the unknown scattered fields, $\mathbf{E}^{sct}$ and $\mathbf{H}^{sct}$, which propagate in free space

with index of refraction n_0 and impedance η_0. This facilitates the use of a free-space Green's function $G_0(\mathbf{r};\mathbf{r}')$ [cf. Eq. (16)]; however, it is still difficult to formulate analytical solutions for $\mathbf{J}_S^{eq}$ and $\mathbf{M}_S^{eq}$ since they are, by definition, dependent on $\mathbf{E}^{sct}$ and $\mathbf{H}^{sct}$, which are unknown. The physical-optics (PO) approximation helps to alleviate these constraints [14, 22]. In essence, the PO approximation makes use of the geometrical-optics (GO) approximation to formulate the current densities involved in an electromagnetic scattering problem. Figure 5 helps to further explain this point [18]. As shown, the current densities formulated with the PO approximation equate to zero in the shadow regions of a scattering object—an assumption which is analogous to using Kirchhoff boundary conditions in physical or wave optics [23, 24].

When using the PO approximation with surface equivalence, one replaces the unknown scattered fields with reflected fields. Specifically, $\mathbf{E}^{sct} \approx \mathbf{E}^{ref}$ and $\mathbf{H}^{sct} \approx \mathbf{H}^{ref}$, so that the equivalent surface current densities, $\mathbf{J}_S^{eq}$ and $\mathbf{M}_S^{eq}$, become

$$\mathbf{J}_S^{eq} = \hat{\mathbf{n}} \times \mathbf{H}^{ext} = \hat{\mathbf{n}} \times \left(\mathbf{H}^{inc} + \mathbf{H}^{sct} \right) \approx \hat{\mathbf{n}} \times \left(\mathbf{H}^{inc} + \mathbf{H}^{ref} \right) \tag{29}$$

and

$$\mathbf{M}_S^{eq} = -\hat{\mathbf{n}} \times \mathbf{E}^{ext} = -\hat{\mathbf{n}} \times \left(\mathbf{E}^{inc} + \mathbf{E}^{sct} \right) \approx -\hat{\mathbf{n}} \times \left(\mathbf{E}^{inc} + \mathbf{E}^{ref} \right). \tag{30}$$

These approximations assume that the scattering object and its associated curvature are large compared to the wavelength of the incident fields, $\mathbf{E}^{inc}$ and $\mathbf{H}^{inc}$[4]. Such approximations are exact if the scattering object is homogeneous, infinite, and planar [14, 22]. With that said, the incident illumination follows the law of reflection—a direct

4. This is consistent with geometrical or ray optics, which emerges as the limit of physical or wave optics when the wavelength approaches zero, $\lambda_0 \to 0$ [20, 22].

result from the GO approximation [22]—so that the tangential reflected fields, $\hat{\mathbf{n}}\times\mathbf{E}^{ref}$ and $\hat{\mathbf{n}}\times\mathbf{H}^{ref}$, relate to the tangential incident fields, $\hat{\mathbf{n}}\times\mathbf{E}^{inc}$ and $\hat{\mathbf{n}}\times\mathbf{H}^{inc}$, in unique ways for different material substrates, i.e., dielectrics, conductors, and a PEC. Appendix A explores these relationships in more detail.

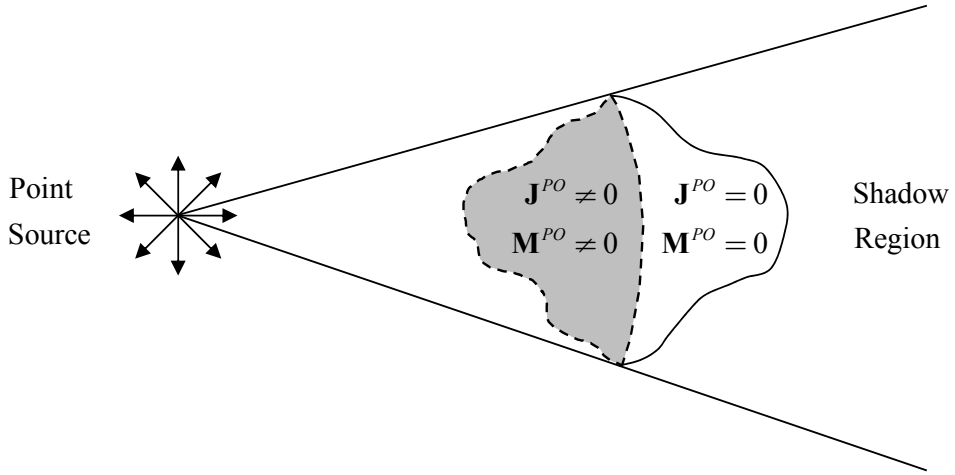

Figure 5. A macro-scale description of the physical optics (PO) approximation. Here, a point source illuminates a scattering object so that no current densities exist in the shadow region predicted by the geometrical optics approximation.

2.3.1 General problem for dielectrics

As shown in Appendix A, the following relationships hold true for dielectrics according to the GO approximation [18]:

$$\hat{\mathbf{n}}\times\mathbf{E}^{ref} = r_S\hat{\mathbf{n}}\times\mathbf{E}^{inc} \tag{31}$$

and

$$\hat{\mathbf{n}}\times\mathbf{H}^{ref} = -r_S\hat{\mathbf{n}}\times\mathbf{H}^{inc}, \tag{32}$$

where r_S is the known Fresnel reflection coefficient at the closed surface S of a scattering object. Accordingly, the equivalent surface current densities, $\mathbf{J}_S^{eq}$ and $\mathbf{M}_S^{eq}$, as given in Eqs. (29) and (30), simplify so that

$$\mathbf{J}_S^{eq} \approx \left(1-r_S\right)\hat{\mathbf{n}}\times\mathbf{H}^{inc} \tag{33}$$

and $$\mathbf{M}_S^{eq} \approx -\left(1+r_S\right)\hat{\mathbf{n}}\times\mathbf{E}^{inc}. \tag{34}$$

This dictates that when using the PO approximation for a dielectric material, the known tangential incident fields, $\hat{\mathbf{n}}\times\mathbf{E}^{inc}$ and $\hat{\mathbf{n}}\times\mathbf{H}^{inc}$, in addition to the known Fresnel reflection coefficient, r_s, are all that is needed in determining the analytical forms of $\mathbf{J}_S^{eq}$ and $\mathbf{M}_S^{eq}$.

2.3.2 Specialization to conductors

For very good conductors, the conductivity approaches infinity, $\sigma \to \infty$ [14]. As such, the tangential incident electric field approximates to zero all along the surface of a conducting material, i.e., $\hat{\mathbf{n}}\times\mathbf{E}^{inc} \approx 0$, and Eqs. (33) and (34) simplify to the following relationships:

$$\mathbf{J}_S^{eq} \approx \left(1-r_S\right)\hat{\mathbf{n}}\times\mathbf{H}^{inc} \tag{35}$$

and $$\mathbf{M}_S^{eq} \approx 0. \tag{36}$$

Thus, the analysis simplifies from that of dielectrics. Only the electric equivalent surface current density $\mathbf{J}_S^{eq}$ radiates when using the PO approximation for a conducting material.

2.3.3 Specialization to a perfect electrical conductor

As shown in Appendix A, the following relationships hold true for a PEC according to the GO approximation [18]:

$$\hat{\mathbf{n}}\times\mathbf{E}^{ref} = -\hat{\mathbf{n}}\times\mathbf{E}^{inc} \tag{37}$$

and $$\hat{\mathbf{n}}\times\mathbf{H}^{ref} = \hat{\mathbf{n}}\times\mathbf{H}^{inc}. \tag{38}$$

Consequently, the equivalent surface current densities, $\mathbf{J}_S^{eq}$ and $\mathbf{M}_S^{eq}$, as given in Eqs. (29) and (30), simply so that

$$\mathbf{J}_S^{eq} \approx 2\hat{\mathbf{n}} \times \mathbf{H}^{inc} \tag{39}$$

and

$$\mathbf{M}_S^{eq} = 0 . \tag{40}$$

This dictates that when using the PO approximation for a perfectly conducting material, the known tangential incident magnetic field $\hat{\mathbf{n}} \times \mathbf{H}^{inc}$ is all that is needed in determining the analytical form of $\mathbf{J}_S^{eq}$.

2.4 Mathematical techniques

Mathematical techniques exist which further simplify the analysis beyond the PO approximation. To help make these mathematical techniques unambiguous, first consider the 3D electromagnetic scattering setup described in Figure 6. The analysis also refers to this setup as the macro-scale scattering geometry. Here, the vector, $\boldsymbol{\rho} = x\hat{\mathbf{x}} + u\hat{\mathbf{u}}$, points from the source plane origin to a transverse location in the source s, since $v = 0$ in the source plane; the vector, $\tilde{\mathbf{r}} = 0\hat{\mathbf{x}} - \tilde{y}\hat{\mathbf{y}} + \tilde{z}\hat{\mathbf{z}}$, points from the source plane origin to the surface plane origin; the vector, $\mathbf{r}' = x'\hat{\mathbf{x}} + y'\hat{\mathbf{y}} + z'\hat{\mathbf{z}}$, points from the surface plane origin to a point on the closed surface S; and the vector, $\mathbf{r} = x\hat{\mathbf{x}} + y\hat{\mathbf{y}} + z\hat{\mathbf{z}}$, points from the surface plane origin to an observation point. This setup plays a pivotal role in employing the far-field approximation, plane-wave spectrum representation, and method of stationary phase, all of which are mathematical techniques which greatly simplify the analysis when used under the right assumptions.

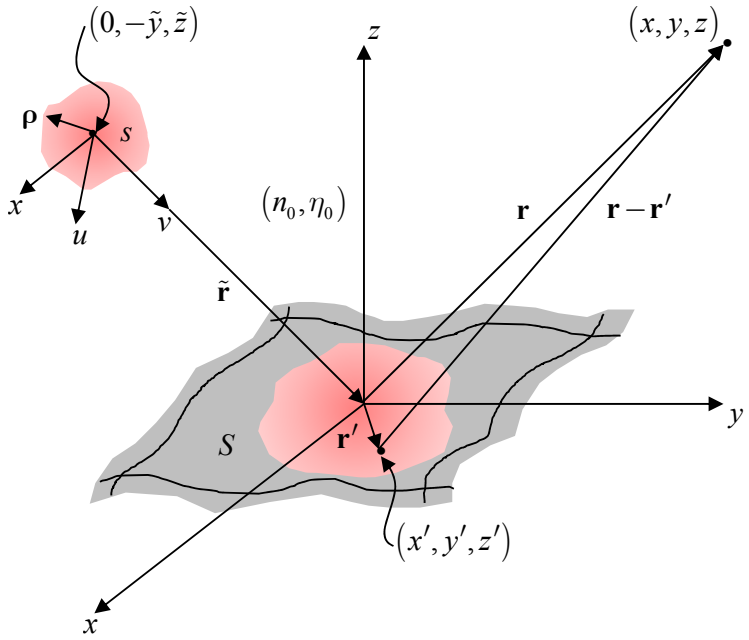

Figure 6. A generic setup for 3D electromagnetic scattering problems. Here, the *x* axes align in both the source plane and the surface plane. This assumes isotropy in the material substrate.

2.4.1 Far-field approximation

In the far field, $\mathbf{r}-\mathbf{r}'$ is approximately parallel to $\mathbf{r}$, as shown in Figure 7 [18]. Additionally, $k_0|\mathbf{r}-\mathbf{r}'| \gg 1$, and the following approximations result [14]:

$$|\mathbf{r}-\mathbf{r}'| = \sqrt{r^2+r'^2-2\mathbf{r}\cdot\mathbf{r}'} \approx \begin{cases} r-\hat{\mathbf{r}}\cdot\mathbf{r}' & \text{for phase variations} \\ r & \text{for amplitude variations} \end{cases}, \tag{41}$$

where $r=|\mathbf{r}|$, $r'=|\mathbf{r}'|$, and

$$\hat{\mathbf{r}}\cdot\mathbf{r}' = x'\sin(\theta)\cos(\phi)+y'\sin(\theta)\sin(\phi)+z'\cos(\theta). \tag{42}$$

Provided Eqs. (41) and (42), the free-space Green's function $G_0(\mathbf{r};\mathbf{r}')$, as given in Eq. (16), simplifies so that

$$G_0(\mathbf{r};\mathbf{r}') = \frac{\exp(-jk_0|\mathbf{r}-\mathbf{r}'|)}{4\pi|\mathbf{r}-\mathbf{r}'|} \approx \frac{\exp(-jk_0 r)}{4\pi r}\exp(jk_0\hat{\mathbf{r}}\cdot\mathbf{r}'). \tag{43}$$

From Eq. (43), the unknown scattered fields, $\mathbf{E}^{sct}$ and $\mathbf{H}^{sct}$, as formulated above in Eqs. (12) and (13), satisfy the following approximations [14]:

$$\mathbf{E}^{sct} = -\nabla\times\mathbf{F}^{ext} - j\frac{\eta_0}{k_0}\left(k_0^2 + \nabla\nabla\cdot\right)\mathbf{A}^{ext} \approx \mathbf{E}_N^{sct} + \mathbf{E}_L^{sct} \tag{44}$$

and

$$\mathbf{H}^{sct} = \nabla\times\mathbf{A}^{ext} - j\frac{\eta_0}{k_0}\left(k_0^2 + \nabla\nabla\cdot\right)\mathbf{F}^{ext} \approx \mathbf{H}_N^{sct} + \mathbf{H}_L^{sct}, \tag{45}$$

where

$$\mathbf{E}_N^{sct} = -jk_0\eta_0\frac{\exp\left(-jk_0r\right)}{4\pi r}\left(\hat{\boldsymbol{\theta}}\hat{\boldsymbol{\theta}} + \hat{\boldsymbol{\phi}}\hat{\boldsymbol{\phi}}\right)\cdot\mathbf{N}^{ext}, \tag{46}$$

$$\mathbf{H}_N^{sct} = \frac{1}{\eta_0}\hat{\mathbf{r}}\times\mathbf{E}_N^{sct}, \tag{47}$$

$$\mathbf{H}_L^{sct} = -j\frac{k_0}{\eta_0}\frac{\exp\left(-jk_0r\right)}{4\pi r}\left(\hat{\boldsymbol{\theta}}\hat{\boldsymbol{\theta}} + \hat{\boldsymbol{\phi}}\hat{\boldsymbol{\phi}}\right)\cdot\mathbf{L}^{ext}, \tag{48}$$

and

$$\mathbf{E}_L^{sct} = -\eta_0\hat{\mathbf{r}}\times\mathbf{H}_L^{sct}. \tag{49}$$

These expressions depend on the far-field-exterior magnetic and electric vector potentials, $\mathbf{N}^{ext}$ and $\mathbf{L}^{ext}$, such that

$$\mathbf{N}^{ext} = \mathbf{N}^{ext}\left(\mathbf{r}\right) = \iint_S \mathbf{J}_S^{eq}\left(\mathbf{r}'\right)\exp\left(jk_0\hat{\mathbf{r}}\cdot\mathbf{r}'\right)ds' \tag{50}$$

and

$$\mathbf{L}^{ext} = \mathbf{L}^{ext}\left(\mathbf{r}\right) = \iint_S \mathbf{M}_S^{eq}\left(\mathbf{r}'\right)\exp\left(jk_0\hat{\mathbf{r}}\cdot\mathbf{r}'\right)ds'. \tag{51}$$

It is important to remember that the PO approximation simplifies the analysis so that the known incident fields, $\mathbf{E}^{inc}$ and $\mathbf{H}^{inc}$, help in determining the analytical form of the equivalent surface current densities, $\mathbf{J}_S^{eq}$ and $\mathbf{M}_S^{eq}$, in Eqs. (50) and (51). Moving forward, one can use the plane-wave spectrum representation to account for $\mathbf{E}^{inc}$ and $\mathbf{H}^{inc}$.

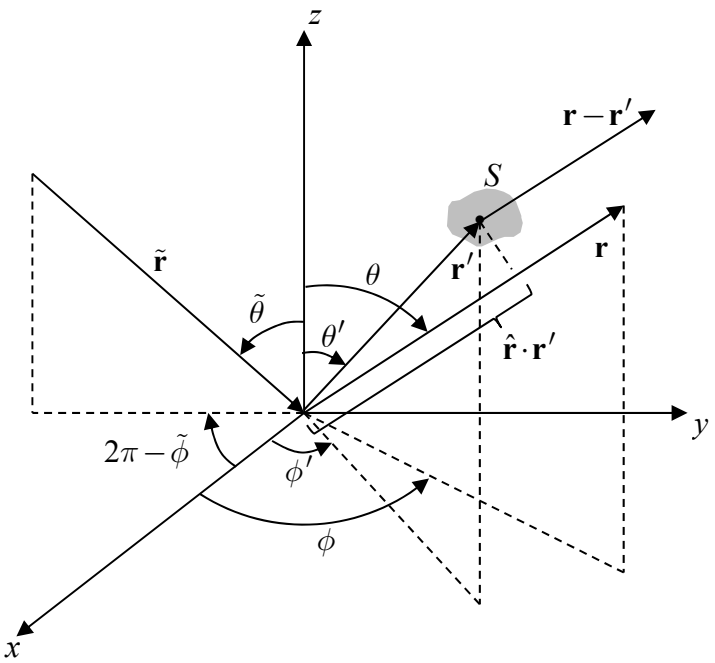

Figure 7. The micro-scale geometry describing far-field electromagnetic scattering. Here, the observation point extends well past what is depicted and only a small portion of the closed surface is displayed. This corresponds to a zoomed-in description of Figure 6.

2.4.2 Plane-wave spectrum representation

In order to determine the analytical form of the equivalent surface current densities, $\mathbf{J}_S^{eq}$ and $\mathbf{M}_S^{eq}$, the analysis must first account for the known incident fields, $\mathbf{E}^{inc}$ and $\mathbf{H}^{inc}$, which propagate from the source s and illuminate the closed surface S [cf. Figure 6]. With this in mind, one can write the incident electric field $\mathbf{E}^{inc}$ in terms of its spectrum $\mathbf{T}_e^{inc}$ using the plane wave spectrum representation [25]. The following expressions result using the macro-scale scattering geometry described in Figure 6:

$$\mathbf{E}^{inc}=\mathbf{E}^{inc}\left(\mathbf{r}\right)=\frac{1}{\left(2\pi\right)^2}\int_{-\infty}^{\infty}\int_{-\infty}^{\infty}\mathbf{T}_e^{inc}\left(k_x^{inc},k_u^{inc}\right)\exp\left[-j\mathbf{k}^{inc}\cdot\left(\tilde{\mathbf{r}}+\mathbf{r}\right)\right]dk_x^{inc}dk_u^{inc},\quad v\geq 0 \quad (52)$$

and

$$\mathbf{T}_e^{inc}=\mathbf{T}_e^{inc}\left(k_x^{inc},k_u^{inc}\right)=\int_{-\infty}^{\infty}\int_{-\infty}^{\infty}\mathbf{E}^{inc}\left(\boldsymbol{\rho}\right)\exp\left[\,j\left(k_x^{inc}x+k_u^{inc}u\right)\right]dxdu,\quad v\geq 0\,. \quad (53)$$

Here, $\mathbf{k}^{inc} = k_x^{inc}\hat{\mathbf{x}} + k_u^{inc}\hat{\mathbf{u}} + k_v^{inc}\hat{\mathbf{v}}$ is the incident propagation vector and $v \geq 0$ is the source-free half space with index of refraction $n_0 = 1$ and impedance $\eta_0 = \sqrt{\mu_0/\varepsilon_0}$. Since the divergence of the incident electric field equals zero in a source-free half space, i.e., $\nabla \cdot \mathbf{E}^{inc} = 0$, it follows that in the spatial-frequency domain,

$$\mathbf{k}^{inc} \cdot \mathbf{T}_e^{inc} = k_x^{inc} T_{ex}^{inc} + k_u^{inc} T_{eu}^{inc} + k_v^{inc} T_{ev}^{inc} = 0 . \tag{54}$$

This physically states that the spectrum of the incident electric field $\mathbf{T}_e^{inc}$ is perpendicular to the incident propagation vector $\mathbf{k}^{inc}$. Thus, for $k_v^{inc} \neq 0$,

$$T_{ev}^{inc} = -\frac{k_x^{inc}}{k_v^{inc}} T_{ex}^{inc} - \frac{k_u^{inc}}{k_v^{inc}} T_{eu}^{inc} , \tag{55}$$

so that the *x* and *u* components of $\mathbf{T}_e^{inc}$ uniquely provide the *v* component.

In a similar fashion, the following relationships provide the plane-wave spectrum representation for the incident magnetic field $\mathbf{H}^{inc}$ and its spectrum $\mathbf{T}_h^{inc}$ [25]:

$$\mathbf{H}^{inc} = \mathbf{H}^{inc}(\mathbf{r}) = \frac{1}{(2\pi)^2} \int_{-\infty}^{\infty} \int_{-\infty}^{\infty} \mathbf{T}_h^{inc}\left(k_x^{inc}, k_u^{inc}\right) \exp\left[-j\mathbf{k}^{inc} \cdot (\tilde{\mathbf{r}} + \mathbf{r})\right] dk_x^{inc} dk_u^{inc}, \quad v \geq 0 \tag{56}$$

and

$$\mathbf{T}_h^{inc} = \mathbf{T}_h^{inc}\left(k_x^{inc}, k_u^{inc}\right) = \int_{-\infty}^{\infty} \int_{-\infty}^{\infty} \mathbf{H}^{inc}(\boldsymbol{\rho}) \exp\left[j\left(k_x^{inc} x + k_u^{inc} u\right)\right] dx du, \quad v \geq 0 . \tag{57}$$

From Maxwell's equations, $\nabla \times \mathbf{E}^{inc} = -j\omega_0 \mu_0 \mathbf{H}^{inc}$, so that in the spatial-frequency domain,

$$\mathbf{k}^{inc} \times \mathbf{T}_e^{inc} = \omega_0 \mu_0 \mathbf{T}_h^{inc} . \tag{58}$$

Here, $\omega_0 = 2\pi\nu_0$ is the free-space angular frequency and ν_0 is the free-space frequency. In an equivalent form, $\mathbf{k}^{inc} = k_0 \hat{\mathbf{k}}^{inc} = \omega_0 \sqrt{\mu_0 \varepsilon_0}\, \hat{\mathbf{k}}^{inc}$, where $\hat{\mathbf{k}}^{inc}$ is the incident unit-

propagation vector. Consequently, the spectrum of the incident magnetic field $\mathbf{T}_h^{inc}$ relates to the spectrum of the incident electric field $\mathbf{T}_e^{inc}$ in the following ways:

$$\mathbf{T}_h^{inc} = \frac{1}{\omega_0 \mu_0} \mathbf{k}^{inc} \times \mathbf{T}_e^{inc} = \sqrt{\frac{\varepsilon_0}{\mu_0}} \hat{\mathbf{k}}^{inc} \times \mathbf{T}_e^{inc} = \frac{1}{\eta_0} \hat{\mathbf{k}}^{inc} \times \mathbf{T}_e^{inc} . \tag{59}$$

It follows that $\mathbf{T}_h$ is also perpendicular to the incident propagation vector $\mathbf{k}^{inc}$; namely,

$$\mathbf{k}^{inc} \cdot \mathbf{T}_h^{inc} = k_x^{inc} T_{hx}^{inc} + k_u^{inc} T_{hu}^{inc} + k_v^{inc} T_{hv}^{inc} = 0 , \tag{60}$$

so that for $k_v^{inc} \neq 0$,

$$T_{hv}^{inc} = -\frac{k_x^{inc}}{k_v^{inc}} T_{hx}^{inc} - \frac{k_u^{inc}}{k_v^{inc}} T_{hu}^{inc} . \tag{61}$$

This says that both the *x* and *u* components of $\mathbf{T}_h^{inc}$ uniquely provide the *v* component.

Before moving on in the analysis, it is important to note that the expressions given in Eqs. (53) and (57) for the incident spectrums, $\mathbf{T}_e^{inc}$ and $\mathbf{T}_h^{inc}$, are mathematically equivalent to taking the two-dimensional Fourier transform of the incident fields in the source plane, i.e., $\mathbf{E}^{inc}(\boldsymbol{\rho})$ and $\mathbf{H}^{inc}(\boldsymbol{\rho})$, and going to the spatial-frequency domain. With that said, the expressions given in Eqs. (52) and (57) allow one to then determine incident fields at any observation point, i.e., $\mathbf{E}^{inc}(\mathbf{r})$ and $\mathbf{H}^{inc}(\mathbf{r})$. Physically, this is analogous to summing up the contributions of a bunch of forward propagating plane waves which originate from the source plane [20]. It is also important to note that the plane-wave spectrum representation often results in rather complex integral expressions. In practice, one must employ additional mathematical techniques, such as the method of stationary phase, to solve these complex integral expressions.

2.4.3 Method of stationary phase

In using the plane-wave spectrum representation (along with the far-field and PO approximations), integrals of the following form often result [18]:

$$F(k) = \int_a^b f(x) \exp\left[jkg(x) \right] dx, \quad \text{as } k \to \infty . \tag{62}$$

Here, $f(x)$ is slowly varying in the interval $[a,b]$ and $kg(x)$ is rapidly oscillating except near special points where the rate of change of $g(x)$ is stationary within the interval, i.e., where

$$\frac{d}{dx} g(x) = g'(x) = 0 . \tag{63}$$

These special points are called critical points of the first kind [26]. Away from these points, $kg(x)$ is rapidly oscillating and the positive and negative contributions of the integrand effectively cancel out. In this case, an asymptotic mathematical technique known as the method of stationary phase helps in solving the integral formulated in Eq. (62).

The initial analysis assumes that there is only one critical point of the first kind; namely, at $x = x_0$ and that $f(x)$ and $g(x)$ are both continuous and well behaved in the interval $[a,b]$. Subsequently, the following conditions must hold true: $g(x_0) \neq 0$, $g'(x_0) = 0$, and $g''(x_0) \neq 0$, so that upon expanding in a Taylor series,

$$g(x) = g(x_0) + g'(x_0)(x - x_0) + g''(x_0) \frac{(x - x_0)^2}{2} + \ldots \approx g(x_0) + g''(x_0) \frac{(x - x_0)^2}{2} \tag{64}$$

and $$f(x) = f(x_0) + f'(x_0)(x - x_0) + f''(x_0)\frac{(x - x_0)^2}{2} + \ldots \approx f(x_0), \tag{65}$$

since $f(x)$ is slowly varying. Substituting Eqs. (64) and (65) into Eq. (62), the method of stationary phase dictates that [26]

$$F(k) \approx F^{(1)}(k) + F^{(2)}(k), \quad \text{as } k \to \infty. \tag{66}$$

Here, $$F^{(1)}(k) = f(x_0)\exp\left[jkg(x_0)\right]\int_{-\infty}^{\infty}\exp\left[jk\frac{(x - x_0)^2}{2}g''(x_0)\right]dx \tag{67}$$

is the contribution from the critical point of the first kind at $x = x_0$, and $F^{(2)}(k)$ is the contribution from the end points. These end points are called critical points of the second kind [26]; however, the present analysis neglects to formulate their contributions[5]. With some mathematical prowess, Eq. (66) evaluates to the following expression [26]:

$$F(k) \approx F^{(1)}(k) = \sqrt{\frac{2\pi}{k}}\frac{f(x_0)}{\left|g''(x_0)\right|^{1/2}}\exp\left[jkg(x_0)\right]\exp\left(j\frac{\pi}{4}\operatorname{sgn}\left[g''(x_0)\right]\right), \tag{68}$$

where $$\operatorname{sgn}\left[g''(x_0)\right] = \begin{cases} 1 & \text{if } g''(x_0) > 0 \\ -1 & \text{if } g''(x_0) < 0 \end{cases}. \tag{69}$$

In general, if there are multiple critical points of the first kind present in the analysis, then their individual contributions sum together.

The analysis leading up to Eqs. (68) and (69) assumed one-dimensional integration; however, the method of stationary phase extends to *n*-dimensional integration

5. Critical points of the second kind do not come into play because of the nature of the fields assumed in this research effort.

[27, 28]. As such, the contribution $F^{(1)}(k)$ from the critical point of the first kind at $\mathbf{x} = \mathbf{x}_0 = (x_{10}, x_{20}, \ldots, x_{n0})$ becomes

$$F^{(1)}(k) = \left(\frac{2\pi}{k}\right)^{n/2} \frac{f(\mathbf{x}_0)}{\left|\mathrm{Det}\left\{\partial_x^2 g(\mathbf{x}_0)\right\}\right|^{1/2}} \exp\left[jkg(\mathbf{x}_0)\right] \exp\left(j\frac{\pi}{4}\mathrm{sgn}\left\{\partial_x^2 g(\mathbf{x}_0)\right\}\right), \quad (70)$$

where

$$\partial_x^2 g(\mathbf{x}_0) = \left[\begin{array}{cccc} \frac{\partial^2 g(\mathbf{x})}{\partial x_1^{\,2}} & \frac{\partial^2 g(\mathbf{x})}{\partial x_1 \partial x_2} & \cdots & \frac{\partial^2 g(\mathbf{x})}{\partial x_1 \partial x_n} \\ \frac{\partial^2 g(\mathbf{x})}{\partial x_2 \partial x_1} & \frac{\partial^2 g(\mathbf{x})}{\partial x_2^{\,2}} & \cdots & \frac{\partial^2 g(\mathbf{x})}{\partial x_2 \partial x_n} \\ \vdots & \vdots & \ddots & \vdots \\ \frac{\partial^2 g(\mathbf{x})}{\partial x_n \partial x_1} & \frac{\partial^2 g(\mathbf{x})}{\partial x_n \partial x_2} & \cdots & \frac{\partial^2 g(\mathbf{x})}{\partial x_n^{\,2}} \end{array}\right]_{\mathbf{x}=\mathbf{x}_0}, \quad (71)$$

$\mathrm{Det}\{\cdots\}$ denotes the determinant operation, and $\mathrm{sgn}\{A\} = \lambda_+\{A\} - \lambda_-\{A\}$ denotes the signature of a real symmetric non-degenerate matrix A. Here, $\lambda_\pm\{A\}$ are the number of positive and negative eigenvalues of A.

2.5 Coherence

The fields of interest in electromagnetic scattering problems are often random in nature. Goodman refers to such fields as optical disturbances [29]. Of primary concern in the statistical analysis of optical disturbances is coherence. In essence, coherence describes the degree to which one point in a given optical disturbance relates to any other point within the optical disturbance in time or space. An optical disturbance is coherent when there is a fixed relation between one point and all other points within the optical disturbance. On the other hand, an optical disturbance is then incoherent when there is no fixed relation between one point and any other point. Statistical properties that fall

somewhere between the preceding descriptions provide for a partially coherent optical disturbance. Mathematically, one realizes coherence through correlation functions $\Gamma(\mathbf{r}_1, \mathbf{r}_2; t_1, t_2)$. These correlation functions are, in general, dependent on two points in space, $\mathbf{r}_1$ and $\mathbf{r}_2$, or two instances of time, t_1 and t_2.

2.5.1 Self-coherence function

When analyzing temporal coherence, an individual uses what Goodman refers to as the self-coherence function $\Gamma(\mathbf{r}, \tau)$ [29]. Specifically,

$$\Gamma(\mathbf{r}, \tau) = \lim_{T \to \infty} \frac{1}{T} \int_{-T/2}^{T/2} u(\mathbf{r}, t+\tau) u^*(\mathbf{r}, t)\, dt = \left\langle u(\mathbf{r}, t+\tau) u^*(\mathbf{r}, t) \right\rangle, \tag{72}$$

which is simply the time autocorrelation of an analytic function $u(\mathbf{r}, t)$ at a single point in space $\mathbf{r}$. Throughout the analysis, $u(\mathbf{r}, t)$ represents the optical disturbance of interest and $u^*(\mathbf{r}, t)$ represents the complex conjugate of that optical disturbance[6]. Note that in writing Eq. (72), one assumes that the optical disturbance is emanating from a point source, so that only temporal coherence effects plays a role. As such, the temporal quantity, $\tau = t_2 - t_1$, is the time interval of interest in quantifying temporal coherence. Put simply, the self-coherence function $\Gamma(\mathbf{r}, \tau)$ gives a distinct gauge for temporal coherence provided $\tau \ll \tau_c \approx 2\pi / \Delta\omega$, where τ_c is the coherence time and $\Delta\omega$ is the finite angular bandwidth of the optical disturbance [29]. The process used to measure temporal coherence helps in explaining this point further.

---

6. Note that the scalar field analysis presented here holds for vector fields, i.e., each component of the vector field.

In practice, coherence measurements require the interference of light using optical devices called interferometers. The type of interferometer used depends highly on the type of coherence to be measured for a given optical source. For example, when temporal coherence is of concern, light from a point source is interfered with a delayed version of itself. This type of interference requires amplitude splitting of the light. A Michelson interferometer achieves this type of interference and is readily described throughout the optics literature—Goodman's treatment is particularly insightful [29]. In the detection plane of a Michelson interferometer, the irradiance $I(\tau)$ scales with the self-coherence function $\Gamma(\mathbf{r},\tau)$. This says that one can measure temporal coherence through the interference of light.

2.5.2 Mutual-coherence function

When analyzing spatial coherence, an individual uses what Wolf, Goodman, and many others refer to as the mutual coherence function (MCF) $\Gamma(\mathbf{r}_1,\mathbf{r}_2,\tau)$ [13, 29]. In particular,

$$\Gamma(\mathbf{r}_1,\mathbf{r}_2,\tau)=\left\langle u(\mathbf{r}_1,t+\tau)u^*(\mathbf{r}_2,t)\right\rangle, \tag{73}$$

which is a time cross correlation of an analytic function $u(\mathbf{r},t)$ at two points in space, $\mathbf{r}_1$ and $\mathbf{r}_2$. When dealing with a single point in space $\mathbf{r}$, Eq. (73) reduces to a self-coherence function $\Gamma(\mathbf{r},\tau)$, as given in Eq. (72), so that in general, the MCF $\Gamma(\mathbf{r}_1,\mathbf{r}_2,\tau)$ is more robust in quantifying coherence. In writing Eq. (73) and similarly Eq. (72), one assumes that the optical disturbance is statistically stationary, at least in the wide sense. This means that the average optical disturbance has no explicit time dependence; instead,

the MCF $\Gamma(\mathbf{r}_1, \mathbf{r}_2, \tau)$ depends only on time difference, $\tau = t_2 - t_1$, not the actual values of t_1 and t_2. Physically, this is analogous to steady-state/continuous-wave operation of the optical source [13].

In writing Eq. (73), one also assumes that the optical disturbance is emanating from an extended source, so that both temporal and spatial coherence effects play a role. Temporal coherence effects play a role in the definition of the MCF $\Gamma(\mathbf{r}_1, \mathbf{r}_2, \tau)$ because there is the potential for optical path-length differences between the extended source and the two points in space, $\mathbf{r}_1$ and $\mathbf{r}_2$. These optical path-length differences are negligible when there is symmetry between the extended source and the two points, $\mathbf{r}_1$ and $\mathbf{r}_2$, and when the light is quasimonochromatic or narrowband, such that $\Delta\omega \ll \bar{\omega}$, where $\bar{\omega}$ is the mean angular frequency of the optical disturbance [13, 29]. When these conditions are met, the analysis treats the temporal properties within the MCF $\Gamma(\mathbf{r}_1, \mathbf{r}_2, \tau)$ separately, viz.,

$$\Gamma(\mathbf{r}_1, \mathbf{r}_2, \tau) \approx J(\mathbf{r}_1, \mathbf{r}_2) \exp(j\bar{\omega}\tau) \tag{74}$$

and

$$J(\mathbf{r}_1, \mathbf{r}_2) = \Gamma(\mathbf{r}_1, \mathbf{r}_2, \tau = 0) = \langle u(\mathbf{r}_1, t) u^*(\mathbf{r}_2, t) \rangle . \tag{75}$$

As such, the mutual intensity $J(\mathbf{r}_1, \mathbf{r}_2)$ gives a distinct gauge for spatial coherence provided the two points in space, $\mathbf{r}_1$ and $\mathbf{r}_2$, situate themselves within the spatial coherence area, $A_c \approx (\bar{\lambda})^2 / \Omega_s$, where $\bar{\lambda}$ is the mean wavelength of the optical disturbance and Ω_s is the solid angle subtended from the extended source to the two

points [13, 29]. The process used to measure spatial coherence helps in explaining this point further.

When spatial coherence is of concern, one would want to interfere the light from an extended source with a spatially shifted, but not delayed version of itself [29]. This type of interference requires wavefront splitting at two separate points. The Young's double slit experiment achieves this type of interference and is readily described throughout the optics literature—the treatments of Goodman and Wolf are particularly insightful [13, 29]. In the detection plane of Young's double slit experiment, the irradiance $I(\mathbf{r},\tau)$ scales with the MCF $\Gamma(\mathbf{r}_1,\mathbf{r}_2,\tau)$, and if the setup allows for it, the irradiance $I(\mathbf{r})$ scales with the mutual intensity $J(\mathbf{r}_1,\mathbf{r}_2)$. This says that an individual can measure spatial coherence through the interference of light.

2.5.3 Complex degree of coherence

Normalizing the MCF $\Gamma(\mathbf{r}_1,\mathbf{r}_2,\tau)$, as given in Eq. (73), an individual obtains a quantity referred to as the complex degree of coherence (CDoC) $\gamma(\mathbf{r}_1,\mathbf{r}_2,\tau)$, where

$$\gamma(\mathbf{r}_1,\mathbf{r}_2,\tau)=\frac{\Gamma(\mathbf{r}_1,\mathbf{r}_2,\tau)}{\sqrt{\Gamma(\mathbf{r}_1,\mathbf{r}_1,\tau=0)\Gamma(\mathbf{r}_2,\mathbf{r}_2,\tau=0)}}. \tag{76}$$

Note that the complex degree of (self) coherence $\gamma(\mathbf{r},\tau)$ follows from Eq. (72) when dealing with a single point in space $\mathbf{r}$ [29], and similarly, the (equal-time) complex degree of coherence $j(\mathbf{r}_1,\mathbf{r}_2)$ follows from Eq. (75) when dealing with symmetry in the optical setup and narrowband light [13]. Furthermore, one can relate the visibility

$V(\mathbf{r},\tau)$ of the irradiance $I(\mathbf{r},\tau)$, detected in their respective interferometer, to the CDoC $\gamma(\mathbf{r}_1,\mathbf{r}_2,\tau)$ using the following relationship [13, 29]:

$$V(\mathbf{r},\tau)=\frac{\max\left[I(\mathbf{r},\tau)\right]-\min\left[I(\mathbf{r},\tau)\right]}{\max\left[I(\mathbf{r},\tau)\right]+\min\left[I(\mathbf{r},\tau)\right]}=\left|\gamma(\mathbf{r}_1,\mathbf{r}_2,\tau)\right|. \tag{77}$$

Together, Eqs. (76) and (77) say that the magnitude of the CDoC $\left|\gamma(\mathbf{r}_1,\mathbf{r}_2,\tau)\right|$ provides a normalized unit of measure for the amount of coherence (temporal or spatial) in an optical disturbance at two points in space, $\mathbf{r}_1$ and $\mathbf{r}_2$, and some time difference $\tau=t_2-t_1$. For example, if $\left|\gamma(\mathbf{r}_1,\mathbf{r}_2,\tau)\right|=1$, two different points in space are correlated and the optical disturbance is fully coherent; however, if $\left|\gamma(\mathbf{r}_1,\mathbf{r}_2,\tau)\right|=0$, two different points in space are uncorrelated and the optical disturbance is incoherent. A partially coherent optical disturbance then satisfies $0<\left|\gamma(\mathbf{r}_1,\mathbf{r}_2,\tau)\right|<1$.

2.5.4 Cross-spectral density

The cross-spectral density (CSD) $W(\mathbf{r}_1,\mathbf{r}_2,\omega)$ is an alternative way of analyzing spatial coherence [13]. Explicitly,

$$\Gamma(\mathbf{r}_1,\mathbf{r}_2,\tau)=\frac{1}{2\pi}\int_0^\infty W(\mathbf{r}_1,\mathbf{r}_2,\omega)\exp(j\omega\tau)\,d\tau \tag{78}$$

and

$$W(\mathbf{r}_1,\mathbf{r}_2,\omega)=\int_{-\infty}^{\infty}\Gamma(\mathbf{r}_1,\mathbf{r}_2,\tau)\exp(-j\omega\tau)\,d\tau, \tag{79}$$

such that the MCF $\Gamma(\mathbf{r}_1,\mathbf{r}_2,\tau)$ and the CSD $W(\mathbf{r}_1,\mathbf{r}_2,\omega)$ form a Fourier transform pair. This says that the CSD $W(\mathbf{r}_1,\mathbf{r}_2,\omega)$ is a way to analyze spatial coherence in the space-

frequency domain as opposed to the space-time domain with the MCF $\Gamma(\mathbf{r}_1, \mathbf{r}_2, \tau)$. Moreover, Wolf derives the following result [13]:

$$W(\mathbf{r}_1, \mathbf{r}_2, \omega) = \langle U(\mathbf{r}_1, \omega) U^*(\mathbf{r}_2, \omega) \rangle, \tag{80}$$

which says that the CSD $W(\mathbf{r}_1, \mathbf{r}_2, \omega)$ is the cross correlation function of an ensemble $\{U(\mathbf{r}, \omega)\}$ of sample functions $U(\mathbf{r}, \omega)$. These sample functions are the space- and angular-frequency-dependent part of a monochromatic optical disturbance, i.e., $u(\mathbf{r}, t) = U(\mathbf{r}, \omega) \exp(j\omega t)$.

It is import to remember that, in general, the Fourier transform of an optical disturbance does not exist because it is not absolutely integrable. However, the Wiener-Khintchine theorem states that for a random process that is zero mean and at least wide-sense stationary, the autocorrelation and the spectral density form a Fourier transform pair [13, 29]. This is an important point in the analysis because when dealing with a single point in space $\mathbf{r}$, Eq. (80) reduces to an expression for the spectral density $S(\mathbf{r}, \omega)$, where

$$S(\mathbf{r}, \omega) = W(\mathbf{r}, \mathbf{r}, \omega) = \langle U(\mathbf{r}, \omega) U^*(\mathbf{r}, \omega) \rangle. \tag{81}$$

Thus, the spectral density $S(\mathbf{r}, \omega)$ is a way to analyze self coherence in the space-frequency domain as opposed to the space-time domain with the self-coherence function $\Gamma(\mathbf{r}, \tau)$. The process used to measure spatial coherence in the space-frequency domain helps in explaining this point further.

When measuring spatial coherence in the space-frequency domain, one again uses Young's double slit experiment. Narrow-band filters placed behind the slits ensure that

the optical disturbances emanating are space- and angular-frequency-dependent ensembles, $\{U(\mathbf{r}_1,\omega)\}$ and $\{U(\mathbf{r}_2,\omega)\}$. This allows an individual to consider the spectrum of the light in the detection plane instead of irradiance. Specifically, one can measure the spectral density $S(\mathbf{r},\omega)$. Wolf shows that in the detection plane of this modified Young's double slit experiment [13], the spectral density $S(\mathbf{r},\omega)$ scales with the CSD $W(\mathbf{r}_1,\mathbf{r}_2,\omega)$. This says that an individual can measure spatial coherence through the interference of light in the space-frequency domain.

2.5.5 Spectral degree of coherence

Normalizing the CSD $W(\mathbf{r}_1,\mathbf{r}_2,\omega)$, as given in Eq. (80), an individual obtains a quantity referred to as the spectral degree of coherence (SDoC) $\mu(\mathbf{r}_1,\mathbf{r}_2,\omega)$, where

$$\mu(\mathbf{r}_1,\mathbf{r}_2,\omega)=\frac{W(\mathbf{r}_1,\mathbf{r}_2,\omega)}{\sqrt{W(\mathbf{r}_1,\mathbf{r}_1,\omega)W(\mathbf{r}_2,\mathbf{r}_2,\omega)}}. \tag{82}$$

As such, one can then relate the visibility $V(\mathbf{r},\omega)$ of the spectral density $S(\mathbf{r},\omega)$, detected in the modified Young's double slit experiment, to the SDoC $\mu(\mathbf{r}_1,\mathbf{r}_2,\omega)$ using the following relationship [13]:

$$V(\mathbf{r},\omega)=\frac{\max\left[S(\mathbf{r},\omega)\right]-\min\left[S(\mathbf{r},\omega)\right]}{\max\left[S(\mathbf{r},\omega)\right]+\min\left[S(\mathbf{r},\omega)\right]}=\left|\mu(\mathbf{r}_1,\mathbf{r}_2,\omega)\right|. \tag{83}$$

Provided Eqs. (82) and (83), the magnitude of the SDoC $\left|\mu(\mathbf{r}_1,\mathbf{r}_2,\omega)\right|$ provides a normalized unit of measure for the amount of spatial coherence in an optical disturbance at two points in space, $\mathbf{r}_1$ and $\mathbf{r}_2$, and angular frequency ω. For instance, if

$\left|\mu(\mathbf{r}_1,\mathbf{r}_2,\omega)\right|=1$, two different points in space are correlated and the optical disturbance is spatially coherent; however, if $\left|\mu(\mathbf{r}_1,\mathbf{r}_2,\omega)\right|=0$, two different points in space are uncorrelated and the optical disturbance is spatially incoherent. A spatially partially coherent optical disturbance then satisfies $0<\left|\mu(\mathbf{r}_1,\mathbf{r}_2,\omega)\right|<1$.

2.5.6 Gaussian Schell-model source

Referencing Figure 7, in the source plane at $v=0$, the CSD $W(\mathbf{r}_1,\mathbf{r}_2,\omega)$ takes the following form:

$$W(\boldsymbol{\rho}_1,\boldsymbol{\rho}_2,\omega)=\left\langle U(\boldsymbol{\rho}_1,\omega)U^*(\boldsymbol{\rho}_2,\omega)\right\rangle, \tag{84}$$

where $\boldsymbol{\rho}_{1,2}=x_{1,2}\hat{\mathbf{x}}+u_{1,2}\hat{\mathbf{u}}$. Consequently, the CSD $W(\boldsymbol{\rho}_1,\boldsymbol{\rho}_2,\omega)$ of a Gaussian Schell-model (GSM) source takes the following form [13]:

$$W(\boldsymbol{\rho}_1,\boldsymbol{\rho}_2,\omega)=\sqrt{S(\boldsymbol{\rho}_1,\omega)}\sqrt{S(\boldsymbol{\rho}_2,\omega)}\mu(\boldsymbol{\rho}_2-\boldsymbol{\rho}_1,\omega), \tag{85}$$

such that

$$S(\boldsymbol{\rho},\omega)=A^2\exp\left[-\frac{2|\boldsymbol{\rho}|^2}{w^2}\right] \tag{86}$$

and

$$\mu(\boldsymbol{\rho},\omega)=\exp\left[-\frac{2|\boldsymbol{\rho}|^2}{\ell^2}\right]. \tag{87}$$

Note that the parameters A^2, w, and ℓ are space independent but are, in general, dependent on angular frequency ω. This dependence is omitted for brevity in the notation. Also note that upon substituting Eq. (85) into Eq. (82), the magnitude of the SDoC $\left|\mu(\boldsymbol{\rho}_2,\boldsymbol{\rho}_1,\omega)\right|$ becomes

$$\left|\mu(\boldsymbol{\rho}_2,\boldsymbol{\rho}_1,\omega)\right| = \left|\mu(\boldsymbol{\rho}_2-\boldsymbol{\rho}_1,\omega)\right| = \exp\left(-\frac{2\left|\boldsymbol{\rho}_2-\boldsymbol{\rho}_1\right|^2}{\ell^2}\right), \tag{88}$$

which depends only on the distance between two points and not on the points themselves. This is the classic characteristic of a Schell-model source [13].

Similar to the Gaussian laser beam source [20], the three parameters A^2, w, and ℓ physically describe the GSM source. For instance, the source beam width w is the radial distance $|\boldsymbol{\rho}|$ where the source magnitude A^2 falls to $1/e^2$ its initial on-axis value. This gives a nice gauge for the physical size of the emanating beam. Likewise, the source coherence length ℓ is the distance between two points $|\boldsymbol{\rho}_2-\boldsymbol{\rho}_1|$ where the magnitude of the SDoC $\left|\mu(\boldsymbol{\rho}_2,\boldsymbol{\rho}_1,\omega)\right|$ falls to $1/e^2$ its initial on-axis value. This is a direct result of the relationship found in Eq. (88). In practice, if $|\boldsymbol{\rho}_2-\boldsymbol{\rho}_1| \ll \ell$, then the two points are correlated and the GSM source is spatially coherent; conversely, if $|\boldsymbol{\rho}_2-\boldsymbol{\rho}_1| \gg \ell$, then the two points are uncorrelated and the GSM source is spatially incoherent. Partial spatial coherence then satisfies $0 < |\boldsymbol{\rho}_2-\boldsymbol{\rho}_1| < \ell$.

In using the GSM source formulated in Eqs. (85)-(87), the analysis is tractable for a variety of fields of practical interest. For example, the GSM source reduces to a point source when the source beam width approaches zero, $w \to 0$, or a plane wave when the source beam width approaches infinity, $w \to \infty$. One can also use the GSM source to model spatially coherent Gaussian laser beams. Here, an individual allows the source coherence radius to approach infinity, $\ell \to \infty$. On the other hand, when the source coherence radius approaches zero, $\ell \to 0$, one obtains a spatially incoherent Gaussian

beam source. This simplicity and versatility makes the GSM source ideal for investigations concerned with spatial coherence.

2.5.7 Cross-spectral density matrix

When analyzing spatial coherence in the space-frequency domain with electromagnetic vector fields, one uses the cross-spectral density matrix (CSDM) $\ddot{\mathbf{W}}(\mathbf{r}_1,\mathbf{r}_2,\omega)$ [13]. In general, the cross-spectral density matrix CSDM $\ddot{\mathbf{W}}(\mathbf{r}_1,\mathbf{r}_2,\omega)$ is the dyadic (outer product) created from electric field vectors of the following form:

$$\begin{aligned}\mathbf{E}(\mathbf{r}_l,\omega) &= E_x(\mathbf{r}_l,\omega)\,\hat{\mathbf{x}} + E_u(\mathbf{r}_l,\omega)\,\hat{\mathbf{u}} \quad (l=1,2)\\ &= \begin{bmatrix} E_x(\mathbf{r}_l,\omega) \\ E_u(\mathbf{r}_l,\omega)\end{bmatrix} \quad (l=1,2)\end{aligned}, \tag{89}$$

such that

$$\begin{aligned}\ddot{\mathbf{W}}(\mathbf{r}_1,\mathbf{r}_2,\omega) &\equiv \left\langle \mathbf{E}(\mathbf{r}_1,\omega)\,\mathbf{E}^{\dagger}(\mathbf{r}_2,\omega)\right\rangle\\ &= \left\langle \begin{bmatrix} E_x(\mathbf{r}_1,\omega) \\ E_u(\mathbf{r}_1,\omega)\end{bmatrix}\begin{bmatrix} E_x^*(\mathbf{r}_2,\omega) & E_u^*(\mathbf{r}_2,\omega)\end{bmatrix}\right\rangle\\ &= \begin{bmatrix} \left\langle E_x(\mathbf{r}_1,\omega)\,E_x^*(\mathbf{r}_2,\omega)\right\rangle & \left\langle E_x(\mathbf{r}_1,\omega)\,E_u^*(\mathbf{r}_2,\omega)\right\rangle \\ \left\langle E_u(\mathbf{r}_1,\omega)\,E_x^*(\mathbf{r}_2,\omega)\right\rangle & \left\langle E_u(\mathbf{r}_1,\omega)\,E_u^*(\mathbf{r}_2,\omega)\right\rangle\end{bmatrix},\\ &= \left\langle E_{\mathrm{m}}(\mathbf{r}_1,\omega)\,E_{\mathrm{n}}^*(\mathbf{r}_2,\omega)\right\rangle \quad (\mathrm{m}=x,u;\ \mathrm{n}=x,u)\\ &= W_{\mathrm{mn}}(\mathbf{r}_1,\mathbf{r}_2,\omega) \quad (\mathrm{m}=x,u;\ \mathrm{n}=x,u)\end{aligned} \tag{90}$$

where † denotes Hermitian conjugate. In Eq. (89), $E_x(\mathbf{r}_l,\omega)$ and $E_u(\mathbf{r}_l,\omega)$ are members of statistical ensembles which are at least wide-sense stationary, and in referencing Figure 7, are analytic functions in two mutually orthogonal directions perpendicular to the direction of propagation, i.e., the *v* direction. This says that the vector-field result presented in Eq. (90) is analogous to the scalar-field result given above in Eq. (80).

Accordingly, the SD $S(\mathbf{r},\omega)$ and the SDoC $\mu(\mathbf{r}_1,\mathbf{r}_2,\omega)$ are determined from the CSDM $\ddot{\mathbf{W}}(\mathbf{r}_1,\mathbf{r}_2,\omega)$ using the following relationships [13]:

$$S(\mathbf{r},\omega)=\mathrm{Tr}\left\{\ddot{\mathbf{W}}(\mathbf{r},\mathbf{r},\omega)\right\} \tag{91}$$

and

$$\mu(\mathbf{r}_1,\mathbf{r}_2,\omega)=\frac{\mathrm{Tr}\left\{\ddot{\mathbf{W}}(\mathbf{r}_1,\mathbf{r}_2,\omega)\right\}}{\sqrt{\mathrm{Tr}\left\{\ddot{\mathbf{W}}(\mathbf{r}_1,\mathbf{r}_1,\omega)\right\}}\sqrt{\mathrm{Tr}\left\{\ddot{\mathbf{W}}(\mathbf{r}_2,\mathbf{r}_2,\omega)\right\}}}, \tag{92}$$

where $\mathrm{Tr}\{\cdots\}$ denotes the trace operation and $\mathbf{r}=\mathbf{r}_{1,2}$. This says that the vector-field result presented in Eqs. (91) and (92) directly relate to the scalar-field results given above in Eqs. (81)-(83). The magnitude of the SDoC $\left|\mu(\mathbf{r}_1,\mathbf{r}_2,\omega)\right|$ resulting from electromagnetic vector fields also provides a normalized unit of measure for the amount of spatial coherence, i.e., $0\le\left|\mu(\mathbf{r}_1,\mathbf{r}_2,\omega)\right|\le 1$.

Referencing Figure 7, the CSDM $\ddot{\mathbf{W}}(\mathbf{r}_1,\mathbf{r}_2,\omega)$ of a Gaussian Schell-model (GSM) source takes the following element-based form [13]:

$$W_{\mathrm{mn}}(\boldsymbol{\rho}_1,\boldsymbol{\rho}_2,\omega)=\sqrt{S_{\mathrm{m}}(\boldsymbol{\rho}_1,\omega)}\sqrt{S_{\mathrm{n}}(\boldsymbol{\rho}_2,\omega)}\mu_{\mathrm{mn}}(\boldsymbol{\rho}_2-\boldsymbol{\rho}_1,\omega)\quad(\mathrm{m}=x,u;\ \mathrm{n}=x,u), \tag{93}$$

such that

$$S_{\mathrm{m}}(\boldsymbol{\rho},\omega)=A_{\mathrm{m}}^2\exp\left[-\frac{2|\boldsymbol{\rho}|^2}{w_{\mathrm{m}}^2}\right]\quad(\mathrm{m}=x,u) \tag{94}$$

and

$$\mu_{\mathrm{mn}}(\boldsymbol{\rho}_2-\boldsymbol{\rho}_1,\omega)=B_{\mathrm{mn}}\exp\left[-\frac{2|\boldsymbol{\rho}_2-\boldsymbol{\rho}_1|^2}{\ell_{\mathrm{mn}}^2}\right]\quad(\mathrm{m}=x,u;\ \mathrm{n}=x,u). \tag{95}$$

Note that the element-based parameters A_{m}^2, w_{m}, B_{mn}, and ℓ_{mn} are space independent but are, in general, dependent on angular frequency ω. This dependence is omitted for brevity in the notation. Also note that the CSDM $\ddot{\mathbf{W}}(\mathbf{r}_1,\mathbf{r}_2,\omega)$ given in Eqs. (93)-(95) is

analogous to the scalar-field result given above in Eqs. (85)-(87); however, there are additional constraints, viz.,

$$B_{\mathrm{mn}} = 1 \quad \text{when m} = \text{n}\,, \tag{96}$$

$$\left|B_{\mathrm{mn}}\right| \le 1 \quad \text{when m} \ne \text{n}\,, \tag{97}$$

$$B_{\mathrm{mn}} = B_{\mathrm{nm}}^{*}\,, \tag{98}$$

and

$$\ell_{\mathrm{mn}} = \ell_{\mathrm{nm}}\,. \tag{99}$$

Nonetheless, the GSM source presented in Eqs. (93)-(99) is ideal for investigations concerned with spatial coherence.

2.6 Polarization

Given electromagnetic vector fields and the CSDM $\ddot{\mathbf{W}}\left(\mathbf{r}_1, \mathbf{r}_2, \omega\right)$, as defined above in Eq. (90), polarization relationships result. The first polarization relationship of interest is the space- and angular-frequency-dependent degree of polarization (DoP) $P\left(\mathbf{r}, \omega\right)$ [13]. Particularly,

$$P\left(\mathbf{r}, \omega\right) = \sqrt{1 - \frac{4\mathrm{Det}\left\{\ddot{\mathbf{W}}\left(\mathbf{r}, \mathbf{r}, \omega\right)\right\}}{\left(\mathrm{Tr}\left\{\ddot{\mathbf{W}}\left(\mathbf{r}, \mathbf{r}, \omega\right)\right\}\right)^2}}\,, \tag{100}$$

where again, $\mathrm{Det}\left\{\cdots\right\}$ denotes the determinant operation and $\mathbf{r} = \mathbf{r}_{1,2}$. In general, the DoP $P\left(\mathbf{r}, \omega\right)$ provides a normalized unit of measure for the amount of polarization in an optical disturbance [13, 30]. When $P\left(\mathbf{r}, \omega\right) = 1$, the optical disturbance is polarized, whereas when $P\left(\mathbf{r}, \omega\right) = 0$, the optical disturbance is unpolarized. Partial polarization then satisfies $0 < P\left(\mathbf{r}, \omega\right) < 1$.

The second polarization relationship of interest is the space- and angular-frequency-dependent angle of polarization (AOP) $\psi(\mathbf{r},\omega)$. Specifically,

$$\psi(\mathbf{r},\omega)=\frac{1}{2}\tan^{-1}\left(\frac{2\,\mathrm{Re}\{W_{xu}(\mathbf{r},\mathbf{r},\omega)\}}{W_{xx}(\mathbf{r},\mathbf{r},\omega)-W_{uu}(\mathbf{r},\mathbf{r},\omega)}\right),\quad(-\pi/2<\psi\le\pi/2). \tag{101}$$

This angle is depicted in Figure 8 in terms of a polarization ellipse. The semi-major and semi-minor axes of this ellipse satisfy the following relationships [13]:

$$\begin{aligned}a^2(\mathbf{r},\omega)=\frac{1}{8}\Big\{&\sqrt{4\left|W_{xu}(\mathbf{r},\mathbf{r},\omega)\right|^2+\left[W_{xx}(\mathbf{r},\mathbf{r},\omega)-W_{uu}(\mathbf{r},\mathbf{r},\omega)\right]^2}\\&-\sqrt{4\left[\mathrm{Re}\{W_{xu}(\mathbf{r},\mathbf{r},\omega)\}\right]^2+\left[W_{xx}(\mathbf{r},\mathbf{r},\omega)-W_{uu}(\mathbf{r},\mathbf{r},\omega)\right]^2}\Big\}\end{aligned} \tag{102}$$

and

$$\begin{aligned}b^2(\mathbf{r},\omega)=\frac{1}{8}\Big\{&\sqrt{4\left|W_{xu}(\mathbf{r},\mathbf{r},\omega)\right|^2+\left[W_{xx}(\mathbf{r},\mathbf{r},\omega)-W_{uu}(\mathbf{r},\mathbf{r},\omega)\right]^2}\\&-\sqrt{4\left[\mathrm{Re}\{W_{xu}(\mathbf{r},\mathbf{r},\omega)\}\right]^2+\left[W_{xx}(\mathbf{r},\mathbf{r},\omega)-W_{uu}(\mathbf{r},\mathbf{r},\omega)\right]^2}\Big\}\end{aligned}, \tag{103}$$

respectively. As such, the space- and angular-frequency-dependent ellipticity $\varepsilon(\mathbf{r},\omega)$ follows as

$$\varepsilon(\mathbf{r},\omega)=\frac{b(\mathbf{r},\omega)}{a(\mathbf{r},\omega)}=\tan[\chi(\mathbf{r},\omega)],\quad(-\pi/4<\chi\le\pi/4), \tag{104}$$

where $\chi(\mathbf{r},\omega)$ is the ellipticity angle, which is also depicted in Figure 8. In general, the ellipticity $\varepsilon(\mathbf{r},\omega)$ provides a normalized unit of measure for the polarization state of the optical disturbance [23, 30]. When $\varepsilon(\mathbf{r},\omega)=1$, the semi-major and semi-minor axes of the polarization ellipse equal each other, i.e., $a(\mathbf{r},\omega)=b(\mathbf{r},\omega)$. This corresponds to a circularly polarized optical disturbance. On the other hand, when $\varepsilon(\mathbf{r},\omega)=0$, the semi-

minor axis of the polarization ellipse equals zero, i.e., $b(\mathbf{r},\omega)=0$. This corresponds to a linearly polarized optical disturbance. An elliptically polarized optical disturbance then satisfies $0<\varepsilon(\mathbf{r},\omega)<1$.

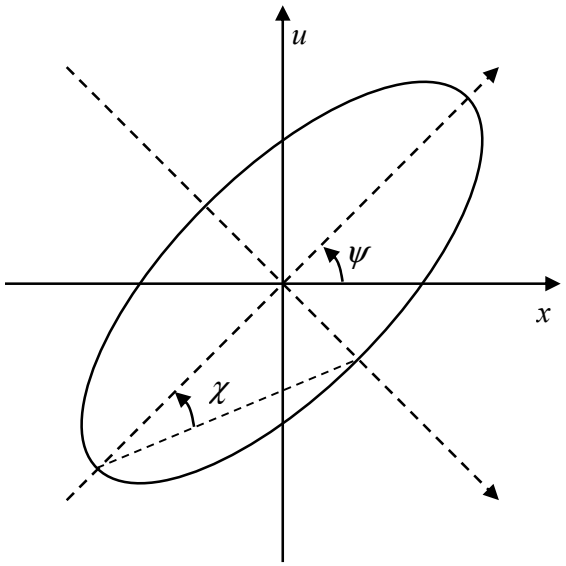

Figure 8. A description of the polarization geometry used in the analysis.

The third polarization relationship of interest is the angular-frequency-dependent two-point Stokes vector $\mathbf{s}(\mathbf{r}_1,\mathbf{r}_2,\omega)$ [13]. Per se, the components of this vector satisfy the following relationships:

$$\left.\begin{aligned} s_0(\mathbf{r}_1,\mathbf{r}_2,\omega) &= W_{xx}(\mathbf{r}_1,\mathbf{r}_2,\omega)+W_{uu}(\mathbf{r}_1,\mathbf{r}_2,\omega) \\ s_1(\mathbf{r}_1,\mathbf{r}_2,\omega) &= W_{xx}(\mathbf{r}_1,\mathbf{r}_2,\omega)-W_{uu}(\mathbf{r}_1,\mathbf{r}_2,\omega) \\ s_2(\mathbf{r}_1,\mathbf{r}_2,\omega) &= W_{xu}(\mathbf{r}_1,\mathbf{r}_2,\omega)+W_{ux}(\mathbf{r}_1,\mathbf{r}_2,\omega) \\ s_3(\mathbf{r}_1,\mathbf{r}_2,\omega) &= j\left[W_{ux}(\mathbf{r}_1,\mathbf{r}_2,\omega)-W_{xu}(\mathbf{r}_1,\mathbf{r}_2,\omega)\right] \end{aligned}\right\} \tag{105}$$

or

$$\left.\begin{aligned} s_0(\mathbf{r}_1,\mathbf{r}_2,\omega) &= \left\langle E_x(\mathbf{r}_1,\omega)E_x^*(\mathbf{r}_2,\omega)\right\rangle+\left\langle E_u(\mathbf{r}_1,\omega)E_u^*(\mathbf{r}_2,\omega)\right\rangle \\ s_1(\mathbf{r}_1,\mathbf{r}_2,\omega) &= \left\langle E_x(\mathbf{r}_1,\omega)E_x^*(\mathbf{r}_2,\omega)\right\rangle-\left\langle E_u(\mathbf{r}_1,\omega)E_u^*(\mathbf{r}_2,\omega)\right\rangle \\ s_2(\mathbf{r}_1,\mathbf{r}_2,\omega) &= \left\langle E_x(\mathbf{r}_1,\omega)E_u^*(\mathbf{r}_2,\omega)\right\rangle+\left\langle E_u(\mathbf{r}_1,\omega)E_x^*(\mathbf{r}_2,\omega)\right\rangle \\ s_3(\mathbf{r}_1,\mathbf{r}_2,\omega) &= j\left[\left\langle E_u(\mathbf{r}_1,\omega)E_x^*(\mathbf{r}_2,\omega)\right\rangle-\left\langle E_x(\mathbf{r}_1,\omega)E_u^*(\mathbf{r}_2,\omega)\right\rangle\right] \end{aligned}\right\}. \tag{106}$$

History shows that the single point Stokes vector $\mathbf{s}(\mathbf{r},\mathbf{r},\omega)$, where $\mathbf{r}=\mathbf{r}_{1,2}$, is a very versatile tool in terms of analyzing polarization [23, 30]. For example,

$$P(\mathbf{r},\omega)=\frac{\sqrt{s_1^2(\mathbf{r},\mathbf{r},\omega)+s_2^2(\mathbf{r},\mathbf{r},\omega)+s_3^2(\mathbf{r},\mathbf{r},\omega)}}{s_0(\mathbf{r},\mathbf{r},\omega)}, \tag{107}$$

which says that one can obtain the DoP $P(\mathbf{r},\omega)$ two separate ways within the analysis.

3 Background rough surface scattering literature review

As mentioned in Chapter 1, the purpose of this dissertation is to extend the rough surface scattering literature to include the effects of partially coherent electromagnetic beam illumination. In support, recent publications derived a 2D scalar-equivalent solution for the scattering of partially coherent beams from statistically rough surfaces using the physical-optics (PO) approximation [10, 11]. These publications serve as the basis for this dissertation; however, modern-day research in rough surface scattering dates back to the work of Lord Rayleigh around the turn of the 20th century [31-33]. With this said, one can distinguish the published literature in rough surface scattering into two main categories. The first category deals with the research predominately concerned with the scattering of fully coherent and fully incoherent illumination from rough surfaces, whereas the second category deals with the research predominately concerned with the scattering of partially coherent illumination from rough surfaces.

3.1 Fully coherent and fully incoherent illumination

Several different research communities come to mind when reviewing the rough surface scattering literature pertaining to fully coherent and fully incoherent illumination. The first couple identify themselves with the rough surface scattering research performed by the optics and photonics communities for metrology and manufacturing applications. The text written by Stover highlights this point [34]. Conversely, the second couple identify themselves with the rough surface scattering research performed by the radio-frequency/microwave and visible/near-infrared communities for synthetic aperture radar and remote sensing applications. The three-volume text by Ulaby *et al*. highlights this point [35]. With some exceptions, the common approaches employed by these research

communities are the geometrical-optics (GO), linear-systems, perturbation, PO, and full-wave methods. One may refer to works of Beckmann and Spizzichino [36], Ishimaru [37], Ogilvy [38], Voronovich [39], Warnick and Chew [40], Elfouhaily and Guérin [41], Nieto-Vesperinas [42], Maradudin [43], and Fung and Chen [44], for excellent summaries on rough surface scattering techniques using fully coherent and fully incoherent illumination.

3.1.1 Geometrical-optics methods

When employing GO methods, one typically uses a bidirectional reflectance distribution function (BRDF) or its polarimetric counterpart, a polarimetric BRDF (pBRDF), to model rough surface scattering. Nicodemus was the first to introduce the BRDF in 1965 [45]. Defined in radiometric terms, the BRDF is the reflected radiance divided by the incident irradiance [34]. As such, the BRDF typically characterizes how light reflects from surfaces in terms of a specular and diffuse component or a polarized and unpolarized component [46]. Both empirical and analytical BRDFs exist in practice. Measurements help in formulating empirical BRDFs. For example, in preparation for the NASA Apollo missions, the analysis of light scattered from the lunar surface led researchers to conclude that the moon's surface is composed of a particulate material [47]. On the other hand, both PO and GO approximations help in formulating analytical BRDFs [22]. Using the GO approximation, the seminal BRDF paper is that of Torrance and Sparrow [48], whereas the oft-referenced pBRDF paper is that of Priest and Meier [49]. Many other models exist based on their work. These include BRDFs for applications in passive visible/near-infrared remote sensing [50] and computer graphics [51]—Sun's literature review is particularly insightful [52].

3.1.2 Linear-systems methods

In the late 1970s, Harvey and Shack developed a linear-systems formulation of rough surface scattering based on scalar diffraction theory [53-55]. In this approach, a surface transfer function characterizes the scattering process much like the optical transfer function does for aberrations found within an imaging system. The Fourier transform of this surface transfer function then yields a scattered radiance distribution function closely related to the BRDF. In the late 1980's, Harvey *et al*. modified this theory to include the effects of grazing incidence at X-ray wavelengths [56]. This helped in the design of X-ray telescopes. Most recently, Krywonos *et al.* modified the theory once again to a non-paraxial regime [57, 58]. This scalar non-paraxial linear-systems formulation of rough surface scattering claims to produce accurate results for rougher surfaces than the theories based on perturbation methods and for larger incident and scattered angles than the theories based on PO methods [59-61].

3.1.3 Perturbation methods

The perturbation approach to rough surface scattering models the surface roughness as a small perturbation relative to the case of a perfectly smooth surface. As such, this approach requires that the surface roughness be small compared to the wavelength of the incident radiation [37]. The literature credits Rice with the groundbreaking paper on this subject [62]; however, it is important to note that Lord Rayleigh initiated the use of many of the mathematical techniques [31-33]. Thus, the literature often refers to the perturbation formulation of rough surface scattering as Rayleigh-Rice theory. It is also important to note that different approaches found within the literature tend to yield similar results up to a fifth-order perturbation expansion [63];

nonetheless, perturbation methods are the oldest and most widely used in the rough surface scattering literature.

3.1.4 Physical-optics methods

The PO approach to rough surface scattering uses the PO approximation [14, 22], which is analogous to using Kirchhoff boundary conditions in physical or wave optics [23, 24]. This is done so that instead of satisfying the exact boundary conditions, as is done with perturbation methods, the field and its normal derivative simplify on the scattering surface. Accordingly, this approach does not require that the surface roughness be small compared to the wavelength of the incident radiation [35]. The literature typically credits Beckmann with the trailblazing work on this subject [36], and one often sees the title of Beckmann-Kirchhoff theory or the Kirchhoff approximation used in practice. It is important to note that the PO approximation typically allows an individual to calculate closed-form expressions where other approximations/theories would not. Such is the case when considering the scattering of fully coherent laser beam illumination from rough surfaces [64-68].

3.1.5 Full-wave methods

When employing full-wave methods, one typically uses the method of moments [14, 19, 21], the finite difference time domain [19, 69, 70], or the finite element method [19, 71, 72] to satisfy Maxwell's equations and model rough surface scattering. This problem has a rich history that dates back to the late 1970's. Some of the early notable work in this field is that of Bahar [73-76], Axline and Fung [77], Thorsos [78], and Collin [79, 81]. The topical review written by Warnick and Chew outlines many such full-wave techniques [40].

3.2 Partially coherent illumination

The rough surface scattering literature pertaining to partially coherent illumination is the sole result of the proliferation of laser-based systems, such as those found in active-illumination systems for directed-energy and remote-sensing applications [82-85]. In recent times, the statistical behaviors of the laser-target interaction; in particular, the resulting speckle patterns, gained considerable interest. Since the presence of speckle is typically detrimental in applications involving coherent light, techniques for suppressing speckle naturally followed. Some of the early notable literature in such fields as metrology and remote sensing include the research efforts of Dainty [86], Fujii and Asakura [87, 88], Pedersen [89], Goodman [90], Parry [91], and Yoshimura *et al*. [92]. A recent text written by Goodman reviews many such techniques [93].

One way to suppress speckle in active-illumination systems is to use partially coherent light instead of fully coherent laser light. As a result, this research topic is becoming more and more popular due predominately to the work of Wolf in creating his unified theory of coherence and polarization [12, 13]. This unified theory helps in explaining correlation-induced changes in coherence, polarization, and spectrum of partially coherent light. In particular, much of the published literature uses the properties of a partially coherent electromagnetic beam whose cross-spectral density matrix possesses a Gaussian Schell-model (GSM) form [13]. As the name implies, Schell was the first to conjecture such an electromagnetic source in 1961 [94, 95]. Since then, much effort has gone into understanding the physics behind GSM sources/beams. Some of the published literature includes research in realizability conditions [96-98], experimental generation [98-100], numerical simulation [102-104], free-space propagation [105-107],

turbulent propagation [108-110], or sources/beams of similar form [111-113]. The topical review written by Gbur and Visser [114] and a recent text written by Korotkova [115] are most thorough in review.

In regards to the scattering of partially coherent illumination, most of the current literature deals with the scattering from low-contrast surfaces, i.e., where the index of refraction differs only slightly from unity [116-125]. These are scattering surfaces in which the Born approximation is valid [13, 23, 114, 115]—the topical review written by Zhao and Wang thoroughly reviews this problem [126]. In view of this, there are far fewer publications on the scattering of partially coherent illumination from rough surfaces. Of the published work to date, the following approaches are common: the phase-screen model, the ABCD matrix formulation, and the coherent-mode representation.

3.2.1 Phase-screen methods

In 1975, Goodman developed a phase-screen formulation of rough surface scattering based on scalar diffraction theory [90, 93]. In this approach, a phase-screen transmittance function characterizes the scattering process much like an aperture transmittance function does in physical or wave optics [24]. Hoover and Gamiz most recently employed this approach [127]. In so doing, Hoover and Gamiz assumed idealized quasimonochromatic plane-wave illumination. This allowed for the application of the generalized Van Cittert-Zernike (VCZ) theorem to the mutual intensity function on the phase-screen surface. The VCZ theorem relates the irradiance to the mutual intensity through a Fourier transform [13, 29]. Hoover and Gamiz's work ultimately lead to the formulation of a generalized BRDF solution which was the sum of a coherent and

incoherent component; however, their work did not directly account for partially coherent beam illumination.

3.2.2 ABCD-matrix methods

The text written by Andrews and Phillips best describes the principles behind the ABCD-matrix approach to rough surface scattering [128]. In general, the ABCD-matrix approach describes paraxial wave propagation through any complex optical system. When modeling the rough surface scattering using the ABCD-matrix approach, a phase-screen transmittance function again characterizes the scattering process. However, the inclusion of a soft-Gaussian aperture in the model accounts for the size of the scattering surface and accompanying diffraction effects. Korotkova discusses this point in her texts [115, 129]. The research of Hansen *et al*. [130] and Yura and Hanson [131] used this approach to look at rough surface scattering from a target which produced partially developed speckle. Wu and Cai also described an approach to sensing the scatter from rough surfaces using ABCD-matrix methods and partially coherent beam illumination via the GSM formulation [132]; however, this work is only applicable to small-angle scattering geometries with very rough surfaces [133-135].

3.2.3 Coherent-mode methods

The text written by Ostrovsky best describes the principles behind the coherent-mode approach to rough surface scattering [136]. Huttunen *et al*. used this approach along with the PO approximation to look at the scattering from two-dimensional micro-structured media [137], i.e., an isolated groove or slit in a perfectly conducting material substrate. This unique approach to rough surface scattering may prove useful for future research efforts.

4 Methodology for the 3D vector solution

Figure 1 describes the geometry used to obtain a 3D vector solution for the problem proposed above in Chapter 1. As shown, a zero mean 2D sample function $h = h(x, y)$ describes the surface height at the rough interface with standard deviation σ_h and correlation length ℓ_h. This gives rise to a statistically rough surface S. Spatially partially coherent electromagnetic beam illumination (parameters given below) emanates from the source plane specified by the coordinates (x, u, v), which are different from the surface-plane coordinates (x, y, z). As such, the vector, $\boldsymbol{\rho} = x\hat{\mathbf{x}} + u\hat{\mathbf{u}}$, points from the source plane origin to a transverse beam location since $v = 0$ in the source plane; the vector, $\mathbf{r}_s = 0\hat{\mathbf{x}} - y_s\hat{\mathbf{y}} + z_s\hat{\mathbf{z}}$, points from the source-plane origin to the surface-plane origin; and the vector, $\mathbf{r} = x\hat{\mathbf{x}} + y\hat{\mathbf{y}} + z\hat{\mathbf{z}}$, points from the surface plane origin to an observation point. Note that in the source and the surface planes, the x axes align, which assumes that the surface of the homogeneous medium is statistically isotropic [38, 43] with impedance η. Above, the medium is free space with impedance η_0.

4.1 Incident field cross-spectral density matrix

As mentioned above, spatially partially coherent electromagnetic beam illumination emanates from the source plane. With this in mind, the analysis uses a Gaussian Schell-model (GSM) form for the incident field cross-spectral density matrix (CSDM) $\ddot{\mathbf{W}}^i(\boldsymbol{\rho}_1, \boldsymbol{\rho}_2)$ [13, 94], such that

$$
\begin{aligned}
\vec{\vec{\mathbf{W}}}^{i}\left(\boldsymbol{\rho}_1,\boldsymbol{\rho}_2\right) &\equiv \left\langle \mathbf{E}^{i}\left(\boldsymbol{\rho}_1\right)\mathbf{E}^{i\dagger}\left(\boldsymbol{\rho}_2\right)\right\rangle \\
&= \begin{bmatrix} \left\langle E_x^{i}\left(\boldsymbol{\rho}_1\right)E_x^{i*}\left(\boldsymbol{\rho}_2\right)\right\rangle & \left\langle E_x^{i}\left(\boldsymbol{\rho}_1\right)E_u^{i*}\left(\boldsymbol{\rho}_2\right)\right\rangle \\ \left\langle E_u^{i}\left(\boldsymbol{\rho}_1\right)E_x^{i*}\left(\boldsymbol{\rho}_2\right)\right\rangle & \left\langle E_u^{i}\left(\boldsymbol{\rho}_1\right)E_u^{i*}\left(\boldsymbol{\rho}_2\right)\right\rangle \end{bmatrix} \\
&= W_{\mathrm{mn}}^{i}\left(\boldsymbol{\rho}_1,\boldsymbol{\rho}_2\right) \quad \left(\mathrm{m}=x,u;\ \mathrm{n}=x,u\right) \\
&= A_{\mathrm{m}}\exp\left(-\frac{\left|\boldsymbol{\rho}_1\right|^2}{4w_s^2}\right)A_{\mathrm{n}}\exp\left(-\frac{\left|\boldsymbol{\rho}_2\right|^2}{4w_s^2}\right)B_{\mathrm{mn}}\exp\left(-\frac{\left|\boldsymbol{\rho}_2-\boldsymbol{\rho}_1\right|^2}{2\ell_{\mathrm{mn}}^2}\right)
\end{aligned}
, \qquad (108)
$$

where $\langle\cdots\rangle$ denotes correlation, $\dagger$ denotes Hermitian conjugate, and $*$ denotes complex conjugate. In Eq. (108), the element-based parameters A_{m} and A_{n} are the beam amplitudes in the x and u directions, respectively, w_s is the source width, and the element-based parameters B_{mn} and $\ell_{\mathrm{mn}}=\ell_{\mathrm{nm}}$ are the correlation amplitude and correlation length, respectively. Note that B_{mn} follows additional constraints [13, 97]; namely,

$$
\begin{aligned}
B_{\mathrm{mn}} &= 1 \quad \text{when } \mathrm{m}=\mathrm{n} \\
\left|B_{\mathrm{mn}}\right| &\le 1 \quad \text{when } \mathrm{m}\neq\mathrm{n}\,. \\
B_{\mathrm{mn}} &= B_{\mathrm{nm}}^{*}
\end{aligned}
\qquad (109)
$$

Also note that, in general, the incident field $\mathbf{E}^{i}$ and the parameters A_{m}, w_s, ℓ_{mn}, and B_{mn} are radian frequency ω dependent [13]; however, the analysis omits this dependence for brevity in the notation[7].

7. The analysis presented in this chapter uses the MKS system of units in addition to the engineering sign convention for the time-harmonic variations (cf. Footnote 1, p. 5). In addition, some of the notation is simplified from that presented in Chapter 2, e.g., $\mathbf{E}^{inc}=\mathbf{E}^{i}$. This is done for brevity in the notation.

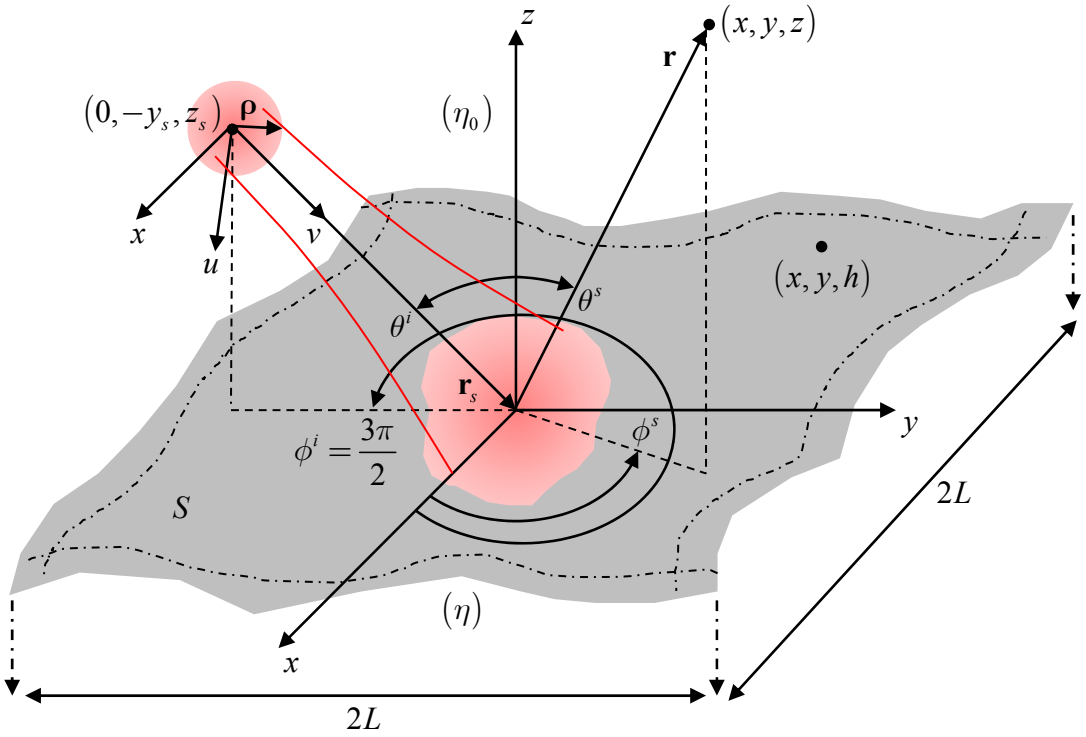

(a)

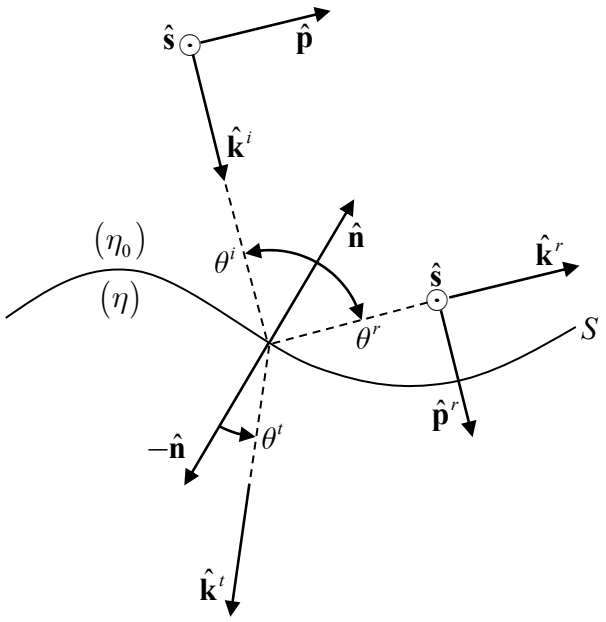

(b)

Figure 9. The macro-scale (a) and micro-scale (b) scattering geometry of a 2D statistically rough surface *S* of length 2*L* and width 2*L*.

4.2 Scattered field

The present analysis uses the PO approximation to develop a far-field expression for the scattered field $\mathbf{E}^s(\mathbf{r})$. For this purpose, one can write the incident field $\mathbf{E}^i(\mathbf{r})$ in terms of its spectrum $\mathbf{T}^i\left(k_x^i, k_u^i\right)$ using the plane-wave spectrum representation [25]. Using the macro-scale scattering geometry given in Figure 9a, the following expressions result:

$$\mathbf{E}^i(\mathbf{r}) = \frac{1}{(2\pi)^2} \int_{-\infty}^{\infty} \int_{-\infty}^{\infty} \mathbf{T}^i\left(k_x^i, k_u^i\right) \mathrm{e}^{-j\mathbf{k}^i \cdot \mathbf{r}_s} \, \mathrm{e}^{-j\mathbf{k}^i \cdot \mathbf{r}} \, dk_x^i dk_u^i \tag{110}$$

and

$$\mathbf{T}^i\left(k_x^i, k_u^i\right) = \int_{-\infty}^{\infty} \int_{-\infty}^{\infty} \mathbf{E}^i(\boldsymbol{\rho}) \mathrm{e}^{jk_x^i x} \mathrm{e}^{jk_u^i u} dx du \,, \tag{111}$$

which are valid in the source-free half space where $v \geq 0$. In Eqs. (110) and (111), $\mathbf{k}^i = k_0 \hat{\mathbf{k}}^i = k_x^i \hat{\mathbf{x}} + k_u^i \hat{\mathbf{u}} + k_v^i \hat{\mathbf{v}}$ is the incident propagation vector, $k_0 = 2\pi/\lambda_0$ is the free-space wavenumber, and λ_0 is the free-space wavelength.

For most directed-energy and remote-sensing engagement scenarios, all of the observation points of interest are in the far field. As such, the scattered electric field $\mathbf{E}^s(\mathbf{r})$ depends on the far-field vector potentials, $\mathbf{L}(\mathbf{r})$ and $\mathbf{N}(\mathbf{r})$, using the following relationships[8]:

$$\mathbf{E}^s(\mathbf{r}) \approx jk_0 \frac{\mathrm{e}^{-jk_0 r}}{4\pi r} \left[\left(\hat{\boldsymbol{\phi}}\hat{\boldsymbol{\theta}} - \hat{\boldsymbol{\theta}}\hat{\boldsymbol{\phi}} \right) \cdot \mathbf{L}(\mathbf{r}) - \eta_0 \left(\hat{\boldsymbol{\theta}}\hat{\boldsymbol{\theta}} + \hat{\boldsymbol{\phi}}\hat{\boldsymbol{\phi}} \right) \cdot \mathbf{N}(\mathbf{r}) \right], \tag{112}$$

8. In the far field, $r > 2D^2/\lambda_0$, where $D \approx 2L$ and $r \gg L$; consequently, the analysis neglects all contributions to the scattered field $\mathbf{E}^s$ that are in the radial $\hat{\mathbf{r}}$ direction because their contributions scale as $1/r^n$, where $n = 2, 3, \ldots$, and are negligible [14].

$$\mathbf{L}(\mathbf{r}) = \iint_S \mathbf{M}(\mathbf{r}') \mathrm{e}^{jk_0 \hat{\mathbf{r}} \cdot \mathbf{r}'} \, ds', \tag{113}$$

and

$$\mathbf{N}(\mathbf{r}) = \iint_S \mathbf{J}(\mathbf{r}') \mathrm{e}^{jk_0 \hat{\mathbf{r}} \cdot \mathbf{r}'} \, ds'. \tag{114}$$

In Eqs. (112)-(114), $\hat{\boldsymbol{\theta}}$ and $\hat{\boldsymbol{\phi}}$ are unit vectors in the polar (vertical polarization) and azimuth (horizontal polarization) directions, respectively, $\mathbf{M}(\mathbf{r}')$ and $\mathbf{J}(\mathbf{r}')$ are the equivalent surface current densities, respectively, and the vector, $\mathbf{r}' = x'\hat{\mathbf{x}} + y'\hat{\mathbf{y}} + h'\hat{\mathbf{z}}$, points from the surface-plane origin to a point on the statistically rough surface S.

Using the micro-scale scattering geometry given in Figure 9b and the PO approximation [14, 22],

$$\mathbf{M}(\mathbf{r}') \approx -\overleftrightarrow{\mathbf{M}}' \cdot \mathbf{E}^i(\mathbf{r}') \tag{115}$$

and

$$\mathbf{J}(\mathbf{r}') \approx \frac{1}{\eta_0} \overleftrightarrow{\mathbf{J}}' \cdot \mathbf{E}^i(\mathbf{r}'), \tag{116}$$

where $\overleftrightarrow{\mathbf{J}}'$ and $\overleftrightarrow{\mathbf{M}}'$ are dyadics, such that

$$\overleftrightarrow{\mathbf{J}}' = \hat{\mathbf{n}}' \times \left[\hat{\mathbf{s}}' \left(1 - r_{\parallel}'\right) \hat{\mathbf{p}}' - \hat{\mathbf{p}}' \left(1 - r_{\perp}'\right) \hat{\mathbf{s}}' \right] \tag{117}$$

and

$$\overleftrightarrow{\mathbf{M}}' = \hat{\mathbf{n}}' \times \left[\hat{\mathbf{s}}' \left(1 + r_{\perp}'\right) \hat{\mathbf{s}}' + \hat{\mathbf{p}}' \left(1 + r_{\parallel}'\right) \hat{\mathbf{p}}' \right]. \tag{118}$$

In Eqs. (117) and (118), $\hat{\mathbf{n}}' = \hat{\mathbf{n}}(x', y')$ is the 2D unit outward normal vector given by

$$\hat{\mathbf{n}}' = \frac{\mathbf{n}'}{|\mathbf{n}'|} = \frac{-h_{x'}\hat{\mathbf{x}} - h_{y'}\hat{\mathbf{y}} + \hat{\mathbf{z}}}{\sqrt{1 + h_{x'}^2 + h_{y'}^2}}, \tag{119}$$

where

$$h_{x'} = \frac{\partial h'}{\partial x'} = \frac{\partial h(x', y')}{\partial x'} \quad h_{y'} = \frac{\partial h'}{\partial y'} = \frac{\partial h(x', y')}{\partial y'}. \tag{120}$$

Furthermore, $\hat{\mathbf{s}}'$ and $\hat{\mathbf{p}}'$ are the unit perpendicular and parallel vectors, whereas $r_{\perp}'$ and $r_{\parallel}'$ are the corresponding Fresnel reflection coefficients, respectively. Referencing the micro-scale scattering geometry in Figure 9b, the following relationships result:

$$\hat{\mathbf{s}} = \frac{\hat{\mathbf{k}}^i \times \hat{\mathbf{n}}}{\left|\hat{\mathbf{k}}^i \times \hat{\mathbf{n}}\right|} \quad \hat{\mathbf{p}} = \hat{\mathbf{s}} \times \hat{\mathbf{k}}^i \quad \hat{\mathbf{p}}^r = -\hat{\mathbf{s}} \times \hat{\mathbf{k}}^r \,. \tag{121}$$

Thus, in arriving at the relationships found in Eqs. (117) and (118), one must use the GO approximation [22]; specifically the law of reflection, such that $-\hat{\mathbf{n}} \cdot \hat{\mathbf{k}}^i = \hat{\mathbf{n}} \cdot \hat{\mathbf{k}}^r$ [9].

Based on Eq. (119), it is important to note that the integration in Eqs. (113) and (114) is over the parameterized rough surface, i.e., $ds' = \left|\mathbf{n}'\right| dx'dy'$. Consequently, using Eq. (110) and substituting Eqs. (115)-(119) into Eqs. (113) and (114), one obtains the following expressions:

$$\mathbf{L}(\mathbf{r}) = -\frac{1}{(2\pi)^2} \int_{-L}^{L} \int_{-L}^{L} \int_{-\infty}^{\infty} \int_{-\infty}^{\infty} \vec{\mathbf{L}}' \cdot \mathbf{T}^i \left(k_x^i, k_u^i\right) \mathrm{e}^{-j\mathbf{k}^i \cdot \mathbf{r}_s} \, \mathrm{e}^{j\mathbf{q} \cdot \mathbf{r}'} dk_x^i dk_u^i dx'dy' \tag{122}$$

and

$$\mathbf{N}(\mathbf{r}) = \frac{1}{(2\pi)^2 \eta_0} \int_{-L}^{L} \int_{-L}^{L} \int_{-\infty}^{\infty} \int_{-\infty}^{\infty} \vec{\mathbf{N}}' \cdot \mathbf{T}^i \left(k_x^i, k_u^i\right) \mathrm{e}^{-j\mathbf{k}^i \cdot \mathbf{r}_s} \, \mathrm{e}^{j\mathbf{q} \cdot \mathbf{r}'} dk_x^i dk_u^i dx'dy' \,, \tag{123}$$

where $\mathbf{q} = k_0 \left(\hat{\mathbf{r}} - \hat{\mathbf{k}}^i\right) = q_x \hat{\mathbf{x}} + q_y \hat{\mathbf{y}} + q_z \hat{\mathbf{z}}$, $\vec{\mathbf{L}}' = \left|\mathbf{n}'\right| \vec{\mathbf{M}}'$, and $\vec{\mathbf{N}}' = \left|\mathbf{n}'\right| \vec{\mathbf{J}}'$. Without further simplifications, no analytical expression exists for the far-field vector potentials, $\mathbf{L}(\mathbf{r})$ and $\mathbf{N}(\mathbf{r})$, given in Eqs. (122) and (123). This is because the integrands in Eqs. (122) and (123) are complicated functions of surface height and surface slopes; namely, h', $h_{x'}$, and $h_{y'}$ with respect to the integrals over the parameterized rough surface. One

9. See Appendix B for more details.

typically simplifies these integrals using the stationary-phase (SP) approximation [22, 35], i.e.,

$$\frac{\partial}{\partial x'}(\mathbf{q}\cdot\mathbf{r}')\approx 0 \quad \frac{\partial}{\partial y'}(\mathbf{q}\cdot\mathbf{r}')\approx 0\,. \tag{124}$$

As a result, the relationships found in Eq. (120) simplify, such that

$$h_{x'}\approx -\frac{q_x}{q_z} \quad h_{y'}\approx -\frac{q_y}{q_z}\,, \tag{125}$$

and in turn, $\vec{\vec{\mathbf{L}}}'\approx\vec{\vec{\mathbf{L}}}$ and $\vec{\vec{\mathbf{N}}}'\approx\vec{\vec{\mathbf{N}}}$ in Eqs. (122) and (123). Similar to the PO approximation, the SP approximation physically dictates that reflection from the rough surface is locally specular and excludes all local diffraction effects [22, 35].

4.3 Scattered field cross-spectral density matrix

The analysis presented here develops closed-form expressions for the scattered field CSDM $\vec{\vec{\mathbf{W}}}^s(\mathbf{r}_1,\mathbf{r}_2)$. In general, $\vec{\vec{\mathbf{W}}}^s(\mathbf{r}_1,\mathbf{r}_2)$ depends on the scattered field $\mathbf{E}^s(\mathbf{r})$, such that in the far field

$$\begin{aligned}\vec{\vec{\mathbf{W}}}^s(\mathbf{r}_1,\mathbf{r}_2)&\equiv\left\langle\mathbf{E}^s(\mathbf{r}_1)\mathbf{E}^{s\dagger}(\mathbf{r}_2)\right\rangle\\&=\begin{bmatrix}\left\langle E_\theta^s(\mathbf{r}_1)E_\theta^{s*}(\mathbf{r}_2)\right\rangle & \left\langle E_\theta^s(\mathbf{r}_1)E_\phi^{s*}(\mathbf{r}_2)\right\rangle\\ \left\langle E_\phi^s(\mathbf{r}_1)E_\theta^{s*}(\mathbf{r}_2)\right\rangle & \left\langle E_\phi^s(\mathbf{r}_1)E_\phi^{s*}(\mathbf{r}_2)\right\rangle\end{bmatrix}.\\&=W_{\mathrm{pq}}^s(\mathbf{r}_1,\mathbf{r}_2)\quad(\mathrm{p}=\theta,\phi;\ \mathrm{q}=\theta,\phi)\end{aligned} \tag{126}$$

Using Eq. (112), one determines the matrix elements found in Eq. (126) as

$$\begin{aligned}W_{\theta\theta}^s(\mathbf{r}_1,\mathbf{r}_2)=\Omega_{12}\sum_{\mathrm{i}=x,y,z}\sum_{\mathrm{j}=x,y,z}\Big[&\left(\hat{\boldsymbol{\phi}}_1\cdot\hat{\mathbf{i}}\right)\left(\hat{\boldsymbol{\phi}}_2\cdot\hat{\mathbf{j}}\right)\left\langle L_{\mathrm{i}}(\mathbf{r}_1)L_{\mathrm{j}}^*(\mathbf{r}_2)\right\rangle\\&+\eta_0\left(\hat{\boldsymbol{\phi}}_1\cdot\hat{\mathbf{i}}\right)\left(\hat{\boldsymbol{\theta}}_2\cdot\hat{\mathbf{j}}\right)\left\langle L_{\mathrm{i}}(\mathbf{r}_1)N_{\mathrm{j}}^*(\mathbf{r}_2)\right\rangle\\&+\eta_0\left(\hat{\boldsymbol{\theta}}_1\cdot\hat{\mathbf{i}}\right)\left(\hat{\boldsymbol{\phi}}_2\cdot\hat{\mathbf{j}}\right)\left\langle N_{\mathrm{i}}(\mathbf{r}_1)L_{\mathrm{j}}^*(\mathbf{r}_2)\right\rangle\\&+\eta_0^2\left(\hat{\boldsymbol{\theta}}_1\cdot\hat{\mathbf{i}}\right)\left(\hat{\boldsymbol{\theta}}_2\cdot\hat{\mathbf{j}}\right)\left\langle N_{\mathrm{i}}(\mathbf{r}_1)N_{\mathrm{j}}^*(\mathbf{r}_2)\right\rangle\Big]\end{aligned}, \tag{127}$$

$$W_{\theta\phi}^{s}(\mathbf{r}_1,\mathbf{r}_2)=\Omega_{12}\sum_{\mathrm{i}=x,y,z}\sum_{\mathrm{j}=x,y,z}\Big[-\left(\hat{\boldsymbol{\phi}}_1\cdot\hat{\mathbf{i}}\right)\left(\hat{\boldsymbol{\theta}}_2\cdot\hat{\mathbf{j}}\right)\left\langle L_{\mathrm{i}}(\mathbf{r}_1)L_{\mathrm{j}}^{*}(\mathbf{r}_2)\right\rangle$$
$$+\eta_0\left(\hat{\boldsymbol{\phi}}_1\cdot\hat{\mathbf{i}}\right)\left(\hat{\boldsymbol{\phi}}_2\cdot\hat{\mathbf{j}}\right)\left\langle L_{\mathrm{i}}(\mathbf{r}_1)N_{\mathrm{j}}^{*}(\mathbf{r}_2)\right\rangle$$
$$-\eta_0\left(\hat{\boldsymbol{\theta}}_1\cdot\hat{\mathbf{i}}\right)\left(\hat{\boldsymbol{\theta}}_2\cdot\hat{\mathbf{j}}\right)\left\langle N_{\mathrm{i}}(\mathbf{r}_1)L_{\mathrm{j}}^{*}(\mathbf{r}_2)\right\rangle$$
$$+\eta_0^2\left(\hat{\boldsymbol{\theta}}_1\cdot\hat{\mathbf{i}}\right)\left(\hat{\boldsymbol{\phi}}_2\cdot\hat{\mathbf{j}}\right)\left\langle N_{\mathrm{i}}(\mathbf{r}_1)N_{\mathrm{j}}^{*}(\mathbf{r}_2)\right\rangle\Big], \quad (128)$$

$$W_{\phi\theta}^{s}(\mathbf{r}_1,\mathbf{r}_2)=\Omega_{12}\sum_{\mathrm{i}=x,y,z}\sum_{\mathrm{j}=x,y,z}\Big[-\left(\hat{\boldsymbol{\theta}}_1\cdot\hat{\mathbf{i}}\right)\left(\hat{\boldsymbol{\phi}}_2\cdot\hat{\mathbf{j}}\right)\left\langle L_{\mathrm{i}}(\mathbf{r}_1)L_{\mathrm{j}}^{*}(\mathbf{r}_2)\right\rangle$$
$$-\eta_0\left(\hat{\boldsymbol{\theta}}_1\cdot\hat{\mathbf{i}}\right)\left(\hat{\boldsymbol{\theta}}_2\cdot\hat{\mathbf{j}}\right)\left\langle L_{\mathrm{i}}(\mathbf{r}_1)N_{\mathrm{j}}^{*}(\mathbf{r}_2)\right\rangle$$
$$+\eta_0\left(\hat{\boldsymbol{\phi}}_1\cdot\hat{\mathbf{i}}\right)\left(\hat{\boldsymbol{\phi}}_2\cdot\hat{\mathbf{j}}\right)\left\langle N_{\mathrm{i}}(\mathbf{r}_1)L_{\mathrm{j}}^{*}(\mathbf{r}_2)\right\rangle$$
$$+\eta_0^2\left(\hat{\boldsymbol{\phi}}_1\cdot\hat{\mathbf{i}}\right)\left(\hat{\boldsymbol{\theta}}_2\cdot\hat{\mathbf{j}}\right)\left\langle N_{\mathrm{i}}(\mathbf{r}_1)N_{\mathrm{j}}^{*}(\mathbf{r}_2)\right\rangle\Big], \quad (129)$$

$$W_{\phi\phi}^{s}(\mathbf{r}_1,\mathbf{r}_2)=\Omega_{12}\sum_{\mathrm{i}=x,y,z}\sum_{\mathrm{j}=x,y,z}\Big[\left(\hat{\boldsymbol{\theta}}_1\cdot\hat{\mathbf{i}}\right)\left(\hat{\boldsymbol{\theta}}_2\cdot\hat{\mathbf{j}}\right)\left\langle L_{\mathrm{i}}(\mathbf{r}_1)L_{\mathrm{j}}^{*}(\mathbf{r}_2)\right\rangle$$
$$-\eta_0\left(\hat{\boldsymbol{\theta}}_1\cdot\hat{\mathbf{i}}\right)\left(\hat{\boldsymbol{\phi}}_2\cdot\hat{\mathbf{j}}\right)\left\langle L_{\mathrm{i}}(\mathbf{r}_1)N_{\mathrm{j}}^{*}(\mathbf{r}_2)\right\rangle$$
$$-\eta_0\left(\hat{\boldsymbol{\phi}}_1\cdot\hat{\mathbf{i}}\right)\left(\hat{\boldsymbol{\theta}}_2\cdot\hat{\mathbf{j}}\right)\left\langle N_{\mathrm{i}}(\mathbf{r}_1)L_{\mathrm{j}}^{*}(\mathbf{r}_2)\right\rangle$$
$$+\eta_0^2\left(\hat{\boldsymbol{\phi}}_1\cdot\hat{\mathbf{i}}\right)\left(\hat{\boldsymbol{\phi}}_2\cdot\hat{\mathbf{j}}\right)\left\langle N_{\mathrm{i}}(\mathbf{r}_1)N_{\mathrm{j}}^{*}(\mathbf{r}_2)\right\rangle\Big], \quad (130)$$

and

where

$$\Omega_{12}=k_0^2\frac{\mathrm{e}^{-jk_0r_1}\,\mathrm{e}^{jk_0r_2}}{(4\pi)^2 r_1 r_2}. \quad (131)$$

In addition, using Eqs. (113)-(125)[10], one determines the element-based correlations found in Eq. (130) from the following relationships:

10. In using Eqs. (113)-(125), one must assume that all observation points are in the far field (cf. Footnote 8, p. 51), the physical-optics approximation holds (cf. Appendix B), and the effects of shadowing/masking and multiple scattering are negligible [38, 42].

$$\left\langle \mathbf{L}\left(\mathbf{r}_1\right)\mathbf{L}^{\dagger}\left(\mathbf{r}_2\right)\right\rangle = \frac{1}{\left(2\pi\right)^4} \int_{-L}^{L}\int_{-L}^{L}\int_{-L}^{L}\int_{-L}^{L}\int_{-\infty}^{\infty}\int_{-\infty}^{\infty}\int_{-\infty}^{\infty}\int_{-\infty}^{\infty} \vec{\vec{\mathbf{L}}}_1 \cdot \left\langle \mathbf{T}^i\left(k_{x1}^i, k_{u1}^i\right)\mathbf{T}^{i\dagger}\left(k_{x2}^i, k_{u2}^i\right)\right\rangle \cdot \vec{\vec{\mathbf{L}}}_2^{\dagger} \; e^{-jk_{v1}^i r_s}\, e^{jk_{v2}^i r_s}\, e^{jq_{x1}x_1'}\, e^{-jq_{x2}x_2'}\, e^{jq_{y1}y_1'}\, e^{-jq_{y2}y_2'} \left\langle e^{jq_{z1}h_1'}\, e^{-jq_{z2}h_2'}\right\rangle dk_{x1}^i dk_{x2}^i dk_{u1}^i dk_{u2}^i dx_1' dx_2' dy_1' dy_2' \quad , \tag{132}$$

$$\left\langle \mathbf{L}\left(\mathbf{r}_1\right)\mathbf{N}^{\dagger}\left(\mathbf{r}_2\right)\right\rangle = -\frac{1}{\left(2\pi\right)^4 \eta_0} \int_{-L}^{L}\int_{-L}^{L}\int_{-L}^{L}\int_{-L}^{L}\int_{-\infty}^{\infty}\int_{-\infty}^{\infty}\int_{-\infty}^{\infty}\int_{-\infty}^{\infty} \vec{\vec{\mathbf{L}}}_1 \cdot \left\langle \mathbf{T}^i\left(k_{x1}^i, k_{u1}^i\right)\mathbf{T}^{i\dagger}\left(k_{x2}^i, k_{u2}^i\right)\right\rangle \cdot \vec{\vec{\mathbf{N}}}_2^{\dagger} \; e^{-jk_{v1}^i r_s}\, e^{jk_{v2}^i r_s}\, e^{jq_{x1}x_1'}\, e^{-jq_{x2}x_2'}\, e^{jq_{y1}y_1'}\, e^{-jq_{y2}y_2'} \left\langle e^{jq_{z1}h_1'}\, e^{-jq_{z2}h_2'}\right\rangle dk_{x1}^i dk_{x2}^i dk_{u1}^i dk_{u2}^i dx_1' dx_2' dy_1' dy_2' \quad , \tag{133}$$

$$\left\langle \mathbf{N}\left(\mathbf{r}_1\right)\mathbf{L}^{\dagger}\left(\mathbf{r}_2\right)\right\rangle = -\frac{1}{\left(2\pi\right)^4 \eta_0} \int_{-L}^{L}\int_{-L}^{L}\int_{-L}^{L}\int_{-L}^{L}\int_{-\infty}^{\infty}\int_{-\infty}^{\infty}\int_{-\infty}^{\infty}\int_{-\infty}^{\infty} \vec{\vec{\mathbf{N}}}_1 \cdot \left\langle \mathbf{T}^i\left(k_{x1}^i, k_{u1}^i\right)\mathbf{T}^{i\dagger}\left(k_{x2}^i, k_{u2}^i\right)\right\rangle \cdot \vec{\vec{\mathbf{L}}}_2^{\dagger} \; e^{-jk_{v1}^i r_s}\, e^{jk_{v2}^i r_s}\, e^{jq_{x1}x_1'}\, e^{-jq_{x2}x_2'}\, e^{jq_{y1}y_1'}\, e^{-jq_{y2}y_2'} \left\langle e^{jq_{z1}h_1'}\, e^{-jq_{z2}h_2'}\right\rangle dk_{x1}^i dk_{x2}^i dk_{u1}^i dk_{u2}^i dx_1' dx_2' dy_1' dy_2' \quad , \tag{134}$$

and

$$\left\langle \mathbf{N}\left(\mathbf{r}_1\right)\mathbf{N}^{\dagger}\left(\mathbf{r}_2\right)\right\rangle = \frac{1}{\left(2\pi\right)^4 \eta_0^2} \int_{-L}^{L}\int_{-L}^{L}\int_{-L}^{L}\int_{-L}^{L}\int_{-\infty}^{\infty}\int_{-\infty}^{\infty}\int_{-\infty}^{\infty}\int_{-\infty}^{\infty} \vec{\vec{\mathbf{N}}}_1 \cdot \left\langle \mathbf{T}^i\left(k_{x1}^i, k_{u1}^i\right)\mathbf{T}^{i\dagger}\left(k_{x2}^i, k_{u2}^i\right)\right\rangle \cdot \vec{\vec{\mathbf{N}}}_2^{\dagger} \; e^{-jk_{v1}^i r_s}\, e^{jk_{v2}^i r_s}\, e^{jq_{x1}x_1'}\, e^{-jq_{x2}x_2'}\, e^{jq_{y1}y_1'}\, e^{-jq_{y2}y_2'} \left\langle e^{jq_{z1}h_1'}\, e^{-jq_{z2}h_2'}\right\rangle dk_{x1}^i dk_{x2}^i dk_{u1}^i dk_{u2}^i dx_1' dx_2' dy_1' dy_2' \quad , \tag{135}$$

where $r_s = \left|\mathbf{r}_s\right|$. Inherent in Eqs. (132)-(135) is the assumption that the incident field plane-wave spectrum is statistically independent of the rough surface. This assumption is physically intuitive; thus, Eqs. (132)-(135) contain two separate correlations.

The first correlation is with respect to the incident field plane-wave spectrum. This correlation is equivalent to a dyadic [cf. Eq. (111)]; namely,

$$\left\langle \mathbf{T}^{i}\left(k_{x1}^{i},k_{u1}^{i}\right)\mathbf{T}^{i\dagger}\left(k_{x2}^{i},k_{u2}^{i}\right)\right\rangle =\ddot{\mathbf{\Phi}}^{i}, \tag{136}$$

where $\ddot{\mathbf{\Phi}}^{i}=\ddot{\mathbf{\Phi}}^{i}\left(k_{x1}^{i},k_{x2}^{i},k_{u1}^{i},k_{u2}^{i}\right)$. The second correlation is with respect to the parameterized rough surface. This correlation is a joint characteristic function χ' of the random variables $h_1'=h\left(x_1',y_1'\right)$ and $h_2'=h\left(x_2',y_2'\right)$, such that

$$\left\langle \mathrm{e}^{jq_{z1}h_1'}\,\mathrm{e}^{-jq_{z2}h_2'}\right\rangle =\chi'. \tag{137}$$

In practice, one must choose a form for this joint characteristic function.

A very common choice for the statistical distribution of the rough surface is to assume that the surface heights are Gaussian distributed and Gaussian correlated. In so doing, the joint probability density function $p'=p\left(h_1',h_2'\right)$ of the random variables h_1' and h_2' takes the following form [36]:

$$p'=\frac{1}{2\pi\sigma_h^2\sqrt{1-\Gamma'^2}}\exp\left[-\frac{h_1'^2+h_2'^2-2\Gamma'h_1'h_2'}{2\sigma_h^2\left(1-\Gamma'^2\right)}\right], \tag{138}$$

where $\Gamma'=\Gamma\left(x_1'-x_2',y_1'-y_2'\right)$ is the surface autocorrelation function, such that

$$\Gamma'=\exp\left[-\frac{\left(x_1'-x_2'\right)^2}{\ell_h^2}\right]\exp\left[-\frac{\left(y_1'-y_2'\right)^2}{\ell_h^2}\right]. \tag{139}$$

History shows that one typically chooses Gaussian-Gaussian (G-G) models for analytical convenience [93]; however, other models exist in practice. For example, the stretched exponential-stretched exponential (SE-SE) model better characterizes surfaces roughened by random industrial processes [138]. Basu *et al.* highlighted this point with profilometer

measurements of sandblasted metallic surfaces [139, 140]. Unfortunately no general analytical form exists for the SE joint characteristic function; nevertheless, the analysis of Basu *et al*. also showed that G-G models were still fairly good approximations for sandblasted metallic surfaces [139, 140]. Thus, Fourier transforming the joint probability density function p' in Eq. (138) yields the desired joint characteristic function for the present analysis [36], i.e.,

$$\begin{aligned}\chi' &= \int_{-\infty}^{\infty}\int_{-\infty}^{\infty} p' \, \mathrm{e}^{jq_{z1}h_1'} \, \mathrm{e}^{-jq_{z2}h_2'} \, dh_1' dh_2' \\ &= \exp\left[-\frac{\sigma_h^2}{2}\left(q_{z1}^2 + q_{z2}^2\right)\right] \exp\left(\sigma_h^2 q_{z1} q_{z2} \Gamma'\right)\end{aligned}, \tag{140}$$

where $\chi' = \chi\left(k_{x1}^i, k_{x2}^i, k_{u1}^i, k_{u2}^i; x_1' - x_2', y_1' - y_2'\right)$. Note that throughout the literature, numerous other surface models exist in addition to G-G and SE models[11].

Using the relationships found in Eqs. (136)-(140), the integrands in Eqs. (132)-(135) still contain complicated functions with respect to the source and surface parameters. To simplify the analysis, one can separate these complicated functions into amplitude and phase terms, viz.,

$$\begin{aligned}\left\langle \mathbf{L}(\mathbf{r}_1)\mathbf{L}^{\dagger}(\mathbf{r}_2)\right\rangle = &\frac{1}{(2\pi)^4} \\ &\int_{-L}^{L}\int_{-L}^{L}\int_{-L}^{L}\int_{-L}^{L}\left(\int_{-\infty}^{\infty}\int_{-\infty}^{\infty}\int_{-\infty}^{\infty}\int_{-\infty}^{\infty} \vec{\mathbf{f}}^{\mathcal{L}} \, \mathrm{e}^{jk_0 g} \, dk_{x1}^i dk_{x2}^i dk_{u1}^i dk_{u2}^i\right) dx_1' dx_2' dy_1' dy_2'\end{aligned}, \tag{141}$$

11. For example, a recent publication explored the use of non-Gaussian surface autocorrelation functions [141].

$$\left\langle \mathbf{L}\left(\mathbf{r}_1\right)\mathbf{N}^{\dagger}\left(\mathbf{r}_2\right)\right\rangle = -\frac{1}{\left(2\pi\right)^4\eta_0} \int_{-L}^{L}\int_{-L}^{L}\int_{-L}^{L}\int_{-L}^{L}\left(\int_{-\infty}^{\infty}\int_{-\infty}^{\infty}\int_{-\infty}^{\infty}\int_{-\infty}^{\infty}\vec{\mathbf{f}}^{\mathcal{K}}\,\mathrm{e}^{jk_0 g}\,dk_{x1}^{i}dk_{x2}^{i}dk_{u1}^{i}dk_{u2}^{i}\right)dx_1'dx_2'dy_1'dy_2' \quad (142)$$

$$\left\langle \mathbf{N}\left(\mathbf{r}_1\right)\mathbf{L}^{\dagger}\left(\mathbf{r}_2\right)\right\rangle = -\frac{1}{\left(2\pi\right)^4\eta_0} \int_{-L}^{L}\int_{-L}^{L}\int_{-L}^{L}\int_{-L}^{L}\left(\int_{-\infty}^{\infty}\int_{-\infty}^{\infty}\int_{-\infty}^{\infty}\int_{-\infty}^{\infty}\vec{\mathbf{f}}^{\mathcal{M}}\,\mathrm{e}^{jk_0 g}\,dk_{x1}^{i}dk_{x2}^{i}dk_{u1}^{i}dk_{u2}^{i}\right)dx_1'dx_2'dy_1'dy_2' \quad (143)$$

and

$$\left\langle \mathbf{N}\left(\mathbf{r}_1\right)\mathbf{N}^{\dagger}\left(\mathbf{r}_2\right)\right\rangle = \frac{1}{\left(2\pi\right)^4\eta_0^2} \int_{-L}^{L}\int_{-L}^{L}\int_{-L}^{L}\int_{-L}^{L}\left(\int_{-\infty}^{\infty}\int_{-\infty}^{\infty}\int_{-\infty}^{\infty}\int_{-\infty}^{\infty}\vec{\mathbf{f}}^{\mathcal{N}}\,\mathrm{e}^{jk_0 g}\,dk_{x1}^{i}dk_{x2}^{i}dk_{u1}^{i}dk_{u2}^{i}\right)dx_1'dx_2'dy_1'dy_2' \quad (144)$$

Here,

$$\vec{\mathbf{f}}^{\mathcal{L}} = \chi'\left(\vec{\mathbf{L}}_1\cdot\vec{\boldsymbol{\Phi}}^{i}\cdot\vec{\mathbf{L}}_2^{\dagger}\right), \quad (145)$$

$$\vec{\mathbf{f}}^{\mathcal{K}} = \chi'\left(\vec{\mathbf{L}}_1\cdot\vec{\boldsymbol{\Phi}}^{i}\cdot\vec{\mathbf{N}}_2^{\dagger}\right), \quad (146)$$

$$\vec{\mathbf{f}}^{\mathcal{M}} = \chi'\left(\vec{\mathbf{N}}_1\cdot\vec{\boldsymbol{\Phi}}^{i}\cdot\vec{\mathbf{L}}_2^{\dagger}\right), \quad (147)$$

and

$$\vec{\mathbf{f}}^{\mathcal{N}} = \chi'\left(\vec{\mathbf{N}}_1\cdot\vec{\boldsymbol{\Phi}}^{i}\cdot\vec{\mathbf{N}}_2^{\dagger}\right) \quad (148)$$

are amplitude dyadics that contains all of the amplitude terms, and

$$\begin{aligned} g = &\left[r_s + \left(\hat{\mathbf{y}}\cdot\hat{\mathbf{v}}\right)y_2'\right]k_{v2}^{i} - \left[r_s + \left(\hat{\mathbf{y}}\cdot\hat{\mathbf{v}}\right)y_1'\right]k_{v1}^{i} \\ &+ \frac{1}{k_0}\left(x_2'k_{x2}^{i} - x_1'k_{x1}^{i}\right) + \frac{\left(\hat{\mathbf{y}}\cdot\hat{\mathbf{u}}\right)}{k_0}\left(y_2'k_{u2}^{i} - y_1'k_{u1}^{i}\right) \\ &+ \left(\hat{\mathbf{x}}\cdot\hat{\mathbf{r}}_1x_1' - \hat{\mathbf{x}}\cdot\hat{\mathbf{r}}_2x_2'\right) + \left(\hat{\mathbf{y}}\cdot\hat{\mathbf{r}}_1y_1' - \hat{\mathbf{y}}\cdot\hat{\mathbf{r}}_2y_2'\right) \end{aligned} \quad (149)$$

is a common phase function that contains all of the phase terms. Without further simplifications, no closed-form expressions exist for the integral relationships given in Eqs. (141)-(144).

To simplify the integrals found in parenthesis in Eqs. (141)-(144), the analysis uses an asymptotic mathematical technique known as the method of stationary phase (MoSP) [26, 27, 37]. In so doing, one assumes that the amplitude terms are slowly varying in the interval $(-\infty,\infty)$. One must also assume that the phase terms are rapidly oscillating in the interval $(-\infty,\infty)$ except near special points where the rate of change is zero or "stationary." These special points are called critical points of the first kind [26]. Away from these points, the phase terms are rapidly oscillating and the positive and negative contributions of the integrand in Eq. (144) effectively cancel out.

Using the MoSP to simplify Eqs. (141)-(144) has two implications with regards to the macro-scale scattering geometry given in Figure 9a. The first implication is with respect to the v component of the incident propagation vector $\mathbf{k}^i$; namely,

$$k_v^i = \sqrt{k_0^2 - \left(k_x^i\right)^2 - \left(k_u^i\right)^2}\,. \tag{150}$$

In particular, the analysis assumes that $k_v^i \gg k_x^i$ and $k_v^i \gg k_u^i$; as a result,

$$k_{v1,2}^i \approx \begin{cases} k_0 & \text{in } \ddot{\mathbf{f}}_0^{\mathcal{L}},\ \ddot{\mathbf{f}}_0^{\mathcal{K}},\ \ddot{\mathbf{f}}_0^{\mathcal{K}}, \text{ and } \ddot{\mathbf{f}}_0^{\mathcal{N}} \\ k_0 - \dfrac{\left(k_{x1,2}^i\right)^2}{2k_0} - \dfrac{\left(k_{u1,2}^i\right)^2}{2k_0} & \text{in } g \end{cases}. \tag{151}$$

This physically implies that the incident electromagnetic fields are highly directional being predominately directed along the v direction in Figure 9a. The second implication is that the distance from the source-plane origin to the surface-plane origin must be much, much greater than half the surface length, i.e., $r_s \gg L$, which is typically the case for most directed-energy and remote-sensing engagement scenarios. To provide some idea

of how much greater, letting $r_s = 5L$, $r_s = 25L$, and $r_s = 100L$ results in percentage errors of 18%, 4%, and 1%, respectively. As such, using the MoSP to simplify Eqs. (141)-(144) results in the following relationships:

$$\left\langle \mathbf{L}(\mathbf{r}_1)\mathbf{L}^{\dagger}(\mathbf{r}_2)\right\rangle \approx \frac{k_0^2}{(2\pi)^2 r_s^2}\vec{\vec{\mathcal{L}}}, \tag{152}$$

$$\left\langle \mathbf{L}(\mathbf{r}_1)\mathbf{N}^{\dagger}(\mathbf{r}_2)\right\rangle \approx -\frac{k_0^2}{(2\pi)^2 \eta_0 r_s^2}\vec{\vec{\mathcal{K}}}, \tag{153}$$

$$\left\langle \mathbf{N}(\mathbf{r}_1)\mathbf{L}^{\dagger}(\mathbf{r}_2)\right\rangle \approx -\frac{k_0^2}{(2\pi)^2 \eta_0 r_s^2}\vec{\vec{\mathcal{M}}}, \tag{154}$$

and

$$\left\langle \mathbf{N}(\mathbf{r}_1)\mathbf{N}^{\dagger}(\mathbf{r}_2)\right\rangle \approx \frac{k_0^2}{(2\pi)^2 \eta_0^2 r_s^2}\vec{\vec{\mathcal{N}}}, \tag{155}$$

where $\vec{\vec{\mathcal{L}}}$, $\vec{\vec{\mathcal{K}}}$, $\vec{\vec{\mathcal{M}}}$, and $\vec{\vec{\mathcal{N}}}$ are dyadics that contain all of the amplitude and phase terms evaluated at the critical points of the first kind which one determines as[12]

$$k_{x1,2}^{i} \approx \frac{k_0}{r_s}x_{1,2}' \quad k_{u1,2}^{i} \approx \frac{k_0(\hat{\mathbf{y}}\cdot\hat{\mathbf{u}})}{r_s}y_{1,2}'. \tag{156}$$

The analysis explicitly defines $\vec{\vec{\mathcal{L}}}$, $\vec{\vec{\mathcal{K}}}$, $\vec{\vec{\mathcal{M}}}$, and $\vec{\vec{\mathcal{N}}}$ in Appendix D for different material substrates, i.e., dielectrics, conductors, and a perfect electrical conductor (PEC).

Provided Eqs. (152)-(156) and Appendix D, one is still left with integrals with respect to the parameterized rough surface. These integrals take the following element-based form:

12. See Appendix C for more details.

$$
\begin{aligned}
\Psi_{\mathrm{mn}} = & \int_{-L}^{L}\int_{-L}^{L}\int_{-L}^{L}\int_{-L}^{L} \Phi^{i}_{\mathrm{mn}}\left(\frac{k_0}{r_s}x_1', \frac{k_0}{r_s}x_2', \frac{k_0\left(\hat{\mathbf{y}}\cdot\hat{\mathbf{u}}\right)}{r_s}y_1', \frac{k_0\left(\hat{\mathbf{y}}\cdot\hat{\mathbf{u}}\right)}{r_s}y_2'\right) \\
& \chi'\left(\frac{k_0}{r_s}x_1', \frac{k_0}{r_s}x_2', \frac{k_0\left(\hat{\mathbf{y}}\cdot\hat{\mathbf{u}}\right)}{r_s}y_1', \frac{k_0\left(\hat{\mathbf{y}}\cdot\hat{\mathbf{u}}\right)}{r_s}y_2'; x_1'-x_2', y_1'-y_2'\right) \\
& \exp\left[jk_0\left(\hat{\mathbf{x}}\cdot\hat{\mathbf{r}}_1x_1' - \hat{\mathbf{x}}\cdot\hat{\mathbf{r}}_2x_2'\right)\right]\exp\left[jk_0\left(\hat{\mathbf{y}}\cdot\hat{\mathbf{r}}_1y_1' - \hat{\mathbf{y}}\cdot\hat{\mathbf{r}}_2y_2'\right)\right] \quad , \qquad (157) \\
& \exp\left[-j\frac{k_0}{2r_s}\left(x_1'^2 - x_2'^2\right)\right]\exp\left[-j\frac{k_0\left(\hat{\mathbf{y}}\cdot\hat{\mathbf{u}}\right)^2}{2r_s}\left(y_1'^2 - y_2'^2\right)\right] \\
& \exp\left[-jk_0\left(\hat{\mathbf{y}}\cdot\hat{\mathbf{v}}\right)\left(y_1' - y_2'\right)\right]dx_1'dx_2'dy_1'dy_2'
\end{aligned}
$$

where $\left(\mathrm{m} = x,u;\ \mathrm{n} = x,u\right)$. In Eq. (157), Φ^{i}_{mn} is equivalent to the Fourier transform of the incident field CSDM elements found in Eq. (108), i.e.,

$$
\begin{aligned}
\Phi^{i}_{\mathrm{mn}} &= \int_{-\infty}^{\infty}\int_{-\infty}^{\infty}\int_{-\infty}^{\infty}\int_{-\infty}^{\infty} W^{i}_{\mathrm{mn}}\left(\boldsymbol{\rho}_1,\boldsymbol{\rho}_2\right)\mathrm{e}^{jk^{i}_{x1}x_1}\,\mathrm{e}^{-jk^{i}_{x2}x_2}\,\mathrm{e}^{jk^{i}_{u1}u_1}\,\mathrm{e}^{-jk^{i}_{u2}u_2}\,dx_1dx_2du_1du_2 \\
&= \frac{\pi^2 A_{\mathrm{m}}A_{\mathrm{n}}B_{\mathrm{mn}}}{\left(a^2_{\mathrm{mn}} - b^2_{\mathrm{mn}}\right)}\exp\left[-\tilde{a}_{\mathrm{mn}}\left(k^{i}_{x1}\right)^2 - \tilde{a}_{\mathrm{mn}}\left(k^{i}_{x2}\right)^2 + 2\tilde{b}_{\mathrm{mn}}k^{i}_{x1}k^{i}_{x2}\right] \quad , \qquad (158) \\
&\qquad \exp\left[-\tilde{a}_{\mathrm{mn}}\left(k^{i}_{u1}\right)^2 - \tilde{a}_{\mathrm{mn}}\left(k^{i}_{u2}\right)^2 + 2\tilde{b}_{\mathrm{mn}}k^{i}_{u1}k^{i}_{u2}\right]
\end{aligned}
$$

where $\left(\mathrm{m} = x,u;\ \mathrm{n} = x,u\right)$ and

$$
a_{\mathrm{mn}} = \frac{1}{4w_s^2} + b_{\mathrm{mn}} \quad b_{\mathrm{mn}} = \frac{1}{2\ell^2_{\mathrm{mn}}} \quad \tilde{a}_{\mathrm{mn}} = \frac{a_{\mathrm{mn}}}{4\left(a^2_{\mathrm{mn}} - b^2_{\mathrm{mn}}\right)} \quad \tilde{b}_{mn} = \frac{b_{\mathrm{mn}}}{4\left(a^2_{\mathrm{mn}} - b^2_{\mathrm{mn}}\right)}. \qquad (159)
$$

One can reduce the integrals found in Eq. (157) into closed-form expressions. For this purpose, the analysis first performs the following variable transformations:

$$
x_d = x_1' - x_2' \quad x_a = x_1' + x_2' \quad y_d = y_1' - y_2' \quad y_a = y_1' + y_2', \qquad (160)
$$

so that Eq. (157) simplifies into the following expression:

$$\Psi_{mn} = \frac{\pi^2 A_{\mathrm{m}} A_{\mathrm{n}} B_{\mathrm{mn}}}{4\left(a_{\mathrm{mn}}^2 - b_{\mathrm{mn}}^2\right)} \exp\left[-\frac{k_0^2\sigma_h^2}{2}\left(\vartheta_{z1}^2 + \vartheta_{z2}^2\right)\right]$$
$$\int_{-2L}^{2L}\int_{|y_a|-2L}^{2L-|y_a|}\int_{-2L}^{2L}\int_{|x_a|-2L}^{2L-|x_a|} \exp\left[k_0^2\sigma_h^2\vartheta_{z1}\vartheta_{z2}\exp\left(-\frac{x_d^2}{\ell_h^2}\right)\exp\left(-\frac{y_d^2}{\ell_h^2}\right)\right]$$
$$\exp\left[-\frac{k_0^2}{2r_s^2}\left(\tilde{a}_{\mathrm{mn}} + \tilde{b}_{\mathrm{mn}}\right)x_d^2\right]\exp\left[-\frac{k_0^2}{2r_s^2}\left(\tilde{a}_{\mathrm{mn}} - \tilde{b}_{\mathrm{mn}}\right)x_a^2\right]$$
$$\exp\left[-\frac{k_0^2\left(\hat{\mathbf{y}}\cdot\hat{\mathbf{u}}\right)^2}{2r_s^2}\left(\tilde{a}_{\mathrm{mn}} + \tilde{b}_{\mathrm{mn}}\right)y_d^2\right]\exp\left[-\frac{k_0^2\left(\hat{\mathbf{y}}\cdot\hat{\mathbf{u}}\right)^2}{2r_s^2}\left(\tilde{a}_{\mathrm{mn}} - \tilde{b}_{\mathrm{mn}}\right)y_a^2\right]$$
$$\exp\left[j\frac{k_0}{2}\left(\vartheta_{x1} + \vartheta_{x2}\right)x_d\right]\exp\left[j\frac{k_0}{2}\left(\vartheta_{x1} - \vartheta_{x2}\right)x_a\right]$$
$$\exp\left[j\frac{k_0}{2}\left(\vartheta_{y1} + \vartheta_{y2}\right)y_d\right]\exp\left[j\frac{k_0}{2}\left(\vartheta_{y1} - \vartheta_{y2}\right)y_a\right]$$
$$\exp\left[-j\frac{k_0}{2r_s}x_a x_d\right]\exp\left[-j\frac{k_0\left(\hat{\mathbf{y}}\cdot\hat{\mathbf{u}}\right)^2}{2r_s}y_a y_d\right]dx_d\,dx_a\,dy_d\,dy_a \quad , \qquad (161)$$

where $\left(\mathrm{m} = x,u;\ \mathrm{n} = x,u\right)$ and

$$\vartheta_{x1,2} = \hat{\mathbf{x}}\cdot\hat{\mathbf{r}}_{1,2} \quad \vartheta_{y1,2} = \hat{\mathbf{y}}\cdot\hat{\mathbf{r}}_{1,2} - \hat{\mathbf{y}}\cdot\hat{\mathbf{v}} \quad \vartheta_{z1,2} = \hat{\mathbf{z}}\cdot\hat{\mathbf{r}}_{1,2} - \hat{\mathbf{z}}\cdot\hat{\mathbf{v}}\,. \qquad (162)$$

From here, one must handle the exponential term containing the surface autocorrelation function (i.e., the first exponential term inside the integrals above). History shows that there are two separate ways to go about this. The first is to expand the said exponential term in a Taylor series and proceed with the evaluation of the integrals [36]. Mathematically, this approach is applicable to all surfaces; however, because the series is slowly convergent, the analysis limits this approach to smooth-to-moderately rough surfaces—the next sub-section develops a closed-form expression for this case. The other approach involves expanding the surface autocorrelation function [cf. Eq. (139)] in a Taylor series and retaining only the first and second order terms [36]. This treatment is

applicable to very rough surfaces—sub-section 4.3.2 develops a closed-form expression for this case.

4.3.1 Smooth-to-moderately rough surfaces

When considering smooth-to-moderately rough surfaces, one must expand the exponential term containing the surface autocorrelation function found in Eq. (161) in a Taylor series. Specifically,

$$\exp\left[k_0^2\sigma_h^2\vartheta_{z1}\vartheta_{z2}\exp\left(-\frac{x_d^2}{\ell_h^2}\right)\exp\left(-\frac{y_d^2}{\ell_h^2}\right)\right]=\sum_{l=0}^{\infty}\frac{\left(k_0^2\sigma_h^2\vartheta_{z1}\vartheta_{z2}\right)^l}{l!}\exp\left(-\frac{l}{\ell_h^2}x_d^2\right)\exp\left(-\frac{l}{\ell_h^2}y_d^2\right) \quad . \tag{163}$$

Substitution of Eq. (163) into Eq. (161) allows one to then separate the integrals over the parameterized rough surface, i.e.,

$$\begin{aligned}\Psi_{\mathrm{mn}}=&\frac{\pi^2 A_{\mathrm{m}}A_{\mathrm{n}}B_{\mathrm{mn}}}{4\left(a_{\mathrm{mn}}^2-b_{\mathrm{mn}}^2\right)}\exp\left[-\frac{k_0^2\sigma_h^2}{2}\left(\vartheta_{z1}^2+\vartheta_{z2}^2\right)\right]\sum_{l=0}^{\infty}\frac{\left(k_0^2\sigma_h^2\vartheta_{z1}\vartheta_{z2}\right)^l}{l!}\\&\int_{-2L}^{2L}\exp\left[-\frac{k_0^2}{2r_s^2}\left(\tilde{a}_{\mathrm{mn}}-\tilde{b}_{\mathrm{mn}}\right)x_a^2\right]\exp\left[j\frac{k_0}{2}\left(\vartheta_{x1}-\vartheta_{x2}\right)x_a\right]\\&\int_{|x_a|-2L}^{2L-|x_a|}\exp\left(-\frac{l}{\ell_h^2}x_d^2\right)\exp\left[-\frac{k_0^2}{2r_s^2}\left(\tilde{a}_{\mathrm{mn}}+\tilde{b}_{\mathrm{mn}}\right)x_d^2\right]\\&\exp\left(-j\frac{k_0}{2r_s}\left[x_a-r_s\left(\vartheta_{x1}+\vartheta_{x2}\right)\right]x_d\right)dx_d dx_a\\&\int_{-2L}^{2L}\exp\left[-\frac{k_0^2\left(\hat{\mathbf{y}}\cdot\hat{\mathbf{u}}\right)^2}{2r_s^2}\left(\tilde{a}_{\mathrm{mn}}-\tilde{b}_{\mathrm{mn}}\right)y_a^2\right]\exp\left[j\frac{k_0}{2}\left(\vartheta_{y1}-\vartheta_{y2}\right)y_a\right]\\&\int_{|y_a|-2L}^{2L-|y_a|}\exp\left(-\frac{l}{\ell_h^2}y_d^2\right)\exp\left[-\frac{k_0^2\left(\hat{\mathbf{y}}\cdot\hat{\mathbf{u}}\right)^2}{2r_s^2}\left(\tilde{a}_{\mathrm{mn}}+\tilde{b}_{\mathrm{mn}}\right)y_d^2\right]\\&\exp\left(-j\frac{k_0}{2r_s}\left[\left(\hat{\mathbf{y}}\cdot\hat{\mathbf{u}}\right)^2y_a-r_s\left(\vartheta_{y1}+\vartheta_{y2}\right)\right]y_d\right)dy_d dy_a \quad .\end{aligned} \tag{164}$$

This is a very important step in the analysis. It allows for the development of a closed form expression for smooth-to-moderately rough surface conditions without having to convert to polar coordinates.

It is a relatively straight forward process to evaluate the integrals over x_d and y_d in Eq. (164); however, complex error functions result due to the parameterized rough surface [10, 11]. These complex error functions model diffraction caused by the incident radiation over-illuminating the rough surface and are negligible under certain conditions. As such, the present goal in the analysis is to determine conditions in which one can extend the x_d and y_d limits of integration to $(-\infty,\infty)$ in Eq. (164). The necessary conditions for these approximations occurs when

$$\begin{aligned} \exp\left(-\frac{l}{\ell_h^2}x_d^2\right)\exp\left[-\frac{k_0^2}{2r_s^2}\left(\tilde{a}_{\text{mn}}+\tilde{b}_{\text{mn}}\right)x_d^2\right] &> \delta_x \\ \exp\left(-\frac{l}{\ell_h^2}y_d^2\right)\exp\left[-\frac{k_0^2\left(\hat{\mathbf{y}}\cdot\hat{\mathbf{u}}\right)^2}{2r_s^2}\left(\tilde{a}_{\text{mn}}+\tilde{b}_{\text{mn}}\right)y_d^2\right] &> \delta_y \end{aligned}, \tag{165}$$

where δ_x and δ_y are user-defined parameters and denote the points at which the exponential functions with respect to x_d and y_d no longer maintain significant value in Eq. (164). Furthermore, if $l=0$ and $x_d=y_d=2L$, the arguments of the exponentials are at a minimum and the x_d and y_d limits of integration are at a maximum. One then derives the following conditions from Eq. (165):

$$L>\frac{r_s}{k_0 w_s}\sqrt{\frac{-\ln\left(\delta_x\right)}{2}} \quad L>\frac{r_s}{k_0 w_s\left|\hat{\mathbf{y}}\cdot\hat{\mathbf{u}}\right|}\sqrt{\frac{-\ln\left(\delta_y\right)}{2}}. \tag{166}$$

These conditions physically mean that the projected fully coherent incident beam size must "fit" on the rough surface. In satisfying these conditions the x_d and y_d limits of integration extend to $(-\infty,\infty)$ in Eq. (164). Note that if $\delta_x = \delta_y = \delta$, the second condition in Eq. (166) becomes more stringent since $\left|\hat{\mathbf{y}}\cdot\hat{\mathbf{u}}\right| = \left|-\cos\left(\theta^i\right)\right| \le 1$ [cf. Figure 9a]. One then determines how well the incident beam "fits" by δ—the smaller the δ, the more accurate the approximation. Also note that if the projected fully coherent incident beam size does not "fit" on the rough surface, complex error functions result [10, 11], and one has to evaluate the follow-on integral expression numerically.

Assuming that the conditions in Eq. (166) hold, subsequent evaluation of the integrals over x_d and y_d simplifies Eq. (164), so that[13]

13. One must complete the square in the exponential terms and use of the following integral relationship [125, p. 266]: $\int_{-\infty}^{\infty}\exp\left(-at^2\right)\exp\left(-jbt\right)dt = \sqrt{\pi/a}\exp\left[-b^2/(4a)\right]$, where $a > 0$.

$$
\begin{aligned}
\Psi_{\mathrm{mn}} = {} & \frac{\pi^3 r_s^2 \ell_h^2 A_{\mathrm{m}} A_{\mathrm{n}} B_{\mathrm{mn}}}{2\left(a_{\mathrm{mn}}^2 - b_{\mathrm{mn}}^2\right)} \exp\left[-\frac{k_0^2 \sigma_h^2}{2}\left(\vartheta_{z1}^2 + \vartheta_{z2}^2\right)\right] \sum_{l=0}^{\infty} \frac{\left(k_0^2 \sigma_h^2 \vartheta_{z1} \vartheta_{z2}\right)^l}{l! \sqrt{\mathcal{D}_{l\mathrm{mn}}^x \mathcal{D}_{l\mathrm{mn}}^y}} \\
& \exp\left[-\frac{k_0^2 r_s^2 \ell_h^2}{8\mathcal{D}_{l\mathrm{mn}}^x}\left(\vartheta_{x1} + \vartheta_{x2}\right)^2\right] \exp\left[-\frac{k_0^2 r_s^2 \ell_h^2}{8\mathcal{D}_{l\mathrm{mn}}^y}\left(\vartheta_{y1} + \vartheta_{y2}\right)^2\right] \\
& \int_{-2L}^{2L} \exp\left[-\frac{k_0^2}{2r_s^2}\left(\tilde{a}_{\mathrm{mn}} - \tilde{b}_{\mathrm{mn}}\right) x_a^2\right] \exp\left[-\frac{k_0^2 \ell_h^2}{8\mathcal{D}_{l\mathrm{mn}}^x} x_a^2\right] \\
& \exp\left[\frac{k_0^2 r_s \ell_h^2}{4\mathcal{D}_{l\mathrm{mn}}^x}\left(\vartheta_{x1} + \vartheta_{x2}\right) x_a\right] \exp\left[j\frac{k_0}{2}\left(\vartheta_{x1} - \vartheta_{x2}\right) x_a\right] dx_a \\
& \int_{-2L}^{2L} \exp\left[-\frac{k_0^2 \left(\hat{\mathbf{y}} \cdot \hat{\mathbf{u}}\right)^2}{2r_s^2}\left(\tilde{a}_{\mathrm{mn}} - \tilde{b}_{\mathrm{mn}}\right) y_a^2\right] \left[-\frac{\left(\hat{\mathbf{y}} \cdot \hat{\mathbf{u}}\right)^4 k_0^2 \ell_h^2}{8\mathcal{D}_{l\mathrm{mn}}^y} y_a^2\right] \\
& \exp\left[\frac{k_0^2 r_s \ell_h^2 \left(\hat{\mathbf{y}} \cdot \hat{\mathbf{u}}\right)^2}{4\mathcal{D}_{l\mathrm{mn}}^y}\left(\vartheta_{y1} + \vartheta_{y2}\right) y_a\right] \exp\left[j\frac{k_0}{2}\left(\vartheta_{y1} - \vartheta_{y2}\right) y_a\right] dy_a
\end{aligned}
, \tag{167}
$$

where $\left(\mathrm{m} = x,u;\ \mathrm{n} = x,u\right)$ and

$$
\begin{aligned}
\mathcal{D}_{l\mathrm{mn}}^x &= k_0^2 \ell_h^2 \left(\tilde{a}_{\mathrm{mn}} + \tilde{b}_{\mathrm{mn}}\right) + 2lr_s^2 \\
\mathcal{D}_{l\mathrm{mn}}^y &= k_0^2 \ell_h^2 \left(\tilde{a}_{\mathrm{mn}} + \tilde{b}_{\mathrm{mn}}\right)\left(\hat{\mathbf{y}} \cdot \hat{\mathbf{u}}\right)^2 + 2lr_s^2
\end{aligned}
. \tag{168}
$$

Similar to the analysis presented above, one can extend the x_a and y_a limits of integration to $\left(-\infty,\infty\right)$ in Eq. (164) and subsequently Eq. (167). Here, the necessary conditions for these approximations occurs when

$$
L > \frac{r_s}{k_0 w_s}\sqrt{\frac{-\ln\left(\delta_x\right)}{2}\left(1 + \frac{4}{\alpha_{\mathrm{mn}}^2}\right)} \quad L > \frac{r_s}{k_0 w_s \left|\hat{\mathbf{y}} \cdot \hat{\mathbf{u}}\right|}\sqrt{\frac{-\ln\left(\delta_y\right)}{2}\left(1 + \frac{4}{\alpha_{\mathrm{mn}}^2}\right)}, \tag{169}
$$

where

$$
\alpha_{mn} = \frac{\ell_{mn}}{w_s} \tag{170}
$$

is the element-based source ratio, and δ_x and δ_y are again user-defined parameters, respectively. They denote the points at which the exponential functions with respect to

x_a and y_a no longer maintain significant value in Eq. (167). The conditions given in Eq. (169) physically mean that the projected partially coherent incident beam size must "fit" on the rough surface. In satisfying these conditions the x_a and y_a limits of integration extend to $(-\infty,\infty)$ in Eq. (167). Additionally, if $\delta_x = \delta_y = \delta$, the second condition in Eq. (169) becomes the most stringent within the smooth-to-moderately rough surface analysis.

Assuming that the conditions in Eq. (169) hold, one can then evaluate the remaining integrals in Eq. (167)[14]. In so doing, the following closed-form expression results:

$$\begin{aligned}\Psi_{\mathrm{mn}} = {} & \frac{4\pi^4 r_s^4 \ell_h^2 A_{\mathrm{m}} A_{\mathrm{n}} B_{\mathrm{mn}}}{k_0^2 \left|\hat{\mathbf{y}}\cdot\hat{\mathbf{u}}\right| \left(a_{\mathrm{mn}}^2 - b_{\mathrm{mn}}^2\right)} \exp\left[-\frac{k_0^2\sigma_h^2}{2}\left(\vartheta_{z1}^2+\vartheta_{z2}^2\right)\right] \sum_{l=0}^{\infty} \frac{\left(k_0^2\sigma_h^2\vartheta_{z1}\vartheta_{z2}\right)^l}{l!\sqrt{\mathcal{A}_{l\mathrm{mn}}^x \mathcal{A}_{l\mathrm{mn}}^y}} \\ & \exp\left[-\frac{k_0^2 r_s^2 \ell_h^2}{4\mathcal{D}_{l\mathrm{mn}}^x \mathcal{A}_{l\mathrm{mn}}^x}\left(\mathcal{A}_{l\mathrm{mn}}^x - r_s^2\ell_h^2\right)\left(\vartheta_{x1}^2+\vartheta_{x2}^2\right)\right] \\ & \exp\left[-\frac{k_0^2 r_s^2 \ell_h^2}{4\mathcal{D}_{l\mathrm{mn}}^y \mathcal{A}_{l\mathrm{mn}}^y}\left(\mathcal{A}_{l\mathrm{mn}}^y - r_s^2\ell_h^2\left(\hat{\mathbf{y}}\cdot\hat{\mathbf{u}}\right)^2\right)\left(\vartheta_{y1}^2+\vartheta_{y2}^2\right)\right] \\ & \exp\left[-\frac{r_s^2}{\mathcal{A}_{l\mathrm{mn}}^x}\left(k_0^2\ell_h^2\tilde{b}_{\mathrm{mn}} + l r_s^2\right)\left(\vartheta_{x1}-\vartheta_{x2}\right)^2\right] \\ & \exp\left[-\frac{r_s^2}{\left(\hat{\mathbf{y}}\cdot\hat{\mathbf{u}}\right)^2 \mathcal{A}_{l\mathrm{mn}}^y}\left(k_0^2\ell_h^2\tilde{b}_{\mathrm{mn}}\left(\hat{\mathbf{y}}\cdot\hat{\mathbf{u}}\right)^2 + l r_s^2\right)\left(\vartheta_{y1}-\vartheta_{y2}\right)^2\right] \\ & \exp\left(j\frac{k_0 r_s^3 \ell_h^2}{2\mathcal{A}_{l\mathrm{mn}}^x \mathcal{A}_{l\mathrm{mn}}^y}\left[\mathcal{A}_{l\mathrm{mn}}^y\left(\vartheta_{x1}^2-\vartheta_{x2}^2\right)+\mathcal{A}_{l\mathrm{mn}}^x\left(\vartheta_{y1}^2-\vartheta_{y2}^2\right)\right]\right)\end{aligned} \tag{171}$$

where $(\mathrm{m} = x,u;\ \mathrm{n} = x,u)$ and

14. See Footnote 13, p.66.

$$\begin{aligned}\mathcal{A}_{lmn}^{x} &= r_s^2 \ell_h^2 + 4\left(\tilde{a}_{mn} - \tilde{b}_{mn}\right)\mathcal{D}_{lmn}^{x} \\ \mathcal{A}_{lmn}^{y} &= r_s^2 \ell_h^2 \left(\hat{\mathbf{y}}\cdot\hat{\mathbf{u}}\right)^2 + 4\left(\tilde{a}_{mn} - \tilde{b}_{mn}\right)\mathcal{D}_{lmn}^{y}\end{aligned}. \tag{172}$$

At first glance, the summation somewhat obscures the physical interpretation of Eq. (171). However, further examination of this closed-form expression shows that the exponential terms on the third and fourth lines generally drive the angular extent of the spectral density (SD), whereas the exponential terms on the fourth and fifth lines generally drive the angular extent of the spectral degree of coherence (SDoC). Before exploring these points further in the next chapter, the analysis considers very rough surfaces[15].

4.3.2 Very rough surfaces

When considering very rough surfaces in the analysis, one must expand the surface autocorrelation function found inside the first exponential term in Eq. (161). Here, one retains only the first and second order terms in a Taylor series. To make this concept manifest, the analysis first writes the joint characteristic function found in Eq. (140) in an alternative form, where

$$\begin{aligned}&\chi'\left(\frac{k_0}{r_s}x_1', \frac{k_0}{r_s}x_2', \frac{k_0\left(\hat{\mathbf{y}}\cdot\hat{\mathbf{u}}\right)}{r_s}y_1', \frac{k_0\left(\hat{\mathbf{y}}\cdot\hat{\mathbf{u}}\right)}{r_s}y_2'; x_d, y_d\right) = \\ &\qquad \exp\left(-k_0^2\sigma_h^2\vartheta_{z1}\vartheta_{z2}\left[\frac{\vartheta_{z1}}{2\vartheta_{z2}} + \frac{\vartheta_{z2}}{2\vartheta_{z1}} - \exp\left(-\frac{x_d^2}{\ell_h^2}\right)\exp\left(-\frac{y_d^2}{\ell_h^2}\right)\right]\right)\end{aligned}. \tag{173}$$

In the case of very rough surface conditions, i.e.,

---

15 The following criterion: $\sigma_h \geq 0.5\lambda_0$, helps in discerning the transition point from the smooth-to-moderately rough surface regime to the very rough surface regime and is an empirically determined relationship within the analysis.

$$k_0^2 \sigma_h^2 \vartheta_{z1} \vartheta_{z2} \gg 1, \tag{174}$$

the alternative form found in Eq. (173) maintains significant value when

$$\frac{\vartheta_{z1}}{2\vartheta_{z2}} + \frac{\vartheta_{z2}}{2\vartheta_{z1}} - \exp\left(-\frac{x_d^2}{\ell_h^2}\right)\exp\left(-\frac{y_d^2}{\ell_h^2}\right) \approx 0. \tag{175}$$

Since all of the observation points of interest are in the far field, if one then considers that

$$\frac{\vartheta_{z1}}{2\vartheta_{z2}} \approx \frac{\vartheta_{z2}}{2\vartheta_{z1}}, \tag{176}$$

the relationship found in Eq. (175) is only possible for small x_d and y_d.

With Eqs. (173)-(176) in mind, it makes since to expand the exponential functions found in Eq. (175) and retain only the first and second order terms, so that

$$\exp\left(-\frac{x_d^2}{\ell_h^2}\right)\exp\left(-\frac{y_d^2}{\ell_h^2}\right) \approx 1 - \frac{x_d^2}{\ell_h^2} - \frac{y_d^2}{\ell_h^2}. \tag{177}$$

Substituting Eq. (177) into Eq. (161) allows one to again separate the integrals over the parameterized rough surface. As mentioned before, this allows for the development of a closed-form expression for very rough surface conditions without having to convert to polar coordinates. Carrying out the subsequent integrations[16], the following closed-form expression results:

16. See Footnote 13, p. 66.

$$
\begin{aligned}
\Psi_{\mathrm{mn}} = & \frac{4\pi^4 r_s^4 \ell_h^2 A_{\mathrm{m}} A_{\mathrm{n}} B_{\mathrm{mn}}}{k_0^2 \left|\hat{\mathbf{y}}\cdot\hat{\mathbf{u}}\right| \left(a_{\mathrm{mn}}^2 - b_{\mathrm{mn}}^2\right)} \exp\left[-\frac{k_0^2\sigma_h^2}{2}\left(\vartheta_{z1}-\vartheta_{z2}\right)^2\right] \frac{1}{\sqrt{\mathcal{A}_{\mathrm{mn}}^x \mathcal{A}_{\mathrm{mn}}^y}} \\
& \exp\left[-\frac{k_0^2 r_s^2 \ell_h^2}{4\mathcal{D}_{\mathrm{mn}}^x \mathcal{A}_{\mathrm{mn}}^x}\left(\mathcal{A}_{\mathrm{mn}}^x - r_s^2\ell_h^2\right)\left(\vartheta_{x1}^2+\vartheta_{x2}^2\right)\right] \\
& \exp\left[-\frac{k_0^2 r_s^2 \ell_h^2}{4\mathcal{D}_{\mathrm{mn}}^y \mathcal{A}_{\mathrm{mn}}^y}\left(\mathcal{A}_{\mathrm{mn}}^y - r_s^2\ell_h^2\left(\hat{\mathbf{y}}\cdot\hat{\mathbf{u}}\right)^2\right)\left(\vartheta_{y1}^2+\vartheta_{y2}^2\right)\right] \\
& \exp\left[-\frac{k_0^2 r_s^2}{\mathcal{A}_{\mathrm{mn}}^x}\left(\ell_h^2\tilde{b}_{\mathrm{mn}} + r_s^2\sigma_h^2\vartheta_{z1}\vartheta_{z2}\right)\left(\vartheta_{x1}-\vartheta_{x2}\right)^2\right] \\
& \exp\left[-\frac{k_0^2 r_s^2}{\left(\hat{\mathbf{y}}\cdot\hat{\mathbf{u}}\right)^2 \mathcal{A}_{\mathrm{mn}}^y}\left(\ell_h^2\tilde{b}_{\mathrm{mn}}\left(\hat{\mathbf{y}}\cdot\hat{\mathbf{u}}\right)^2 + r_s^2\sigma_h^2\vartheta_{z1}\vartheta_{z2}\right)\left(\vartheta_{y1}-\vartheta_{y2}\right)^2\right] \\
& \exp\left(j\frac{k_0 r_s^3 \ell_h^2}{2\mathcal{A}_{\mathrm{mn}}^x \mathcal{A}_{\mathrm{mn}}^y}\left[\mathcal{A}_{\mathrm{mn}}^y\left(\vartheta_{x1}^2-\vartheta_{x2}^2\right) + \mathcal{A}_{\mathrm{mn}}^x\left(\vartheta_{y1}^2-\vartheta_{y2}^2\right)\right]\right)
\end{aligned}
, \tag{178}
$$

where $\left(\mathrm{m}=x,u;\ \mathrm{n}=x,u\right)$ and

$$
\begin{aligned}
\mathcal{D}_{\mathrm{mn}}^x &= k_0^2\ell_h^2\left(\tilde{a}_{\mathrm{mn}}+\tilde{b}_{\mathrm{mn}}\right) + 2k_0^2 r_s^2\sigma_h^2\vartheta_{z1}\vartheta_{z2} \\
\mathcal{D}_{\mathrm{mn}}^y &= k_0^2\ell_h^2\left(\tilde{a}_{\mathrm{mn}}+\tilde{b}_{\mathrm{mn}}\right)\left(\hat{\mathbf{y}}\cdot\hat{\mathbf{u}}\right)^2 + 2k_0^2 r_s^2\sigma_h^2\vartheta_{z1}\vartheta_{z2} \\
\mathcal{A}_{\mathrm{mn}}^x &= r_s^2\ell_h^2 + 4\left(\tilde{a}_{\mathrm{mn}}-\tilde{b}_{\mathrm{mn}}\right)\mathcal{D}_{\mathrm{mn}}^x \\
\mathcal{A}_{\mathrm{mn}}^y &= r_s^2\ell_h^2\left(\hat{\mathbf{y}}\cdot\hat{\mathbf{u}}\right)^2 + 4\left(\tilde{a}_{\mathrm{mn}}-\tilde{b}_{\mathrm{mn}}\right)\mathcal{D}_{\mathrm{mn}}^y
\end{aligned}
. \tag{179}
$$

In using the closed-form expression given in Eq. (178), the analysis must satisfy the conditions found in Eq. (169).

The closed-form expression obtained in Eq. (178) is remarkably physical. For instance, the exponential terms on the second and third lines of Eq. (178) are *predominately* responsible for the angular extent of the scattered SD. These exponential terms are functions of the sum of the squares of the observation projections, i.e., $\vartheta_{x1,2}$ and $\vartheta_{y1,2}$. On the other hand, the exponential terms on the fourth and fifth lines of Eq. (178) determine the angular extent of the scattered SDoC. Note that these terms are functions

of the difference of the observation projections, i.e., $\left|\vartheta_{x1}-\vartheta_{x2}\right|$ and $\left|\vartheta_{y1}-\vartheta_{y2}\right|$. Thus, one can state that the closed-form expression obtained in Eq. (178) allows the scattered field CSDM to maintain its GSM form with respect to $\vartheta_{x1,2}$ and $\vartheta_{y1,2}$. The analysis examines these points more closely in the next chapter.

5 Exploration of the 3D vector solution

The purpose of this chapter is to explore the 3D vector solution obtained above in Chapter 4. As stated in Chapter 1, by formulating the 3D vector solution in a manner consistent with Wolf's unified theory of coherence and polarization [12, 13], all physical implications inherent in Wolf's work apply here. Accordingly, one can readily formulate the scattered spectral degree of coherence (SDoC) $\mu^s(\mathbf{r}_1,\mathbf{r}_2)$, the normalized scattered spectral density (SD) $S_N^s(\mathbf{r})$, and the scattered degree of polarization (DoP) $P^s(\mathbf{r})$ from the closed-form expressions developed above for the scattered field cross spectral density matrix (CSDM) $\vec{\vec{\mathbf{W}}}^s(\mathbf{r}_1,\mathbf{r}_2)$. The analysis uses the following relationships [13]:

$$\mu^s(\mathbf{r}_1,\mathbf{r}_2)=\frac{\mathrm{Tr}\left\{\vec{\vec{\mathbf{W}}}^s(\mathbf{r}_1,\mathbf{r}_2)\right\}}{\sqrt{\mathrm{Tr}\left\{\vec{\vec{\mathbf{W}}}^s(\mathbf{r}_1,\mathbf{r}_1)\right\}}\sqrt{\mathrm{Tr}\left\{\vec{\vec{\mathbf{W}}}^s(\mathbf{r}_2,\mathbf{r}_2)\right\}}}, \tag{180}$$

$$S_N^s(\mathbf{r})=\frac{\mathrm{Tr}\left\{\vec{\vec{\mathbf{W}}}^s(\mathbf{r},\mathbf{r})\right\}}{\max\left[\mathrm{Tr}\left\{\vec{\vec{\mathbf{W}}}^s(\mathbf{r},\mathbf{r})\right\}\right]}, \tag{181}$$

and

$$P^s(\mathbf{r})=\sqrt{1-\frac{4\mathrm{Det}\left\{\vec{\vec{\mathbf{W}}}^s(\mathbf{r},\mathbf{r})\right\}}{\left(\mathrm{Tr}\left\{\vec{\vec{\mathbf{W}}}^s(\mathbf{r},\mathbf{r})\right\}\right)^2}}, \tag{182}$$

where $\mathrm{Tr}\{\cdots\}$ denotes the trace operation, $\mathrm{Det}\{\cdots\}$ denotes the determinant operation, and $\mathbf{r}=\mathbf{r}_{1,2}$ corresponds with a single observation point. These relationships contain measurable quantities in practice and serve as metrics in which to compare the 3D vector solution to previously validated solutions and empirical measurements.

Much of the analysis presented in this chapter uses a 5.08 cm × 5.08 cm Labsphere Infragold coupon [142]. It also uses a nominal far-field setup, where

$\lambda_0 = 10.6$ μm, $r_s = r_{1,2} = 185$ cm, and $w_s = 1.9$ mm. As such, the Labsphere Infragold coupon maintains the following complex index of refraction: $n = 13.45 - j63.62$ [143]. Note that a KLA Tencor Alpha-Step IQ Surface Profiler [144] determined the surface statistics of the Labsphere Infragold coupon as $\sigma_h = 11.09$ μm, $\ell_h = 116.9$ μm, and $\sigma_{h'} = 0.2441$ rad [cf. Eq. (191)] using four 1 cm scans (step size 0.2 μm). These surface statistics relate to very rough surface conditions [cf. Eq. (174)].

5.1 Comparison with the 2D scalar-equivalent solution

In order to compare the 3D vector solution to the previously validated 2D scalar-equivalent solution [10, 11], the analysis assumes horizontally polarized (s-pol) illumination and an in-plane scattering geometry, i.e., $A_u = B_{ux} = B_{xu} = 0$ and $\phi^s = \phi^s_{1,2} = 90^\circ$. This provides the setup needed to make a fair comparison between the two solutions.

5.1.1 Angular spectral degree of coherence radius

An individual can formulate a closed-form expression that describes the angular extent over which the scatter field is correlated, i.e., the angular SDoC radius. In general, the angular SDoC radius provides a gauge for the average speckle size observed in the far field and is a quantity of importance when dealing with directed-energy and remote-sensing applications. Note that the analysis presented here is highly analogous to that performed for the 2D scalar-equivalent solution [10, 11].

Because of the summation in Eq. (171), it is not possible to derive a closed-form expression for the angular SDoC radius for smooth-to-moderately rough surfaces. Thus, the present analysis is limited to very rough surfaces. Assuming that Eq. (169) holds, so

that the incident illumination "fits" on the rough surface, the exponential terms on the fourth and fifth lines of Eq. (178), in general, determine the angular extent of the scattered SDoC. Provided s-pol illumination and an in-plane scattering geometry, only Ψ_{xx} exists within the analysis, and the difference of the observation projections simplify, such that

$$\left|\vartheta_{x1}-\vartheta_{x2}\right|=\left|\sin\left(\theta_1^2\right)\cos\left(\phi_1^s\right)-\sin\left(\theta_2^2\right)\cos\left(\phi_2^s\right)\right|=0 \tag{183}$$

and $$\left|\vartheta_{y1}-\vartheta_{y2}\right|=\left|\sin\left(\theta_1^s\right)\sin\left(\phi_1^s\right)-\sin\left(\theta_2^s\right)\sin\left(\phi_2^s\right)\right|=\left|\sin\left(\theta_1^s\right)-\sin\left(\theta_2^s\right)\right|. \tag{184}$$

Consequently, the following "correlation" exponential γ results from Eq. (178) for Ψ_{xx}:

$$\begin{aligned}\gamma&=\exp\left[-\frac{k_0^2r_s^2}{\left(\hat{\mathbf{y}}\cdot\hat{\mathbf{u}}\right)^2\mathcal{A}_{xx}^y}\left(\ell_h^2\tilde{b}_{xx}\left(\hat{\mathbf{y}}\cdot\hat{\mathbf{u}}\right)^2+r_s^2\sigma_h^2\vartheta_{z1}\vartheta_{z2}\right)\left[\sin\left(\theta_1^s\right)-\sin\left(\theta_2^s\right)\right]^2\right]\\&\approx\exp\left[-\frac{r_s^2\mathcal{D}_{xx}^y}{2\left(\hat{\mathbf{y}}\cdot\hat{\mathbf{u}}\right)^2\mathcal{A}_{xx}^y}\left[\sin\left(\theta_1^s\right)-\sin\left(\theta_2^s\right)\right]^2\right]\end{aligned}. \tag{185}$$

Upon setting γ equal to $1/\mathrm{e}$, the following expression results:

$$\begin{aligned}\left|\sin\left(\theta_1^s\right)-\sin\left(\theta_2^s\right)\right|_{1/\mathrm{e}}&\approx\frac{\left|\hat{\mathbf{y}}\cdot\hat{\mathbf{u}}\right|}{r_s}\sqrt{\frac{2A_{xx}^y}{\mathcal{D}_{xx}^y}}\\&=\frac{\left|\hat{\mathbf{y}}\cdot\hat{\mathbf{u}}\right|}{r_s}\sqrt{\frac{8w_s^2\ell_{xx}^2}{\ell_{xx}^2+4w_s^2}+\frac{2r_s^2\ell_h^2\left(\hat{\mathbf{y}}\cdot\hat{\mathbf{u}}\right)^2}{k_0^2\left[\ell_h^2w_s^2\left(\hat{\mathbf{y}}\cdot\hat{\mathbf{u}}\right)^2+2r_s^2\sigma_h^2\vartheta_{z1}\vartheta_{z2}\right]}}\end{aligned}. \tag{186}$$

Because the magnitude of the argument of γ is large (specifically the $k_0^2r_s^4\sigma_h^2\vartheta_{z1}\vartheta_{z2}$ term), $\sin\left(\theta_1^s\right)\approx\sin\left(\theta_2^s\right)$ for Eq. (185) to have a significant value. This implies that $\theta_1^s\approx\theta_2^s$ and that γ is approximately a function of $\Delta\theta^s=\theta_1^s-\theta_2^s$. Using this insight, Eq. (186) simplifies because

$$\begin{aligned}\sin\left(\theta_1^s\right) &= \sin\left(\theta_2^s + \Delta\theta^s\right) \\ &= \sin\left(\theta_2^s\right)\cos\left(\Delta\theta^s\right) + \cos\left(\theta_2^s\right)\sin\left(\Delta\theta^s\right), \\ &\approx \sin\left(\theta_2^s\right) + \cos\left(\theta_2^s\right)\Delta\theta^s\end{aligned} \tag{187}$$

$$\begin{aligned}\cos\left(\theta_1^s\right) &= \cos\left(\theta_2^s + \Delta\theta^s\right) \\ &= \cos\left(\theta_2^s\right)\cos\left(\Delta\theta^s\right) - \sin\left(\theta_2^s\right)\sin\left(\Delta\theta^s\right), \\ &\approx \cos\left(\theta_2^s\right)\end{aligned} \tag{188}$$

and

$$\begin{aligned}\frac{\vartheta_{z1}\vartheta_{z2}}{\left(\hat{\mathbf{y}}\cdot\hat{\mathbf{u}}\right)^2} &= \frac{\left[\cos\left(\theta_1^s\right)+\cos\left(\theta^i\right)\right]\left[\cos\left(\theta_2^s\right)+\cos\left(\theta^i\right)\right]}{\cos^2\left(\theta^i\right)} \\ &\approx \left[1+\frac{\cos\left(\theta_2^s\right)}{\cos\left(\theta^i\right)}\right]^2\end{aligned} \tag{189}$$

After some simple algebra, the expression for the angular SDoC radius becomes

$$\left|\Delta\theta^s\right|_{1/\mathrm{e}} \approx \frac{1}{\varpi r_s}\sqrt{\frac{8w_s^2}{1+\left(2/\alpha_{xx}\right)^2}+\frac{2}{k_0^2\sigma_{h'}^2\left(1+\varpi\right)^2\left(1+\left[\dfrac{\Omega_s}{\sigma_{h'}^2\left(1+\varpi\right)}\right]^2\right)}}, \tag{190}$$

where $\alpha_{xx} = \ell_{xx}/w_s$ is a source ratio [cf. Eq. (170)], $\varpi = \cos\left(\theta_2^s\right)/\cos\left(\theta^i\right)$ is a projection ratio, $\Omega_s = w_s/r_s$ is the source half angle (viewed from the rough surface), and

$$\sigma_{h'} = \sqrt{2}\,\frac{\sigma_h}{\ell_h} \tag{191}$$

is the surface slope standard deviation [36][17].

17. Based on the assumptions used within the analysis [cf. Footnote 10, p.56], valid surface slope standard deviations must satisfy the following condition: $\sigma_{h'} \le 0.25$ rad [35, 66].

For all intents and purposes, one can neglect the term involving $\Omega_s/\sigma_{h'}$ in Eq. (190). This ratio results in values on the order of 10^{-4} for most directed-energy and remote-sensing engagement scenarios. With this said, one can also claim that the source term contained in the radical above is much greater than the surface term. Thus, factoring out the source term and using the binomial approximation yields

$$\begin{aligned}\left|\Delta\theta^s\right|_{1/e} &\approx \frac{\Omega_s}{\varpi}\left(2\sqrt{\frac{2}{1+\left(2/\alpha_{xx}\right)^2}}+\frac{\sqrt{2\left[1+\left(2/\alpha_{xx}\right)^2\right]}}{4k_0^2w_s^2\sigma_{h'}^2\left(1+\varpi\right)^2}\right). \\ &\approx \frac{2\Omega_s}{\varpi}\sqrt{\frac{2}{1+\left(2/\alpha_{xx}\right)^2}}\end{aligned} \tag{192}$$

For most cases of interest, one can neglect the second term contained within the parenthesis in Eq. (192). It only provides a "small" correction to the angular SDoC radius due to the surface parameters. As a result, the angular SDoC radius becomes a function of only the source parameters. This is highly analogous to the result obtained by the 2D scalar-equivalent solution [10, 11]. It is also consistent with the classic, narrow-band, fully coherent illumination result derived by Goodman [90].

5.1.2 Angular spectral density radius

An individual can also formulate a closed-form expression for the angular SD radius. In general, the angular SD radius provides a gauge for the size of the average power distribution observed in the far field. This is a quantity of importance when dealing with directed-energy and remote-sensing applications. The analysis, yet again, is highly analogous to that performed for the 2D scalar-equivalent solution [10, 11].

As was the case for the angular SDoC radius, the summation in Eq. (171) does not allow for a closed-form expression for the angular SD radius for smooth-to-moderately rough surfaces. Furthermore, one must limit the analysis to near normal incidence, so that $\left|\hat{\mathbf{y}}\cdot\hat{\mathbf{u}}\right| = \cos\left(\theta^i\right) \approx 1$. Assuming that Eq. (169) holds, so that the incident illumination "fits" on the rough surface, the exponential terms on the second and third lines of Eq. (178) *predominantly* determine the angular extent of the scattered SD for very rough surfaces. Provided s-pol illumination, only Ψ_{xx} exists within the analysis. In addition, for an in-plane scattering geometry and a single observation point, i.e., $\mathbf{r} = \mathbf{r}_{1,2}$, the observation projections simplify, such that

$$\vartheta_x = \vartheta_{x1,2} = \sin\left(\theta^s\right)\cos\left(\phi^s\right) = 0 \tag{193}$$

and

$$\vartheta_y = \vartheta_{y1,2} = \sin\left(\theta^s\right)\sin\left(\phi^s\right) = \sin\left(\theta^s\right). \tag{194}$$

Consequently, the following "power-distribution" exponential β results from Eq. (178) for Ψ_{xx}:

$$\beta = \exp\left[-\frac{k_0^2 r_s^2 \ell_h^2}{2\mathcal{D}_{\mathrm{mn}}^y \mathcal{A}_{\mathrm{mn}}^y}\left(\mathcal{A}_{\mathrm{mn}}^y - r_s^2 \ell_h^2\right)\sin^2\left(\theta^s\right)\right]. \tag{195}$$

Upon setting β equal to $1/\mathrm{e}$, the following expression results:

$$\sin^2\left(\theta_{1/\mathrm{e}}^s\right) = 2\Omega_s^2 + 2\sigma_{h'}^2\left[1+\cos\left(\theta_{1/\mathrm{e}}^s\right)\right]^2 + \frac{1+\left(2/\alpha_{xx}\right)^2}{2k_0^2 w_s^2}. \tag{196}$$

Since $\sin^2\left(\theta_{1/\mathrm{e}}^s\right) = 1-\cos^2\left(\theta_{1/\mathrm{e}}^s\right)$, Eq. (196) manipulates into a quadratic equation in terms of $\cos\left(\theta_{1/\mathrm{e}}^s\right)$, where

$$0 = \left(1+2\sigma_{h'}^2\right)\cos^2\left(\theta_{\mathrm{l/e}}^s\right) + 4\sigma_{h'}^2\cos\left(\theta_{\mathrm{l/e}}^s\right) + 2\left(\Omega_s^2+\sigma_{h'}^2\right) + \frac{1+\left(2/\alpha_{xx}\right)^2}{2k_0^2w_s^2} - 1. \qquad (197)$$

Solving this quadratic equation (only the positive root makes physical sense), the angular SD radius becomes

$$\begin{aligned}\theta_{\mathrm{l/e}}^s &= \cos^{-1}\left(\frac{1}{1+2\sigma_{h'}^2}\left[1+\sqrt{1-\left(1+2\sigma_{h'}^2\right)\left(2\Omega_s^2+\frac{1+\left(2/\alpha_{xx}\right)^2}{2k_0^2w_s^2}\right)}\right]-1\right). \\ &\approx \cos^{-1}\left(\frac{2}{1+2\sigma_{h'}^2}-1\right)\end{aligned} \qquad (198)$$

For most cases of interest, the source and surface terms contained within the radical in Eq. (198) are negligible. They only provide a "small" correction to the angular SD radius due to the source parameters. Thus, the angular SD radius becomes a function of only the surface parameters. This is highly analogous to the result obtained by the 2D scalar-equivalent solution [10, 11].

5.1.3 Fully coherent illumination validation

In order to validate the angular radii developed above, the present analysis uses the Labsphere Infragold coupon and the nominal far-field setup (described above) with fully coherent illumination at normal incidence, so that $\ell_{xx} = 1000w_s$ and $\theta^i = 0^\circ$. Provided this setup, Figure 10 shows a comparison between the 3D vector solution, the 2D scalar-equivalent solution [10, 11], and a full-wave 2D method of moments (MoM) solution [139, 140]. The 2D MoM solution obtained the scattered field from 400 independent rough surface realizations simulated using the method described by Yura and Hanson [145] with a Gaussian-Gaussian (G-G) probability distribution function

(PDF) [cf. Eq. (138)][18]. Note that the results match up well and that the closed-form expressions for the angular radii behave as predicted. For instance, the dashed vertical line in Figure 10a, which represents the angular SDoC radius [cf. Eq. (192)], identifies the correct $1/e$ location, whereas the dashed vertical lines in Figure 10b, which represent the angular SD radius [cf. Eq. (198)], come close to the $1/e$ locations. The analysis performed in the next sub-section further explains this small disagreement with respect to the angular SD radius; nonetheless, the results in Figure 10 help to validate the 3D vector solution assuming fully coherent illumination and very rough surface conditions.

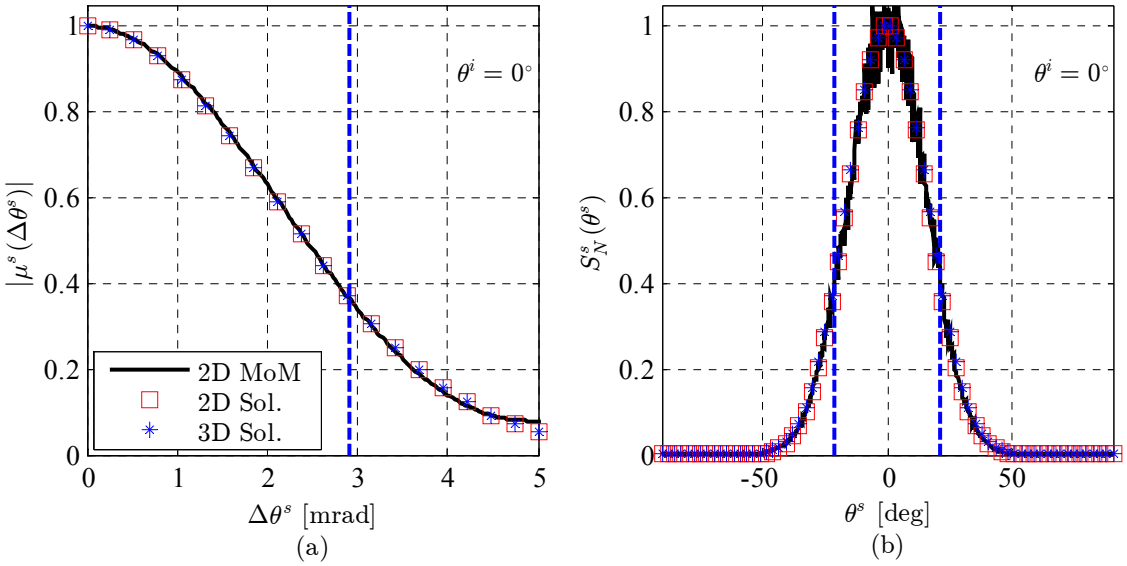

Figure 10. Comparison between a full-wave 2D method of moments (MoM) solution, the 2D scalar-equivalent solution, and the 3D vector solution for fully coherent illumination at normal incidence of a very rough conducting surface. (a) shows the magnitude of the scattered spectral degree of coherence as a function of the difference between two polar angles, whereas (b) shows the normalized scattered spectral density as a function of a single polar angle.

18. A full-wave 3D MoM solution is unrealizable at optical wavelengths with the current fully coherent setup—the computational sampling and memory requirements are far too great for modern desktop computers.

In order to validate the 3D vector solution for smooth-to-moderately rough surface conditions, the analysis assumes the same nominal far-field setup used above but varies the surface height standard deviations of the Labsphere Infragold coupon, so that $\sigma_h = 0.0\lambda_0,\ 0.1\lambda_0,$ and $0.3\lambda_0$. Figure 11 shows the results for this setup. Note that for both the magnitude of the scattered SDoC (Figure 11a) and the normalized scattered SD (Figure 11b), the results deviate for small σ_h between the 3D and 2D solutions. This is most likely due to fact that the 2D scalar-equivalent solution is confined to a single plane, whereas the 3D vector solution is not. The results of Hyde *et al.* showed excellent agreement between the 2D scalar-equivalent solution and a full-wave 2D MoM solution using similar setup parameters [11]. With this said, the 2D solutions do not capture all the physics related to the 3D vector problem—the next sub-section examines this point further at normal and non-normal incidence using partially coherent illumination.

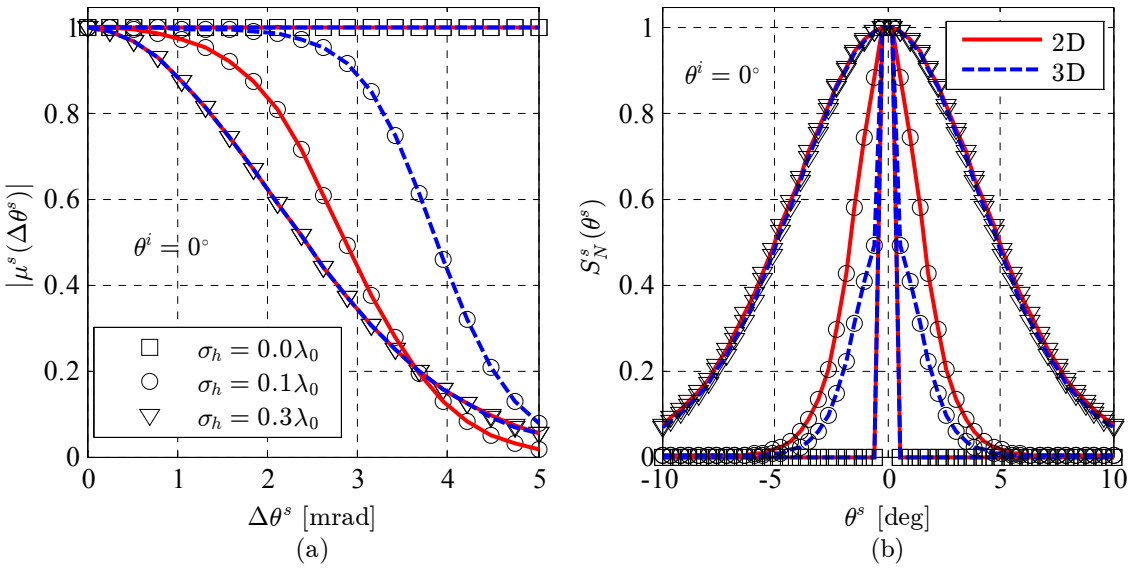

Figure 11. Comparison between the 2D scalar-equivalent and 3D vector solutions for fully coherent illumination at normal incidence of smooth-to-moderately rough conducting surfaces. (a) shows the magnitude of the scattered spectral degree of coherence as a function of the difference between two polar angles. (b) shows the normalized scattered spectral density as a function of a single polar angle.

5.1.4 Partially coherent illumination validation

The present analysis varies the coherence of the incident illumination, so that $\alpha_{xx} = 2$, 1, 0.5, and 0.25 [cf. Eq. (170)], where $w_s = 1.9$ mm and $\ell_{xx} = \alpha_{xx} w_s$. These values relate to a coherent source and to a relatively incoherent source, respectively. In addition, the present analysis varies the surface roughness of the Labsphere Infragold coupon, so that $\sigma_{h'} = 0.01$ rad, 0.05 rad, 0.1 rad, and 0.25 rad [cf. Eq. (191)], where $\ell_h = 116.9$ μm and $\sigma_h = \sigma_{h'} \ell_h / \sqrt{2}$. These values relate with smooth-to-very rough surface conditions, respectively. Figure 12 and Figure 13 below show results for the magnitude of the scattered SDoC and the normalized scattered SD for partially coherent illumination at normal incidence, i.e., $\theta^i = 0^\circ$. Note the excellent agreement between the 2D and 3D solutions (similar to that achieved for the fully coherent illumination analysis).

Figure 14 shows the results for the normalized scattered SD for partially coherent illumination at non-normal incidence, i.e., $\theta^i = 40^\circ$. Here, the results deviate between the 2D and 3D solutions as $\sigma_{h'}$ increases. This deviation is deterministic in practice. For s-pol illumination and an in-plane scattering geometry, the 2D and 3D solutions have the same functional dependence in the exponential term which *predominately* drives the angular extent of the scattered SD. The analysis explored this functional dependence above in the derivation of the angular SD radius. With that said, there is a small difference contained in the amplitude terms when comparing the 2D and 3D solutions.

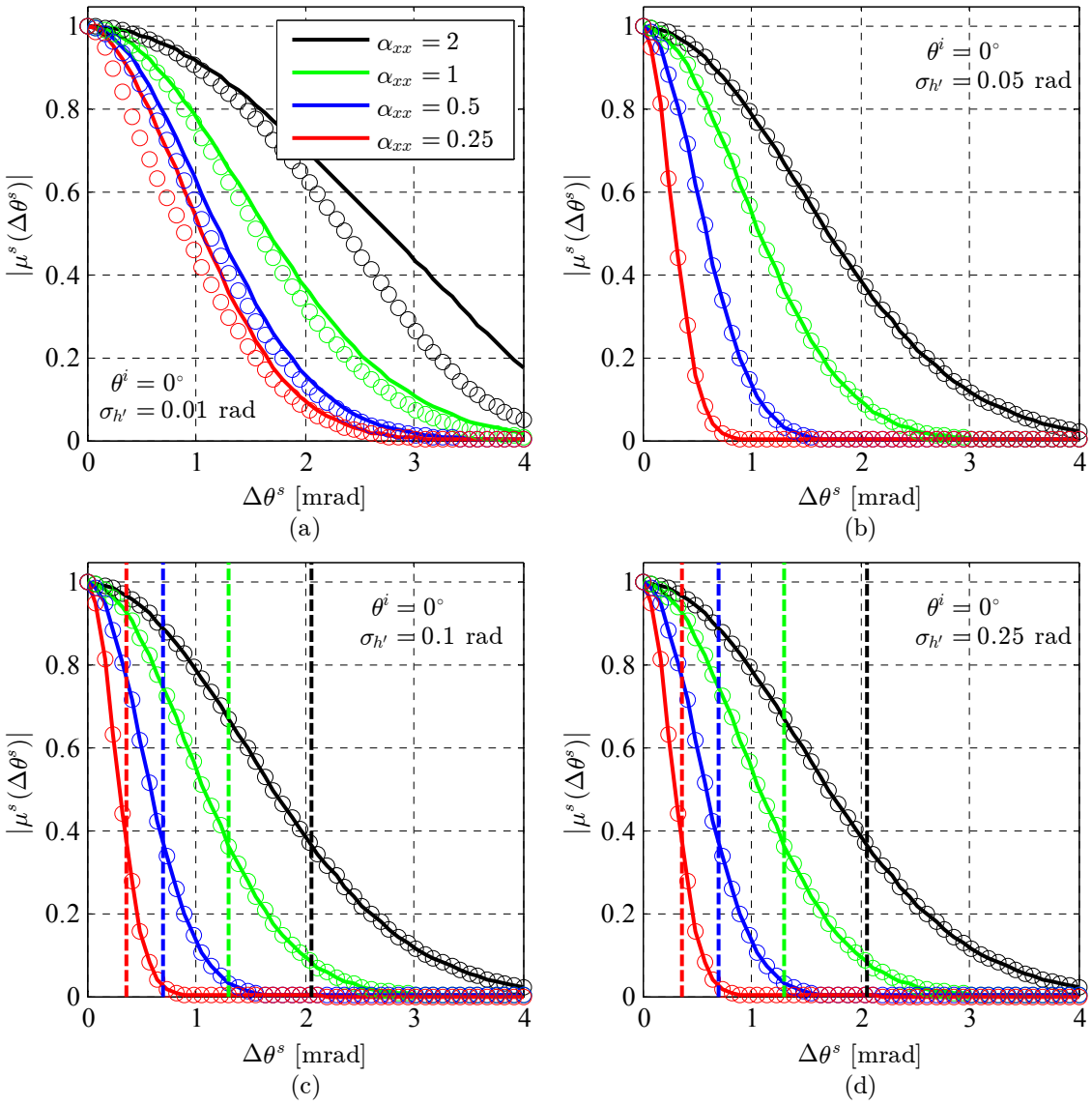

Figure 12. Comparison between the 2D solution (circles) and 3D solution (lines) for partially coherent illumination at normal incidence of smooth-to-very rough conducting surfaces. (a)-(d) shows the magnitude of the scattered spectral degree of coherence as a function of the difference between two polar angles for varying source parameter ratios and surface slope standard deviations.

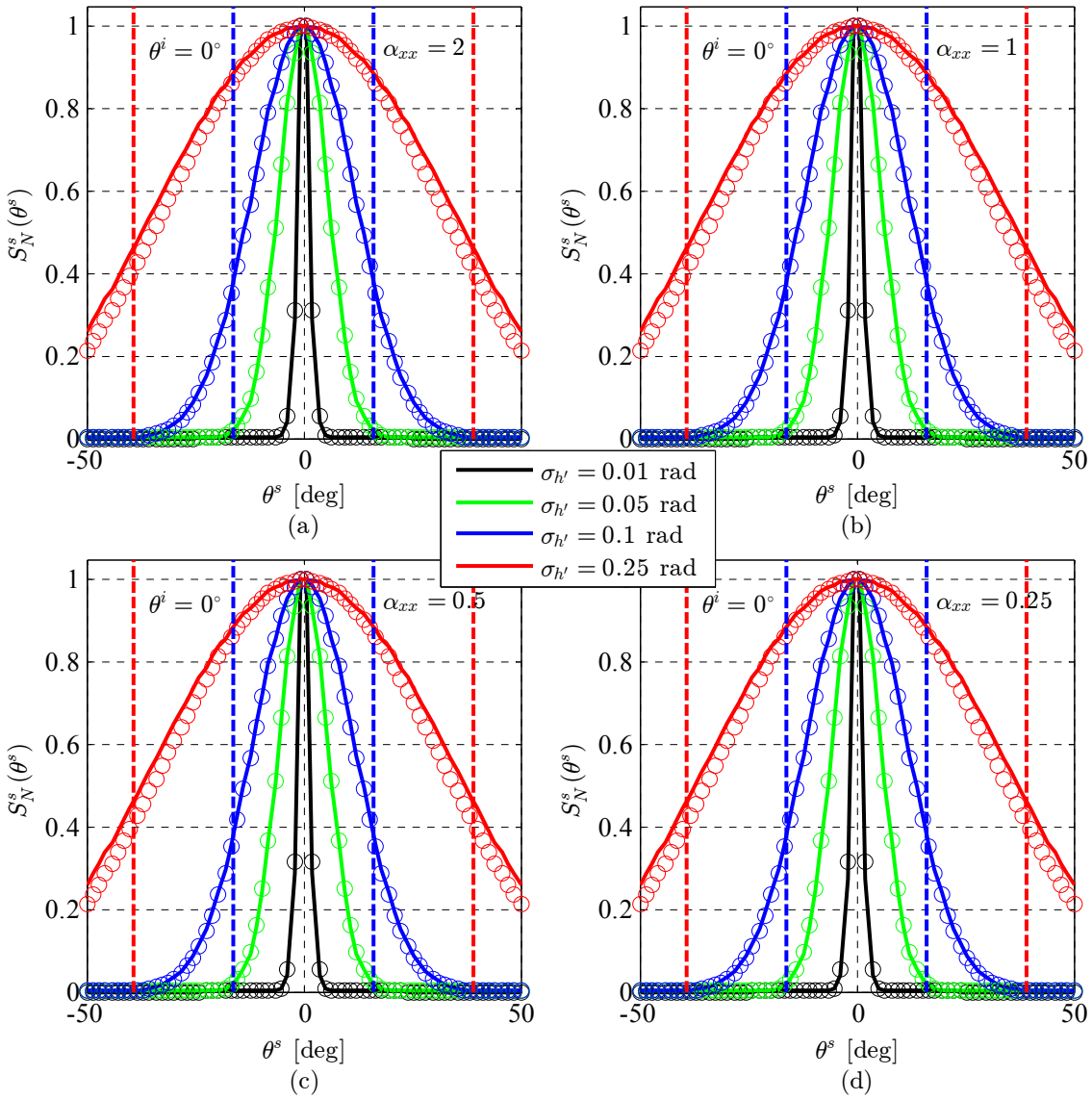

Figure 13. Comparison between the 2D solution (circles) and 3D solution (lines) for partially coherent illumination at normal incidence of smooth-to-very rough conducting surfaces. (a)-(d) shows the normalized scattered spectral density as a function of a single polar angle for varying source parameter ratios and surface slope standard deviations.

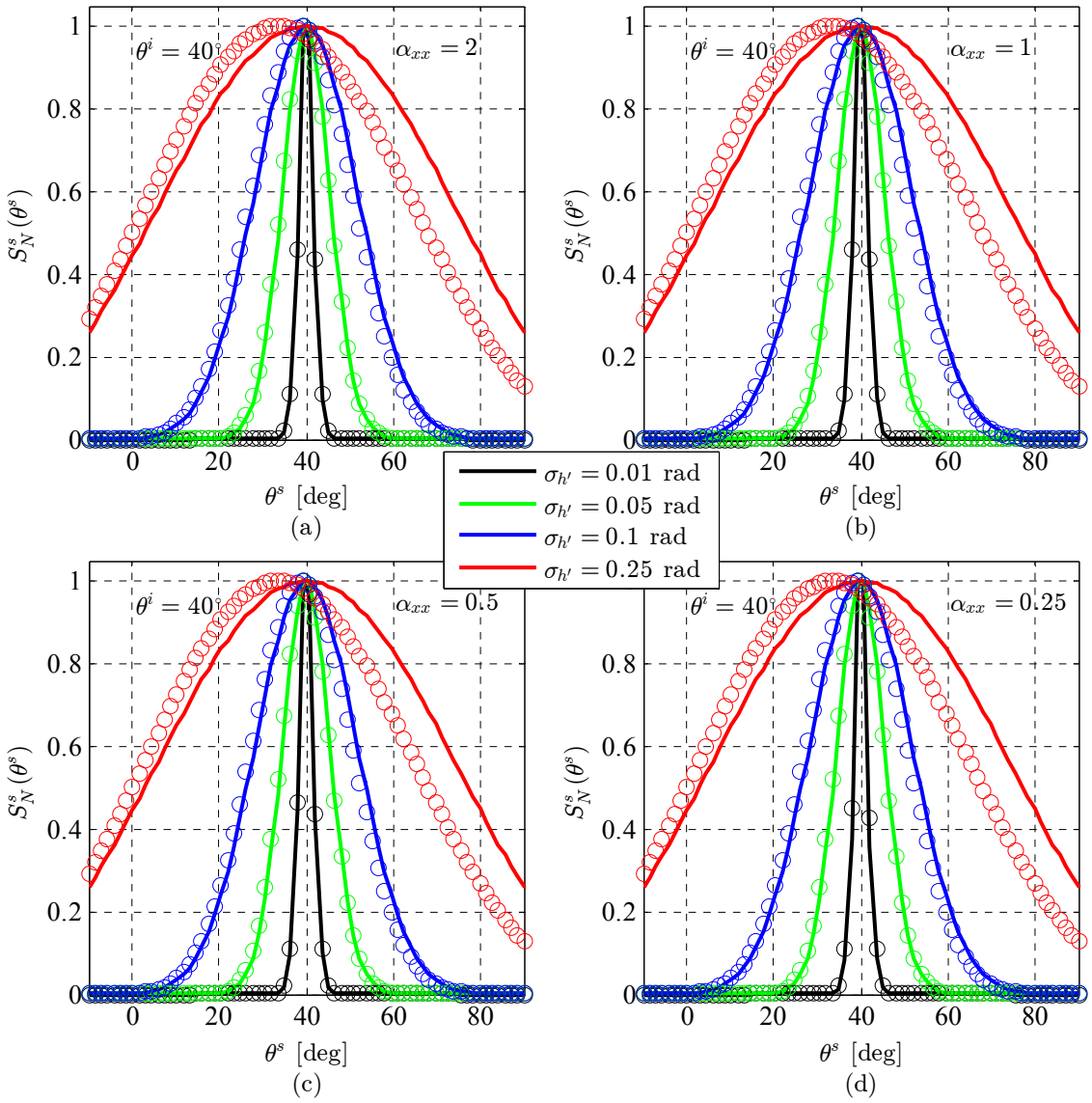

Figure 14. Comparison between the 2D solution (circles) and 3D solution (lines) for partially coherent illumination at non-normal incidence of smooth-to-very rough conducting surfaces. (a)-(d) shows the normalized scattered spectral density as a function of a single polar angle for varying source parameter ratios and surface slope standard deviations.

The 3D vector solution contains a $1/\sqrt{\mathcal{A}_{xx}^{x}\mathcal{A}_{xx}^{y}}$ amplitude factor; whereas, the 2D scalar-equivalent solution contains only a $1/\sqrt{\mathcal{A}_{xx}^{y}}$ amplitude factor [cf. Eqs. (172) and (179)]. These amplitude factors (in addition to polarization terms) appear in front of the exponential term which *predominantly* drives the angular extent of the scattered SD. Functionally, these amplitude factors tend to "push" the scattered SD to the right, whereas the polarization terms tend to "pull" the scattered SD to the left (for positive incident angles—the opposite is true for negative incident angles). The additional amplitude factor contained in the 3D solution pushes the scattered SD, so that the peak of the far-field power distribution always aligns with the specular direction, i.e., where $\theta^s = \theta^i$. Conversely, Figure 14 shows that for the 2D solution, as $\sigma_{h'}$ increases the SD peak shifts more and more to the left and does not align with the specular direction[19]. This is due to the lack of the aforementioned amplitude factor.

Before moving on in the analysis, it is important to note that these said amplitude factors are also responsible for the discrepancy seen in the angular SD radius (cf. the vertical dashed lines in Figure 10 and Figure 13). The angular SD radius only comes close to the $1/e$ locations because these amplitude factors tend to "push" out the wings of the far-field power distribution. Nevertheless, this behavior is deterministic in nature and the angular SD radius, as derived above, adequately characterizes the behavior of the scattered SD.

19. The full-wave 2D MoM solution of Basu *et al.* shows similar behavior [139, 140].

5.2 Comparison to a polarimetric bidirectional distribution function

The analysis presented here compares the 3D vector solution to a polarimetric bidirectional distribution function (pBRDF) developed by Priest and Meier [49]. In general, the pBRDF of Priest and Meier assumes fully incoherent illumination; thus, there is no coherence information contained within the solution. Instead, the pBRDF of Priest and Meier provides the Mueller matrix for statistically rough surfaces that are characterized by a G-G PDF [cf. Eq. (138)]; as a result, if the analysis assumes unpolarized illumination, then the first column of the Mueller matrix (given by the pBRDF solution) becomes the scattered Stokes vector [23, 30]. Provided this scattered Stokes vector, the analysis can then compare the normalized scattered SD and the scattered DoP between the pBRDF solution and the 3D vector solution.

5.2.1 Normalized spectral density validation

The present analysis uses the Labsphere Infragold coupon and the nominal far-field setup (described above). It also assumes unpolarized illumination, so that $A_x = A_u$ and $B_{xu} = B_{ux} = 0$. Figure 15 shows results for this setup with partially coherent illumination at non-normal incidence, where $\alpha_{xx} = \alpha_{uu} = 0.5$ and $\theta^i = 20^\circ$. Note the exact agreement between the pBRDF and 3D solutions for the normalized SD with various scattering geometries. Also note that one can obtain the normalized scattered SD from the pBRDF solution by cosine correcting the first term of the scattered Stokes vector [34], i.e., multiplying by $\cos\left(\theta^s\right)$, and dividing by the max value.

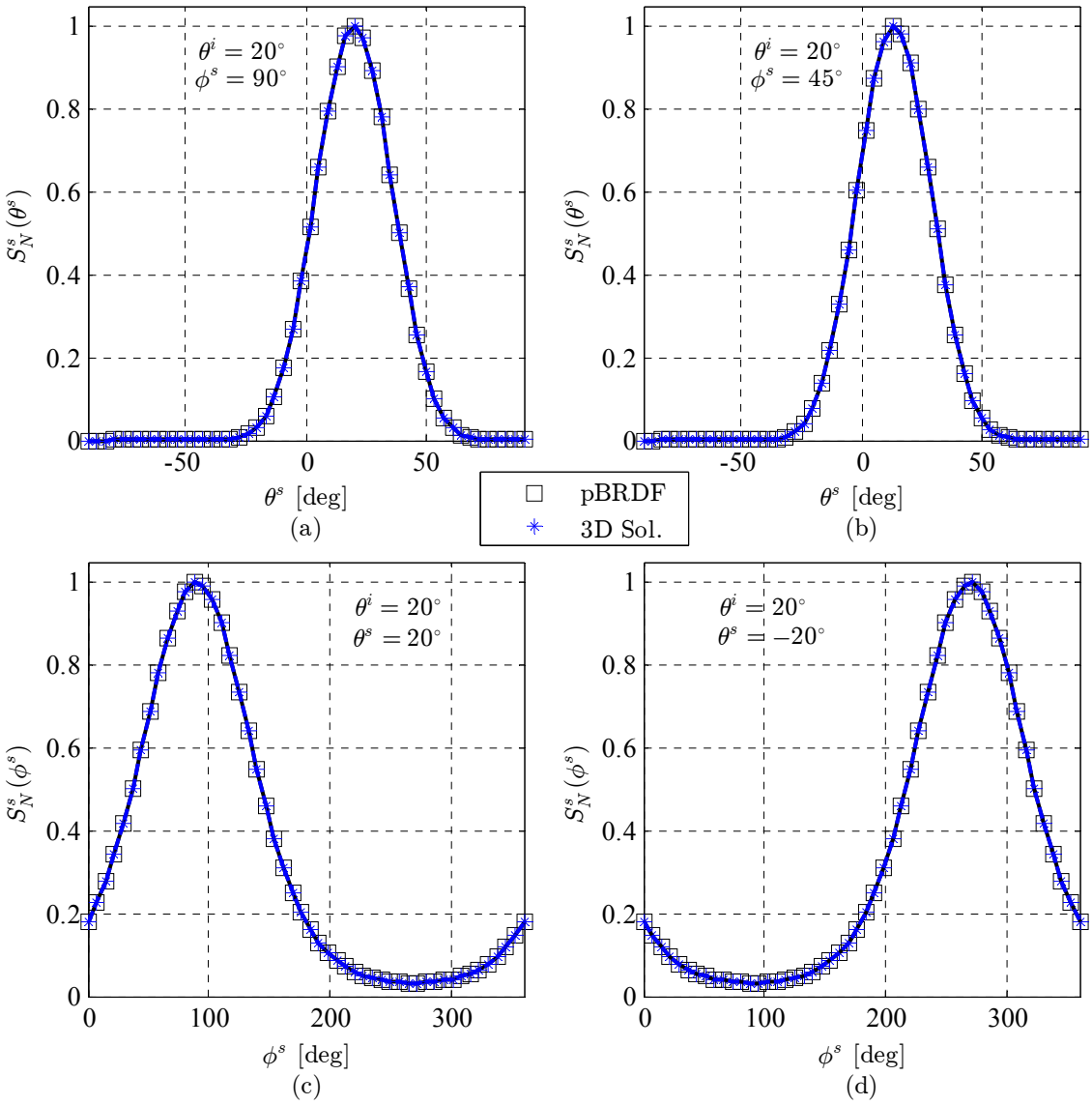

Figure 15. Comparison of the normalized scattered spectral densities obtained from a polarimetric bidirectional distribution function (pBRDF) and the 3D vector solution for unpolarized illumination at non-normal incidence and a very rough conducting surface. (a) depicts an in-plane scattering geometry, whereas (b) depicts an out-of-plane scattering geometry with results as a function of a single polar angle. Conversely, (c) and (d) depict bi-static scattering geometries as a function of a single azimuth angle. Note that the minimum occurs at the mono-static observation point in both (c) and (d).

5.2.2 Degree of polarization validation

The initial analysis presented here again uses the Labsphere Infragold coupon and the nominal far-field setup (described above). It also assumes unpolarized illumination throughout, so that $A_x = A_u$ and $B_{xu} = B_{ux} = 0$. Figure 16 shows results for partially coherent illumination at non-normal incidence, where again $\alpha_{xx} = \alpha_{uu} = 0.5$ and $\theta^i = 20^\circ$. Note the exact agreement between the pBRDF and 3D solutions for the scattered DoP with various scattering geometries.

Now the analysis assumes a tactical engagement scenario, so that $\lambda_0 = 1.064$ μm, $r_s = r_{1,2} = 10$ km, $w_s = 2.54/2$ cm, $\ell_{xx} = \ell_{uu} = 0.25 w_s$, and $\theta^i = 56.4^\circ$. This setup corresponds with partially coherent illumination of NKB7 glass, where $n = 1.507$ [143], at Brewster's angle. The results presented in Figure 17a show exact agreement between the pBRDF and 3D solutions for scattered DoP assuming very rough surface conditions, where $\ell_h = 100\lambda_0$ and $\sigma_h = 10\lambda_0$. Figure 17b then shows results for both very rough and smooth-to-moderately rough surface conditions using only the 3D vector solution, where again $\ell_h = 100\lambda_0$ but $\sigma_h = 10\lambda_0$ and $0.1\lambda_0$. It is important to note that the scattered DoP only exists where light exists in the analysis. This makes sense considering that, by definition, the scattered DoP depends on the scattered SD [cf. Eqs. (181) and (182)]. With that said, Figure 17b shows that the scattered DoP does not depend on surface roughness, at least for the assumptions used within the analysis [cf. Footnote 10, p.55]. It also does not depend on coherence, at least for unpolarized incident illumination—this is consistent with the examples given by Wolf for isotropic beam parameters [13], i.e., when $\ell_{xx} = \ell_{uu}$ (Appendix E shows an example where this is not the case).

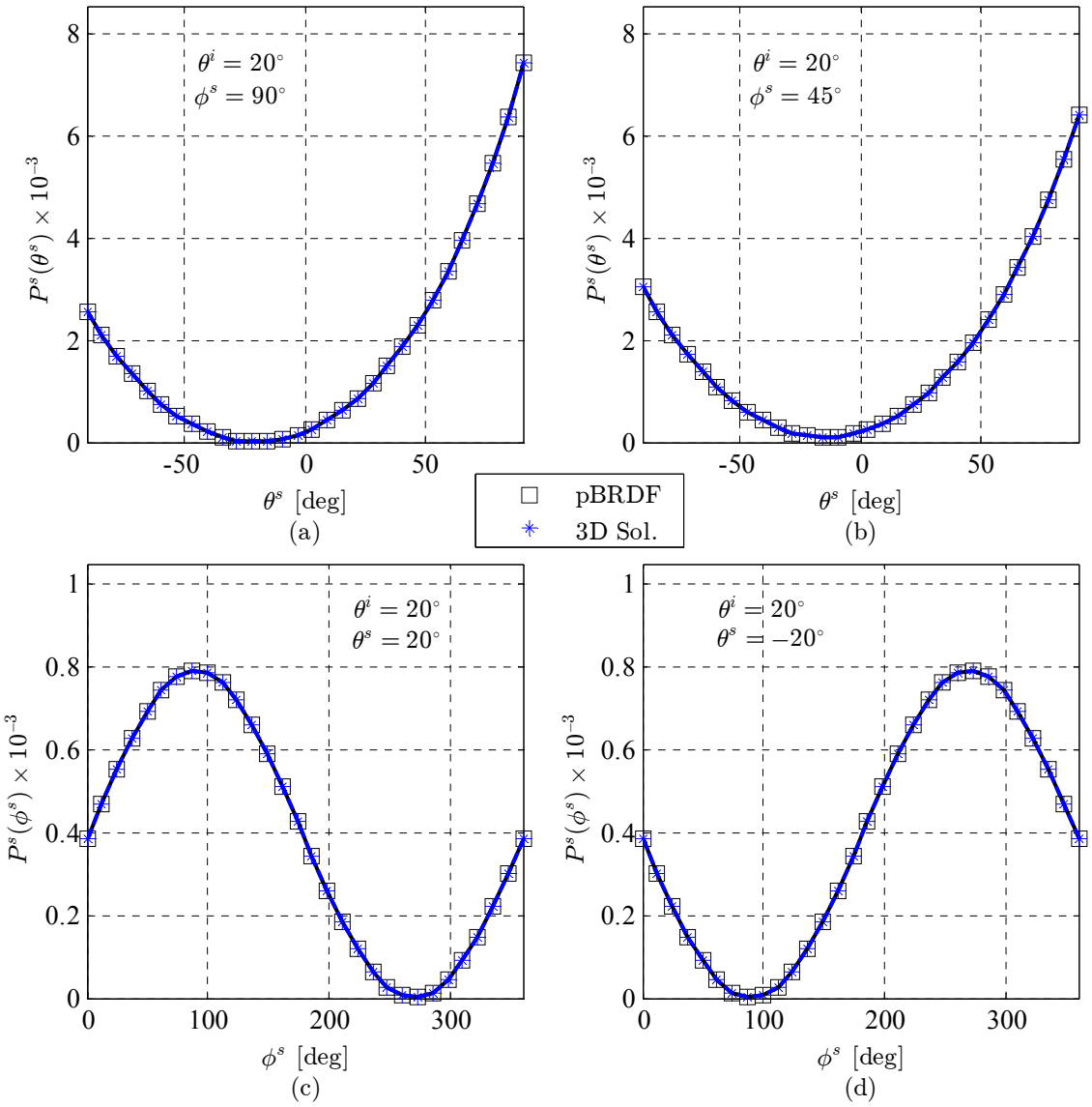

Figure 16. Comparison of the scattered degree of polarization obtained from a polarimetric bidirectional distribution function (pBRDF) and the 3D vector solution for unpolarized illumination at non-normal incidence and a very rough conducting surface. (a) depicts an in-plane scattering geometry, whereas (b) depicts an out of plane scattering geometry with results as a function of a single polar angle. Conversely, (c) and (d) depict bi-static scattering geometries as a function of a single azimuth angle. Note that the minimum occurs at the mono-static observation point in both (c) and (d).

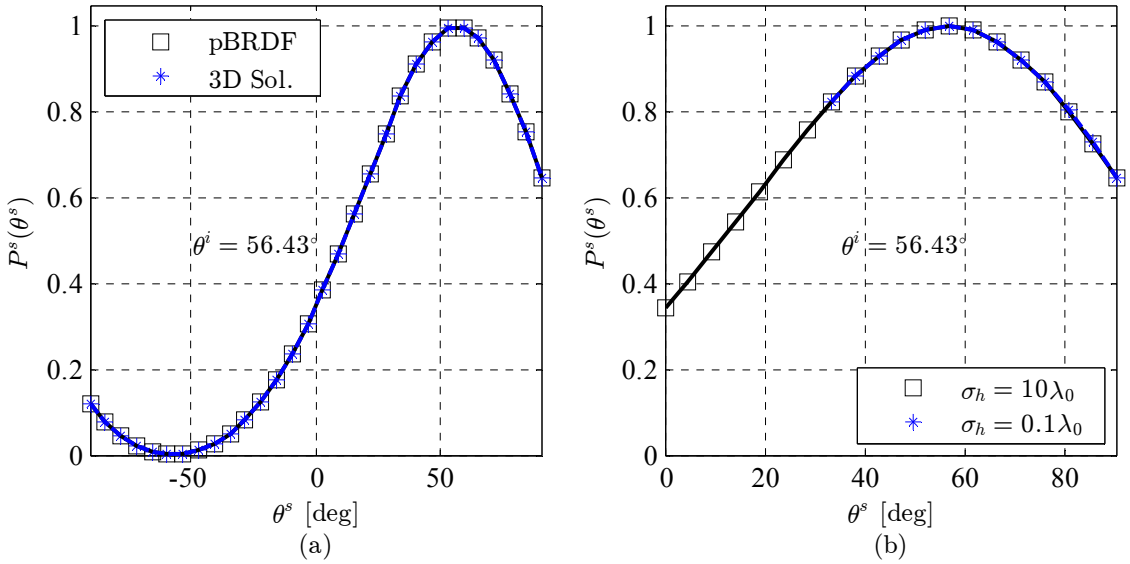

Figure 17. Comparison of the scattered degree of polarization for unpolarized illumination at Brewster's angle of a dielectric surface with varying roughness conditions. (a) shows the results obtained from a polarimetric bidirectional distribution function (pBRDF) and the 3D vector solution for non-normal incidence at Brewster's angle with very rough surface conditions. (b) shows the results from the 3D vector solution for both very rough and smooth-to-moderately rough surface conditions.

5.3 Comparison to empirical measurements

To compare the 3D vector solution with empirical measurements, the analysis uses results from the Complete Angle Scatter Instrument (CASI) at the Air Force Institute of Technology [146][20]. Figure 18 describes the scattering geometry associated with the CASI for both in-plane measurements (Figure 18a) and out-of-plane measurements (Figure 18b). Provided Figure 18, the analysis uses the following angle transformations, developed by Germer and Asmail [148], to relate the CASI scattering geometry to that of the 3D vector solution (cf. Figure 9):

$$\theta^i = \cos^{-1}\left[\cos\left(\alpha^s\right)\cos\left(\beta^s\right)\right], \tag{199}$$

20. Goldstein readily describes the principles behind dual-rotating-retarder polarimety [147, p. 357].

$$\theta^s = \cos^{-1}\left[\cos\left(\beta^s\right)\sin\left(\alpha^s\right)\sin\left(\delta^s\right)+\cos\left(\alpha^s\right)\cos\left(\beta^s\right)\cos\left(\delta^s\right)\right], \tag{200}$$

and

$$\phi^s = \tan^{-1}\left(b^s, a^s\right)+\frac{3\pi}{2}-\tan^{-1}\left(b^i, a^i\right). \tag{201}$$

In Eq. (201), $\tan^{-1}(b,a)$ returns the inverse tangent of b/a after taking into account the quadrant of the point (a,b). With this in mind,

$$\begin{aligned} b^s = {} & \sin\left(\delta^s\right)\left[\cos\left(\gamma^s\right)\sin\left(\alpha^s\right)\sin\left(\beta^s\right)+\cos\left(\sin\left[\gamma^s\right]\right)\right] \\ & +\cos\left(\delta^s\right)\left[\cos\left(\alpha^s\right)\cos\left(\gamma^s\right)\sin\left(\beta^s\right)-\sin\left(\alpha^s\right)\sin\left(\gamma^s\right)\right] \end{aligned}, \tag{202}$$

$$\begin{aligned} a^s = {} & -\cos\left(\delta^s\right)\left[-\cos\left(\gamma^s\right)\sin\left(\alpha^s\right)-\cos\left(\alpha^s\right)\sin\left(\beta^s\right)\sin\left(\gamma^s\right)\right] \\ & +\sin\left(\delta^s\right)\left[\cos\left(\alpha^s\right)\cos\left(\gamma^s\right)-\sin\left(\alpha^s\right)\sin\left(\beta^s\right)\sin\left(\gamma^s\right)\right] \end{aligned}, \tag{203}$$

$$b^i = \cos\left(\alpha^s\right)\cos\left(\gamma^s\right)\sin\left(\beta^s\right)-\sin\left(\alpha^s\right)\sin\left(\gamma^s\right)\Big], \tag{204}$$

and

$$a^i = -\cos\left(\gamma^s\right)\sin\left(\alpha^s\right)-\cos\left(\alpha^s\right)\sin\left(\beta^s\right)\sin\left(\gamma^s\right). \tag{205}$$

Provided Eqs. (199)-(205), the following analysis uses the Labsphere Infragold coupon and the nominal far-field setup (described above). These setup parameters best match those used by the CASI. It also assumes unpolarized partially coherent illumination at non-normal incidence, so that $A_x = A_u$, $B_{xu} = B_{ux} = 0$, $\alpha_{xx} = \alpha_{uu} = 0.5$, and $\theta^i = 20^\circ$.

5.3.1 In-plane measurements

For in-plane measurements, $\beta^s = \gamma^s = 0$. As a result, the angle transformations given above simplify, so that $\alpha^s = \theta^i = 20^\circ$ and $\delta^s = \theta^s$. Figure 19 shows results for the in-plane comparison study. Note that the results for the CASI measurements are highly oscillatory for both the normalized scattered SD and the scattered DoP. This is most likely due to the fact the measurements contain speckle. Spinning the sample would

average out this speckle; however, the current CASI setup does not allow for continuous spinning of the sample. In addition, the CASI measurements, with respect to the normalized scattered SD, show that the Labsphere Infragold coupon does not maintain a G-G model for the underlying surface statistics. Instead, a stretched exponential-stretched exponential (SE-SE) model better characterizes the Labsphere Infragold coupon [138]. This is seen by comparing the results to a full-wave 2D MoM solution [139, 140]. Here, the analysis obtained the scattered field from 400 independent rough surface realizations simulated using the method described by Yura and Hanson [145] with both G-G and SE-SE PDFs [cf. Eq. (138)]. Before moving on in the analysis, it is important to note that the CASI measurements do not contain enough fidelity, with respect to the scattered DoP, to compare them to those obtained by the 3D vector solution.

5.3.2 Out-of-plane measurements

For the out-of-plane measurements, the CASI used the following setup parameters: $\alpha^s = 20^\circ$ and $\beta^s = 25^\circ$. Accordingly, one can use the angle transformations given above in Eqs. (199)-(205) to relate the 3D vector solution to the CASI measurements. Figure 20 shows results for the out-of-plane comparison study. Note again that the CASI measurements, with respect to the normalized scattered SD, show that the Labsphere Infragold coupon does not maintain a G-G model for the underlying surface statistics. Also note that the CASI measurements do not contain enough fidelity, with respect to the scattered DoP, to compare them to those obtained by the 3D vector solution.

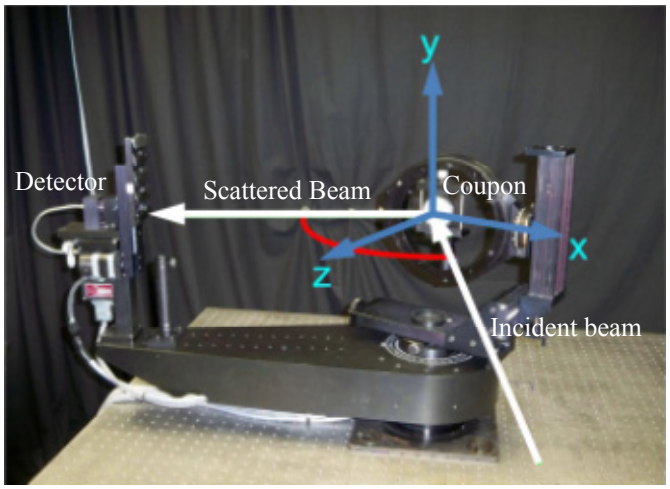

(a)

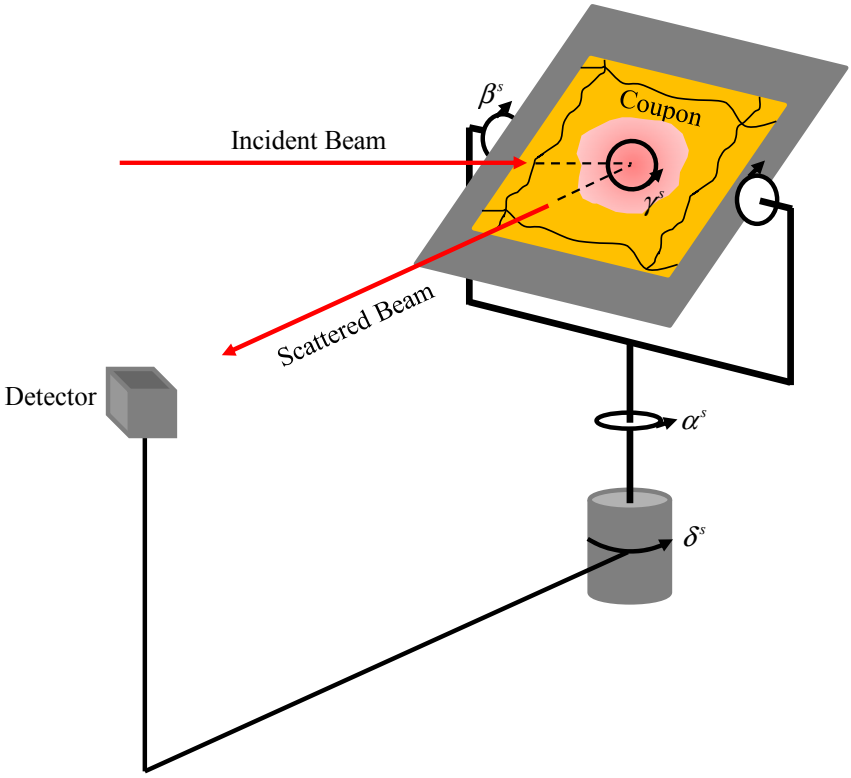

(b)

Figure 18. Description of the Complete Angle Scatter Instrument at the Air Force Institute of Technology. (a) shows the scattering geometry used to collect in-plane measurements [140], whereas (b) shows the scattering geometry used to collect out-of-plane measurements [148].

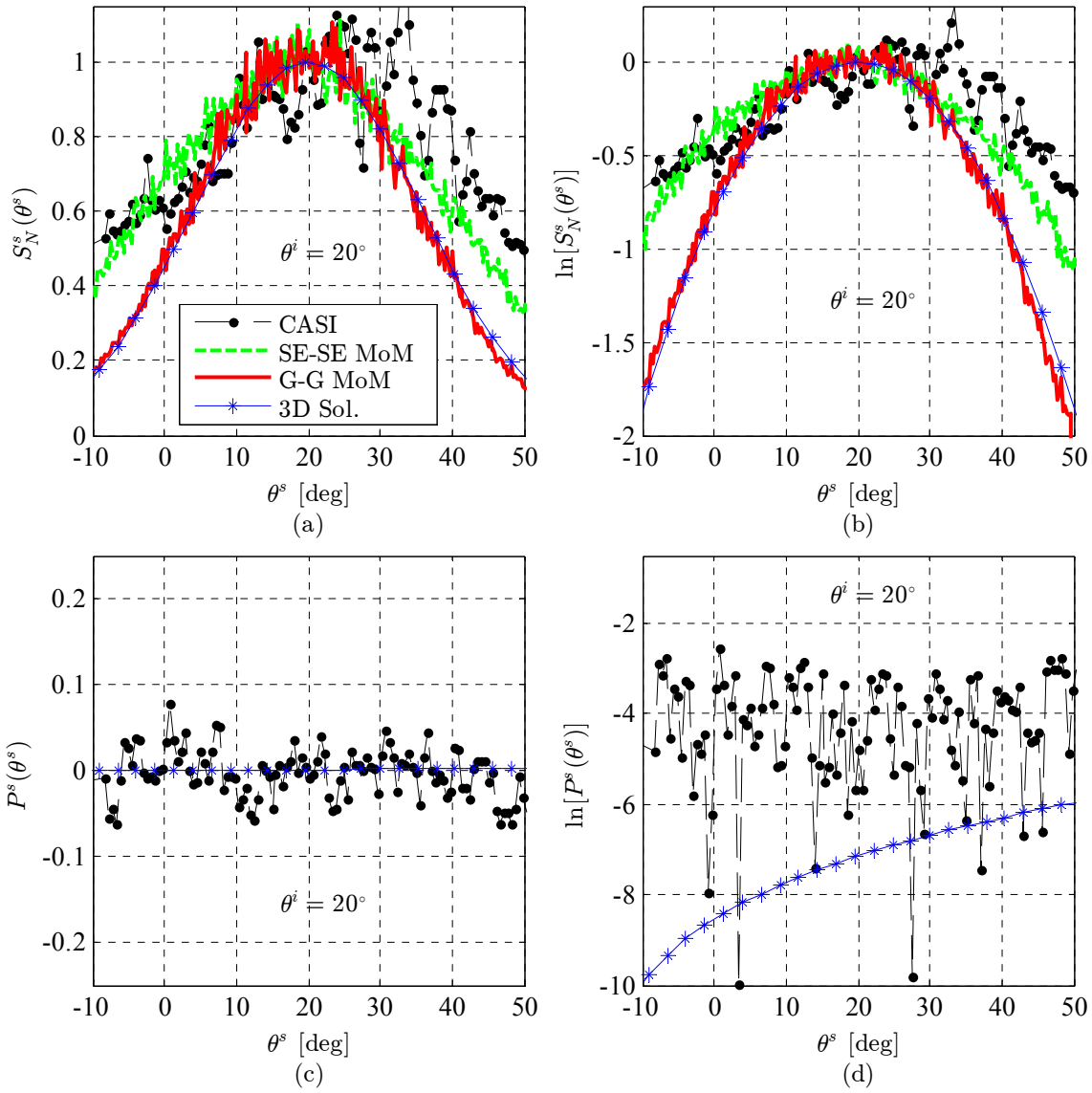

Figure 19. Comparison between in-plane measurements obtained with the Complete Angle Scatter Instrument (CASI) at the Air force Institute of Technology, a full-wave 2D method of moments (MoM) solution with two different surface models, and the 3D vector solution for unpolarized illumination at non-normal incidence of a very rough conducting surface. (a) and (c) show the normalized scattered spectral density and the scattered degree of polarization as a function of a single polar angle. (b) and (d) show the same results in log scale.

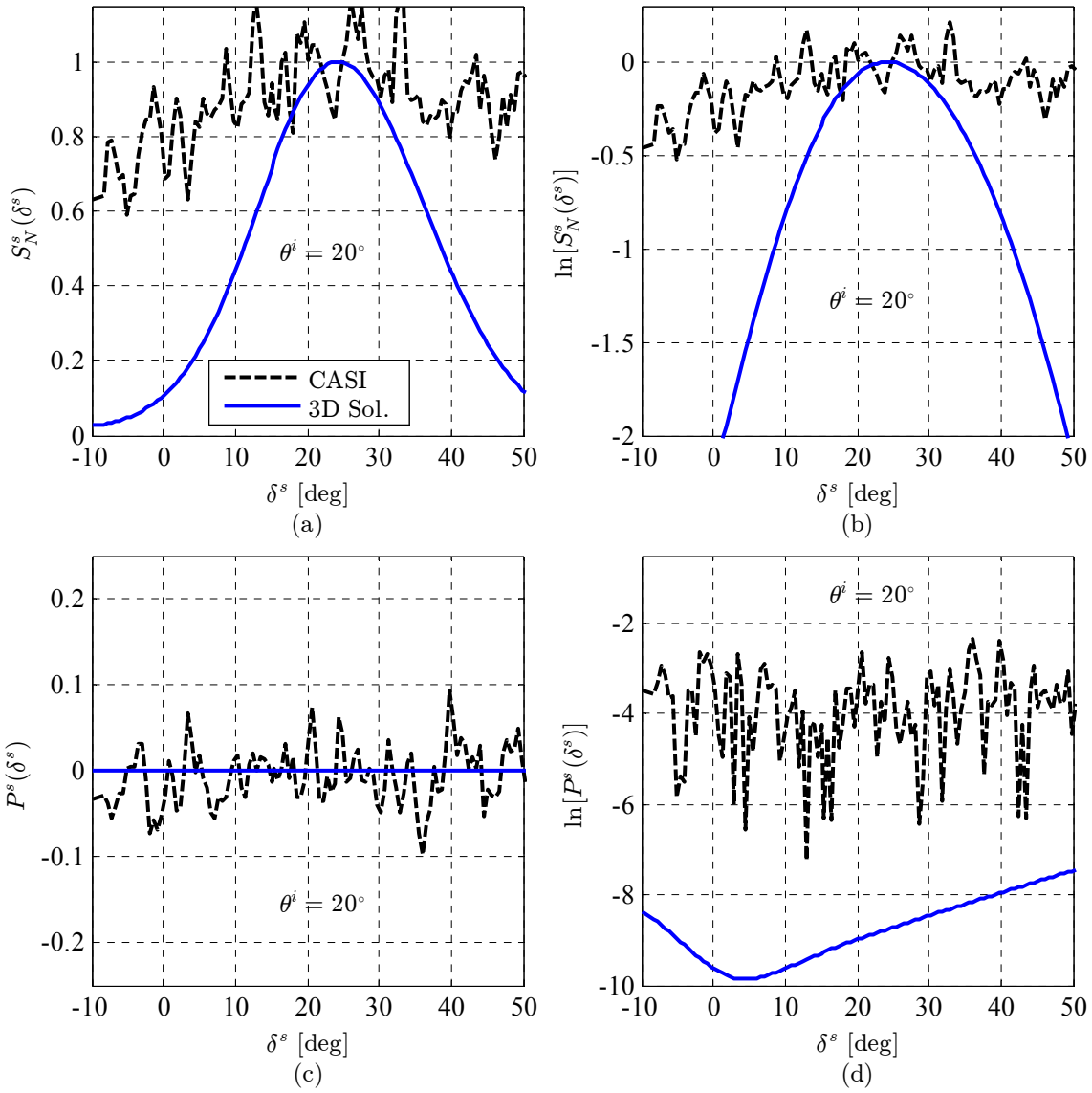

Figure 20. Comparison between out-of-plane measurements obtained with the Complete Angle Scatter Instrument (CASI) at the Air force Institute of Technology and the 3D vector solution for unpolarized illumination at non-normal incidence of a very rough conducting surface. (a) and (c) show the normalized scattered spectral density and the scattered degree of polarization as a function of a single transformation polar angle. (b) and (d) show the same results in log scale.

5.4 Comparison to a paraxial solution

An individual can analyze the 3D vector solution within a Cartesian coordinate system. With that said, one must use the following relationships:

$$\begin{gathered}\vartheta_{x1,2}=\frac{x_{1,2}}{r_{1,2}} \quad \vartheta_{y1,2}=\frac{y_{1,2}}{r_{1,2}}-\sin\left(\theta^{i}\right) \quad \vartheta_{z1,2}=\frac{z_{1,2}}{r_{1,2}}+\cos\left(\theta^{i}\right) \\ \hat{\boldsymbol{\theta}}_{1,2}\cdot\hat{\mathbf{x}}=\frac{z_{1,2}x_{1,2}}{r_{1,2}\rho_{1,2}} \quad \hat{\boldsymbol{\theta}}_{1,2}\cdot\hat{\mathbf{y}}=\frac{z_{1,2}y_{1,2}}{r_{1,2}\rho_{1,2}} \quad \hat{\boldsymbol{\theta}}_{1,2}\cdot\hat{\mathbf{z}}=-\frac{\rho_{1,2}}{r_{1,2}} \\ \hat{\boldsymbol{\phi}}_{1,2}\cdot\hat{\mathbf{x}}=-\frac{y_{1,2}}{\rho_{1,2}} \quad \hat{\boldsymbol{\phi}}_{1,2}\cdot\hat{\mathbf{y}}=\frac{x_{1,2}}{\rho_{1,2}} \\ \rho_{1,2}=\sqrt{x_{1,2}^{2}+y_{1,2}^{2}} \quad r_{1,2}=\sqrt{x_{1,2}^{2}+y_{1,2}^{2}+z_{1,2}^{2}}\end{gathered} \quad . \tag{206}$$

Provided the relationships in Eq. (206), the analysis can compare the 3D vector solution to an ABCD-matrix approach outlined by Korotkova [115]. In general, the ABCD-matrix approach describes paraxial wave propagation through any complex optical system. When modeling rough surface scattering using the ABCD-matrix approach, a phase-screen transmittance function characterizes the scattering process for very rough surface conditions. The inclusion of a soft-Gaussian aperture in the model also accounts for the size of the scattering surface and accompanying diffraction effects.

The present analysis assumes horizontally polarized (s-pol) illumination and a tactical engagement scenario, so that $A_u = B_{xu} = B_{ux} = 0$, $\lambda_0 = 1.064$ μm, $r_s = r_{1,2} = 10$ km, $w_s = 2.54/2$ cm, $\ell_{xx} = \ell_{uu} = 0.25 w_s$, and $\theta^i = 0^\circ$. This setup corresponds with partially coherent illumination at normal incidence. To ensure that incident illumination "fits" on the rough surface, the present analysis removed the soft-Gaussian aperture in the ABCD solution. In addition, the present analysis assumed an

idealized perfectly reflecting rough surface, where $\ell_h = 100\lambda_0$ and $\sigma_h = 10\lambda_0$. Such surface statistics correspond to very rough surface conditions [cf. Eq. (174)].

Provided this setup, Figure 21 shows excellent agreement between the ABCD paraxial solution and the 3D vector solution. For instance, the magnitude of the scattered SDoC (Figure 21a) shows exact agreement. The vertical line depicted here is the angular SDoC multiplied by the propagation distance to observation. Note that it correctly identifies the $1/e$ location. In addition, the normalized scattered SD shows relatively good agreement between the two solutions. The wings of the power distribution associated with the 3D vector solution tend to be wider than those associated with the ABCD solution; nonetheless, the results show good agreement out to the vertical lines depicted in Figure 21b. These vertical lines are the angular SD radius multiplied by the propagation distance to observation. Furthermore, the scattered DoP (Figure 21c) shows exact agreement between the two solutions. Based on the assumptions used within the analysis [cf. Footnote 10, p.55], no de-polarization occurs upon scattering from the perfectly reflecting rough surface [22], at least for isotropic beam parameters, i.e., when $\ell_{xx} = \ell_{uu}$ (Appendix E shows an example where this is not the case). This is also the case for p-pol illumination at normal incidence and is consistent with the 2D scalar-equivalent solution [10, 11].

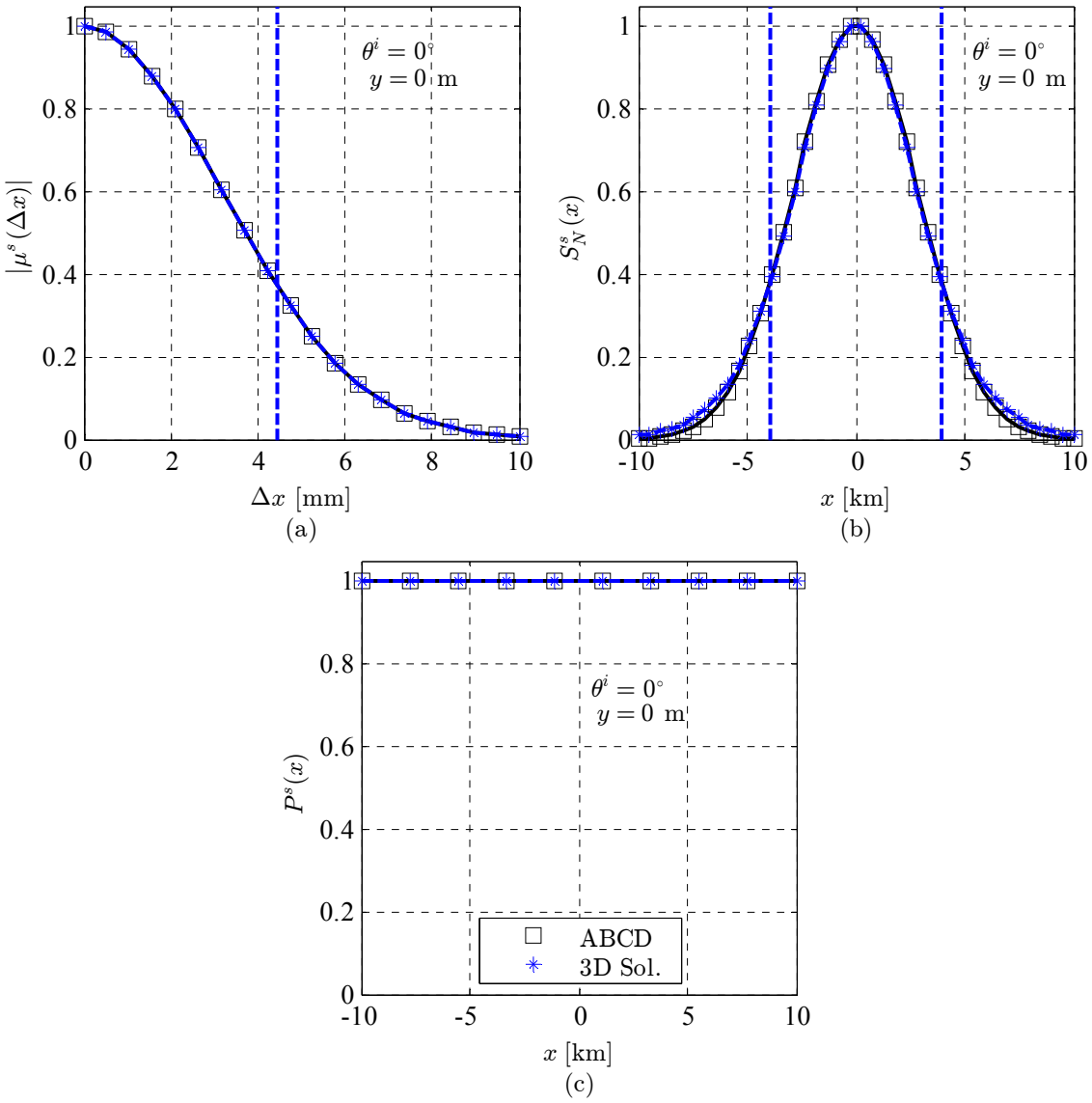

Figure 21. Comparison between an ABCD paraxial solution and the 3D vector solution for partially coherent illumination at normal incidence of a very rough perfectly reflecting surface. (a) shows the magnitude of the scattered spectral degree of coherence as a function of the distance between two values in the x direction, whereas (b) shows the scattered normalized spectral density and (c) shows the scattered degree of polarization as a function of a single value in the x direction.

6 Conclusion

This dissertation develops a 3D vector solution for the far-field scattering of spatially partially coherent electromagnetic beam illumination from statistically rough surfaces. Compared to previous research efforts, the 3D vector solution developed in this dissertation significantly extends the rough surface scattering literature, since most of the theory developed to date considers only the effects of fully coherent and fully incoherent illumination in the formation of solutions. Moreover, the analysis contained in this dissertation considers three different material substrates: dielectrics, conductors, and a perfect electrical conductor (PEC). By incorporating the effects of the material parameters within the analysis, the 3D vector solution developed here transcends previous efforts which included the effects of partially coherent beam illumination, but not the effects of the material parameters.

To develop the 3D vector solution contained in this dissertation, the analysis uses the physical optics approximation (Kirchhoff boundary conditions). It also uses a Gaussian Schell-Model (GSM) form for the incident field cross spectral density matrix (CSDM). This allows for the formulation of a closed-form expression for the scattered field CSDM. In practice, two separate analytical forms result for the scattered field CSDM. The first analytical form is applicable to smooth-to-moderately rough surfaces. It depends on an infinite series that is slowly convergent; however, one can still gain physical intuition from the resultant closed-form expression. The second analytical form is applicable to very rough surfaces. Here, the closed-form expression is extremely physical, and under certain circumstances, maintains a GSM form. This is in agreement with published results valid only in the paraxial regime.

By using the CSDM notation within the 3D vector solution, all aspects inherent in Wolf's unified theory of coherence and polarization apply here [12, 13]. Accordingly, the analysis contained in this dissertation readily formulates the spectral degree of coherence (SDoC), the spectral density (SD), and degree of polarization (DoP) to observe the coherence, size, and polarization properties of the scattered radiation in comparison to the incident radiation. The SDoC, SD, and DoP are measurable quantities in practice and serve as metrics in which to compare the 3D vector solution to previously validated solutions and empirical measurements. With this said, the analysis contained in this dissertation rigorously compares the obtained 3D vector solution to previously validated solutions and empirical measurements. The comparisons show good agreement under the appropriate conditions.

6.1 Contributions

There are two significant contributions which have already resulted from this dissertation effort (with more to come). The first is a SPIE Newsroom article which highlights the contributions of the 2D scalar-equivalent solution [10, 11] and sets the stage for the 3D vector solution developed here [8]. This article also proposes a novel experiment, which could validate the analysis contained in both the 2D and 3D solutions and is an area for future research (discussed below). The second is a 16th Annual Directed Energy Symposium proceeding which formulates the 3D vector solution for a PEC material substrate [9]. This contribution was selected for publication in both the 2013 AP-URSI and 2014 IEEE-Aerospace conferences based on abstract submission; however, due to setbacks in the federal government's budget, this publication was postponed.

6.2 Future areas of research

Future work in rough surface scattering using partially coherent illumination includes, but is not limited to, the following topics.

- Anisotropic material substrates, where the surface correlation length is directionally dependent within the analysis [43, 66].
- Partially coherent pulsed illumination that emanates from a source that is not statistically wide-sense stationary [82, 149].
- The construction of designer surfaces which control the spatial and temporal coherence properties of the scattered radiation [85, 113].
- The use of a non uniformily polarized source, where the source width is directional dependent within the analysis [101, 135].
- Surfaces with large surface slopes so that shadowing, masking, and multiple scattering effects play a role in the analysis [66, 150].
- The development of a closed-form coherent polarimetric bidirectional distribution function, which is validated using high-fidelity measurements [46, 127].
- The development of wave-optics simulations to model the spatially partially coherent beam illumination and the laser-target interaction [102, 103].
- Validation experiments which use a broadband source and narrowband filters to look at changes in the SD and DoP upon scattering off a rough surface [8, 13].

Appendix A. Using the geometrical optics approximation to relate the tangential fields at the scattering surface

Referencing the micro-scale scattering geometry given in Figure 23 [18], the law of reflection dictates that the angle of incidence equals the angle of reflection, $\theta^{inc} = \theta^{ref}$. This is a direct result from geometrical-optics (GO) approximation [22]. As such, the following relationships hold true at the closed surface *S* of a scattering object:

$$\hat{\mathbf{n}} \cdot \hat{\mathbf{k}}^{inc} = -\hat{\mathbf{n}} \cdot \hat{\mathbf{k}}^{ref}, \tag{207}$$

$$\hat{\mathbf{n}} \cdot \hat{\mathbf{k}}^{inc} = -\cos\left(\theta^{inc}\right), \tag{208}$$

$$\hat{\mathbf{n}} \cdot \hat{\mathbf{k}}^{ref} = \cos\left(\theta^{ref}\right), \tag{209}$$

$$\hat{\mathbf{n}} \times \hat{\mathbf{k}}^{inc} = \hat{\mathbf{n}} \times \hat{\mathbf{k}}^{ref}, \tag{210}$$

$$\hat{\mathbf{n}} \times \hat{\mathbf{k}}^{inc} = \hat{\mathbf{t}} \sin\left(\theta^{inc}\right), \tag{211}$$

and

$$\hat{\mathbf{n}} \times \hat{\mathbf{k}}^{ref} = \hat{\mathbf{t}} \sin\left(\theta^{ref}\right), \tag{212}$$

where $\hat{\mathbf{n}}$ is the unit normal vector, $\hat{\mathbf{k}}^{inc}$ is the unit incident propagation vector, $\hat{\mathbf{k}}^{ref}$ is the unit reflected propagation vector, and $\hat{\mathbf{t}}$ is the unit tangential vector. Provided Eqs. (207) -(212), the purpose of this appendix is to demonstrate how the tangential reflected fields, $\hat{\mathbf{n}} \times \mathbf{E}^{ref}$ and $\hat{\mathbf{n}} \times \mathbf{H}^{ref}$, relate to the tangential incident fields, $\hat{\mathbf{n}} \times \mathbf{E}^{inc}$ and $\hat{\mathbf{n}} \times \mathbf{H}^{inc}$, for different material substrates, i.e., dielectrics, conductors, and a perfect electrical conductor (PEC).

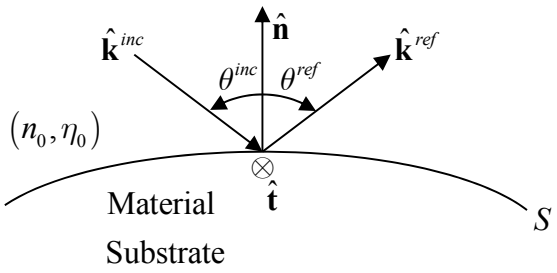

Figure 22: The micro-scale geometry describing how to relate the incident field to the reflected field using the geometrical optics approximation.

The following relationship defines the Fresnel reflection coefficient r_S at the closed surface *S*:

$$r_S = \frac{\left|\mathbf{E}^{inc}\right|}{\left|\mathbf{E}^{ref}\right|}, \tag{213}$$

so that

$$\hat{\mathbf{n}} \times \mathbf{E}^{ref} = r_S \hat{\mathbf{n}} \times \mathbf{E}^{inc} . \tag{214}$$

Equation (31) above repeats this GO result. Moreover, since [14]

$$\mathbf{E} = -\eta_0 \hat{\mathbf{k}} \times \mathbf{H} , \tag{215}$$

a similar relationship exists for the magnetic fields to that given in Eq. (214) for the electric fields. Substituting Eq. (215) into Eq. (214),

$$-\eta_0 \hat{\mathbf{n}} \times \left(\hat{\mathbf{k}}^{ref} \times \mathbf{H}^{ref} \right) = -\eta_0 r_S \hat{\mathbf{n}} \times \left(\hat{\mathbf{k}}^{inc} \times \mathbf{H}^{inc} \right) . \tag{216}$$

Furthermore, using the following vector identity:

$$\mathbf{A} \times \left(\mathbf{B} \times \mathbf{C} \right) = \mathbf{B} \left(\mathbf{A} \cdot \mathbf{C} \right) - \mathbf{C} \left(\mathbf{A} \cdot \mathbf{B} \right) \tag{217}$$

and Eqs. (207)-(212), Eq. (216) manipulates as follows:

$$
\begin{aligned}
&\Rightarrow \hat{\mathbf{k}}^{ref}\left(\hat{\mathbf{n}}\cdot\mathbf{H}^{ref}\right)-\mathbf{H}^{ref}\left(\hat{\mathbf{n}}\cdot\hat{\mathbf{k}}^{ref}\right)=r_S\hat{\mathbf{k}}^{inc}\left(\hat{\mathbf{n}}\cdot\mathbf{H}^{inc}\right)-r_S\mathbf{H}^{inc}\left(\hat{\mathbf{n}}\cdot\hat{\mathbf{k}}^{inc}\right)\\
&\Rightarrow r_S\hat{\mathbf{k}}^{ref}\left(\hat{\mathbf{n}}\cdot\mathbf{H}^{inc}\right)+\mathbf{H}^{ref}\left(\hat{\mathbf{n}}\cdot\hat{\mathbf{k}}^{inc}\right)=r_S\hat{\mathbf{k}}^{inc}\left(\hat{\mathbf{n}}\cdot\mathbf{H}^{inc}\right)-r_S\mathbf{H}^{inc}\left(\hat{\mathbf{n}}\cdot\hat{\mathbf{k}}^{inc}\right)\\
&\Rightarrow r_S\hat{\mathbf{n}}\times\hat{\mathbf{k}}^{ref}\left(\hat{\mathbf{n}}\cdot\mathbf{H}^{inc}\right)+\hat{\mathbf{n}}\times\mathbf{H}^{ref}\left(\hat{\mathbf{n}}\cdot\hat{\mathbf{k}}^{inc}\right)=r_S\hat{\mathbf{n}}\times\hat{\mathbf{k}}^{inc}\left(\hat{\mathbf{n}}\cdot\mathbf{H}^{inc}\right)-r_S\hat{\mathbf{n}}\times\mathbf{H}^{inc}\left(\hat{\mathbf{n}}\cdot\hat{\mathbf{k}}^{inc}\right)\\
&\Rightarrow r_S\hat{\mathbf{n}}\times\hat{\mathbf{k}}^{inc}\left(\hat{\mathbf{n}}\cdot\mathbf{H}^{inc}\right)+\hat{\mathbf{n}}\times\mathbf{H}^{ref}\left(\hat{\mathbf{n}}\cdot\hat{\mathbf{k}}^{inc}\right)=r_S\hat{\mathbf{n}}\times\hat{\mathbf{k}}^{inc}\left(\hat{\mathbf{n}}\cdot\mathbf{H}^{inc}\right)-r_S\hat{\mathbf{n}}\times\mathbf{H}^{inc}\left(\hat{\mathbf{n}}\cdot\hat{\mathbf{k}}^{inc}\right)
\end{aligned}
\quad .(218)
$$

From Eq. (218), it is readily apparent that

$$\hat{\mathbf{n}}\times\mathbf{H}^{ref}=-r_S\hat{\mathbf{n}}\times\mathbf{H}^{inc}. \tag{219}$$

Equation (32) above repeats this GO result.

The tangential components of the electric field equate zero along the surface of a PEC [1]. Thus, the following relationship holds true:

$$\hat{\mathbf{n}}\times\left(\mathbf{E}^{inc}+\mathbf{E}^{ref}\right)=0\Rightarrow\hat{\mathbf{n}}\times\mathbf{E}^{inc}=-\hat{\mathbf{n}}\times\mathbf{E}^{ref}. \tag{220}$$

Equation (37) above repeats this GO result. Substituting Eq. (215) into Eq. (220),

$$\eta_0\hat{\mathbf{n}}\times\left(\hat{\mathbf{k}}^{inc}\times\mathbf{H}^{inc}\right)=-\eta_0\hat{\mathbf{n}}\times\left(\hat{\mathbf{k}}^{ref}\times\mathbf{H}^{ref}\right). \tag{221}$$

Additionally, using Eq. (217) and Eqs. (207)-(212), Eq. (221) manipulates as follows:

$$
\begin{aligned}
&\Rightarrow \hat{\mathbf{k}}^{inc}\left(\hat{\mathbf{n}}\cdot\mathbf{H}^{inc}\right)-\mathbf{H}^{inc}\left(\hat{\mathbf{n}}\cdot\hat{\mathbf{k}}^{inc}\right)=-\left[\hat{\mathbf{k}}^{ref}\left(\hat{\mathbf{n}}\cdot\mathbf{H}^{ref}\right)-\mathbf{H}^{ref}\left(\hat{\mathbf{n}}\cdot\hat{\mathbf{k}}^{ref}\right)\right]\\
&\Rightarrow \hat{\mathbf{k}}^{inc}\left(\hat{\mathbf{n}}\cdot\mathbf{H}^{ref}\right)-\mathbf{H}^{inc}\left(\hat{\mathbf{n}}\cdot\hat{\mathbf{k}}^{ref}\right)=\hat{\mathbf{k}}^{ref}\left(\hat{\mathbf{n}}\cdot\mathbf{H}^{ref}\right)-\mathbf{H}^{ref}\left(\hat{\mathbf{n}}\cdot\hat{\mathbf{k}}^{ref}\right)\\
&\Rightarrow \hat{\mathbf{n}}\times\hat{\mathbf{k}}^{inc}\left(\hat{\mathbf{n}}\cdot\mathbf{H}^{ref}\right)-\hat{\mathbf{n}}\times\mathbf{H}^{inc}\left(\hat{\mathbf{n}}\cdot\hat{\mathbf{k}}^{ref}\right)=\hat{\mathbf{n}}\times\hat{\mathbf{k}}^{ref}\left(\hat{\mathbf{n}}\cdot\mathbf{H}^{ref}\right)-\hat{\mathbf{n}}\times\mathbf{H}^{ref}\left(\hat{\mathbf{n}}\cdot\hat{\mathbf{k}}^{ref}\right)\\
&\Rightarrow \hat{\mathbf{n}}\times\hat{\mathbf{k}}^{ref}\left(\hat{\mathbf{n}}\cdot\mathbf{H}^{ref}\right)-\hat{\mathbf{n}}\times\mathbf{H}^{inc}\left(\hat{\mathbf{n}}\cdot\hat{\mathbf{k}}^{ref}\right)=\hat{\mathbf{n}}\times\hat{\mathbf{k}}^{ref}\left(\hat{\mathbf{n}}\cdot\mathbf{H}^{ref}\right)-\hat{\mathbf{n}}\times\mathbf{H}^{ref}\left(\hat{\mathbf{n}}\cdot\hat{\mathbf{k}}^{ref}\right)
\end{aligned}
\quad . \tag{222}
$$

From Eq. (222), it is readily apparent that

$$\hat{\mathbf{n}}\times\mathbf{H}^{ref}=\hat{\mathbf{n}}\times\mathbf{H}^{inc}. \tag{223}$$

Equation (38) above repeats this GO result.

Appendix B. Using the physical optics approximation to simplify the equivalent surface current densities

The physical-optics (PO) approximation uses the geometrical-optics (GO) approximation to formulate the current densities involved in an electromagnetic scattering problem. With that said, the purpose of this appendix is to demonstrate how the equivalent surface current densities, which result from using surface equivalence, simplify to known quantities when using the GO approximation in association with the PO approximation.

To make this concept manifest, first consider the micro-scale scattering geometry given in Figure 23. Here, the law of reflection dictates that the angle of incidence equals the angle of reflection, $\theta^{inc} = \theta^{ref}$. This is a direct result from the GO approximation [22]. In using the GO approximation as part of the PO approximation, one must assume that the scattering object and its associated surface curvature are large compared to the wavelength of the incident fields. Such approximations are exact when the scattering surface is homogeneous, infinite, and planar [14, 22]. As such, when using the PO approximation, the following relationships hold true at the closed surface *S* of a scattering object:

$$\hat{\mathbf{s}} = \frac{\hat{\mathbf{k}}^{inc} \times \hat{\mathbf{n}}}{\left|\hat{\mathbf{k}}^{inc} \times \hat{\mathbf{n}}\right|} \quad \hat{\mathbf{s}} = \hat{\mathbf{k}}^{inc} \times \hat{\mathbf{p}} \quad -\hat{\mathbf{s}} = \hat{\mathbf{k}}^{ref} \times \hat{\mathbf{p}}^{ref}\,, \tag{224}$$

$$\hat{\mathbf{p}} = \hat{\mathbf{s}} \times \hat{\mathbf{k}}^{inc} \quad -\hat{\mathbf{p}} = \hat{\mathbf{k}}^{inc} \times \hat{\mathbf{s}}\,, \tag{225}$$

$$\hat{\mathbf{p}}^{ref} = -\hat{\mathbf{s}} \times \hat{\mathbf{k}}^{ref} \quad \hat{\mathbf{p}}^{ref} = \hat{\mathbf{k}}^{ref} \times \hat{\mathbf{s}}\,, \tag{226}$$

and

$$-\hat{\mathbf{n}} \cdot \hat{\mathbf{k}}^{inc} = \hat{\mathbf{n}} \cdot \hat{\mathbf{k}}^{ref}\,, \tag{227}$$

where $\hat{\mathbf{s}}$ is the unit perpendicular vector, $\hat{\mathbf{p}}$ is the unit parallel vector, $\hat{\mathbf{p}}^{ref}$ is the unit parallel vector upon reflection, $\hat{\mathbf{n}}$ is the unit normal vector, $\hat{\mathbf{k}}^{inc}$ is the unit incident propagation vector, and $\hat{\mathbf{k}}^{ref}$ is the unit reflected propagation vector. Provided Eqs. (224) -(227), one can then write the equivalent surface current densities, $\mathbf{J}_S^{eq}$ and $\mathbf{M}_S^{eq}$, in terms of only the known incident electric field $\mathbf{E}^{inc}$. This is shown in the analysis to follow.

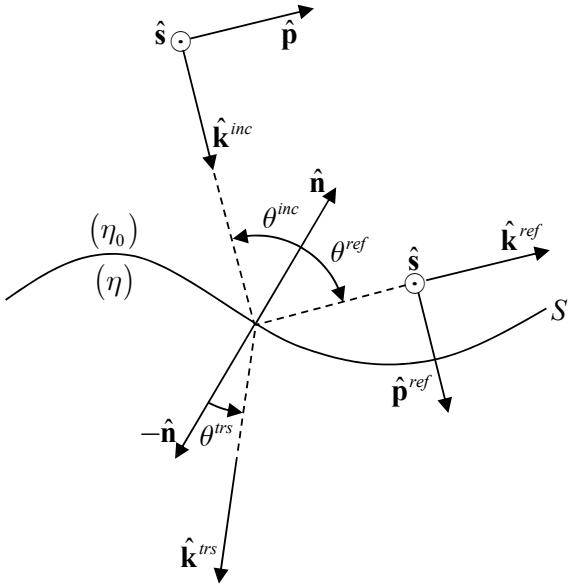

Figure 23: The micro-scale geometry describing how to relate the incident field to the reflected and transmitted fields using the geometrical optics approximation.

As stated in Section 2.3, when using the PO approximation with surface equivalence, one replaces the unknown scattered fields with reflected fields. In particular, $\mathbf{E}^{sct} \approx \mathbf{E}^{ref}$ and $\mathbf{H}^{sct} \approx \mathbf{H}^{ref}$, so that the equivalent surface current densities, $\mathbf{J}_S^{eq}$ and $\mathbf{M}_S^{eq}$, become

$$\mathbf{J}_S^{eq} = \hat{\mathbf{n}} \times \mathbf{H}^{ext} = \hat{\mathbf{n}} \times \left(\mathbf{H}^{inc} + \mathbf{H}^{sct} \right) \approx \hat{\mathbf{n}} \times \left(\mathbf{H}^{inc} + \mathbf{H}^{ref} \right) \tag{228}$$

and

$$\mathbf{M}_S^{eq} = -\hat{\mathbf{n}} \times \mathbf{E}^{ext} = -\hat{\mathbf{n}} \times \left(\mathbf{E}^{inc} + \mathbf{E}^{sct} \right) \approx -\hat{\mathbf{n}} \times \left(\mathbf{E}^{inc} + \mathbf{E}^{ref} \right). \tag{229}$$

Moreover, in using the following relationship [14]:

$$\mathbf{H} = \frac{1}{\eta_0}\hat{\mathbf{k}} \times \mathbf{E} \tag{230}$$

and writing the respective electric fields in terms of their perpendicular and parallel components, i.e.,

$$\mathbf{E} = \left(\hat{\mathbf{s}}\hat{\mathbf{s}} + \hat{\mathbf{p}}\hat{\mathbf{p}}\right) \cdot \mathbf{E}\,, \tag{231}$$

the equivalent surface current densities, $\mathbf{J}_S^{eq}$ and $\mathbf{M}_S^{eq}$, become

$$\mathbf{J}_S^{eq} = \frac{1}{\eta_0}\hat{\mathbf{n}} \times \left[\hat{\mathbf{k}}^{inc} \times \left(\hat{\mathbf{s}}\hat{\mathbf{s}} + \hat{\mathbf{p}}\hat{\mathbf{p}}\right) \cdot \mathbf{E}^{inc} + \hat{\mathbf{k}}^{ref}\left(\hat{\mathbf{s}}\hat{\mathbf{s}} + \hat{\mathbf{p}}^{ref}\hat{\mathbf{p}}^{ref}\right) \cdot \mathbf{E}^{ref}\right] \tag{232}$$

and

$$\mathbf{M}_S^{eq} = -\hat{\mathbf{n}} \times \left[\left(\hat{\mathbf{s}}\hat{\mathbf{s}} + \hat{\mathbf{p}}\hat{\mathbf{p}}\right) \cdot \mathbf{E}^{inc} + \left(\hat{\mathbf{s}}\hat{\mathbf{s}} + \hat{\mathbf{p}}^{ref}\hat{\mathbf{p}}^{ref}\right) \cdot \mathbf{E}^{ref}\right]. \tag{233}$$

Defining the perpendicular and parallel Fresnel reflection coefficients as

$$r_\perp = \frac{\hat{\mathbf{s}} \cdot \mathbf{E}^{ref}}{\hat{\mathbf{s}} \cdot \mathbf{E}^{inc}} = \frac{\eta \cos\left(\theta^{inc}\right) - \eta_0 \cos\left(\theta^{trs}\right)}{\eta \cos\left(\theta^{inc}\right) - \eta_0 \cos\left(\theta^{trs}\right)} \tag{234}$$

and

$$r_\parallel = \frac{\hat{\mathbf{p}}^{ref} \cdot \mathbf{E}^{ref}}{\hat{\mathbf{p}} \cdot \mathbf{E}^{inc}} = \frac{-\eta_0 \cos\left(\theta^{inc}\right) + \eta \cos\left(\theta^{trs}\right)}{\eta_0 \cos\left(\theta^{inc}\right) + \eta \cos\left(\theta^{trs}\right)}, \tag{235}$$

where θ^{trs} is the angle of transmission, η_0 is the impedance of free-space, and η is the impedance of the material substrate (cf. Figure 23), one can then write the equivalent surface current densities, $\mathbf{J}_S^{eq}$ and $\mathbf{M}_S^{eq}$, in terms of only the known incident electric field $\mathbf{E}^{inc}$. Specifically,

$$\mathbf{J}_S^{eq} = \frac{1}{\eta_0}\hat{\mathbf{n}} \times \left[\mathbf{k}^{inc} \times \left(\hat{\mathbf{s}}\hat{\mathbf{s}} + \hat{\mathbf{p}}\hat{\mathbf{p}}\right) + \mathbf{k}^{ref} \times \left(\hat{\mathbf{s}} r_\perp \hat{\mathbf{s}} + \hat{\mathbf{p}}^{ref} r_\parallel \hat{\mathbf{p}}\right)\right] \cdot \mathbf{E}^{inc} \tag{236}$$

and

$$\mathbf{M}_S^{eq} = -\hat{\mathbf{n}} \times \left[\left(\hat{\mathbf{s}}\hat{\mathbf{s}} + \hat{\mathbf{p}}\hat{\mathbf{p}}\right) + \left(\hat{\mathbf{s}} r_\perp \hat{\mathbf{s}} + \hat{\mathbf{p}}^{ref} r_\parallel \hat{\mathbf{p}}\right)\right] \cdot \mathbf{E}^{inc}. \tag{237}$$

Before moving on in the analysis, it is important to note that the Fresnel reflection coefficients, as defined in Eqs. (234) and (235), are readily derived throughout the electromagnetic and optics literature. Balanis' treatment is particularly insightful [14], as his problem setup directly relates to that used in Figure 23.

Using the relationships found in Eqs. (224)-(227), the equivalent surface current densities, $\mathbf{J}_S^{eq}$ and $\mathbf{M}_S^{eq}$, as given in Eqs. (236) and (237), simplify even further, such that

$$\begin{aligned}\mathbf{J}_S^{eq} &= \frac{1}{\eta_0}\hat{\mathbf{n}}\times\left[\mathbf{k}^{inc}\times\left(\hat{\mathbf{s}}\hat{\mathbf{s}}+\hat{\mathbf{p}}\hat{\mathbf{p}}\right)+\mathbf{k}^{ref}\times\left(\hat{\mathbf{s}}r_{\perp}\hat{\mathbf{s}}+\hat{\mathbf{p}}^{ref}r_{\parallel}\hat{\mathbf{p}}\right)\right]\cdot\mathbf{E}^{inc}\\ &= \frac{1}{\eta_0}\hat{\mathbf{n}}\times\left[\hat{\mathbf{s}}\hat{\mathbf{p}}-\hat{\mathbf{p}}\hat{\mathbf{s}}+\hat{\mathbf{p}}^{ref}r_{\perp}\hat{\mathbf{s}}-\hat{\mathbf{s}}r_{\parallel}\hat{\mathbf{p}}\right]\cdot\mathbf{E}^{inc}\\ &= \frac{1}{\eta_0}\hat{\mathbf{n}}\times\left[\hat{\mathbf{s}}\left(1-r_{\parallel}\right)\hat{\mathbf{p}}-\left(\hat{\mathbf{p}}-\hat{\mathbf{p}}^{ref}r_{\perp}\right)\hat{\mathbf{s}}\right]\cdot\mathbf{E}^{inc}\\ &= \frac{1}{\eta_0}\left[\hat{\mathbf{n}}\times\hat{\mathbf{s}}\left(1-r_{\parallel}\right)\hat{\mathbf{p}}-\left(\hat{\mathbf{n}}\times\hat{\mathbf{s}}\times\hat{\mathbf{k}}^{inc}-\hat{\mathbf{n}}\times-\hat{\mathbf{s}}\times\hat{\mathbf{k}}^{ref}r_{\perp}\right)\hat{\mathbf{s}}\right]\cdot\mathbf{E}^{inc}\end{aligned} \tag{238}$$

and

$$\begin{aligned}\mathbf{M}_S^{eq} &= -\hat{\mathbf{n}}\times\left[\hat{\mathbf{s}}\hat{\mathbf{s}}+\hat{\mathbf{p}}\hat{\mathbf{p}}+\hat{\mathbf{s}}r_{\perp}\hat{\mathbf{s}}+\hat{\mathbf{p}}^{ref}r_{\parallel}\hat{\mathbf{p}}\right]\cdot\mathbf{E}^{inc}\\ &= -\hat{\mathbf{n}}\times\left[\hat{\mathbf{s}}\left(1+r_{\perp}\right)\hat{\mathbf{s}}+\left(\hat{\mathbf{p}}+\hat{\mathbf{p}}^{ref}r_{\parallel}\right)\hat{\mathbf{p}}\right]\cdot\mathbf{E}^{inc}\\ &= -\left[\hat{\mathbf{n}}\times\hat{\mathbf{s}}\left(1+r_{\perp}\right)\hat{\mathbf{s}}+\left(\hat{\mathbf{n}}\times\hat{\mathbf{p}}+\hat{\mathbf{n}}\times\hat{\mathbf{p}}^{ref}r_{\parallel}\right)\hat{\mathbf{p}}\right]\cdot\mathbf{E}^{inc}\end{aligned}. \tag{239}$$

Furthermore, using the following vector identity:

$$\mathbf{A}\times\left(\mathbf{B}\times\mathbf{C}\right)=\mathbf{B}\left(\mathbf{A}\cdot\mathbf{C}\right)-\mathbf{C}\left(\mathbf{A}\cdot\mathbf{B}\right), \tag{240}$$

one can then write the equivalent surface current densities, $\mathbf{J}_S^{eq}$ and $\mathbf{M}_S^{eq}$, in terms of the dyadics, $\vec{\mathbf{J}}_S^{eq}$ and $\vec{\mathbf{M}}_S^{eq}$, where

$$
\begin{aligned}
\mathbf{J}_S^{eq} &= \frac{1}{\eta_0}\left[\hat{\mathbf{n}}\times\hat{\mathbf{s}}\left(1-r_{\parallel}\right)\hat{\mathbf{p}} - \left(\hat{\mathbf{n}}\times\hat{\mathbf{s}}\times\hat{\mathbf{k}}^{inc} - \hat{\mathbf{n}}\times -\hat{\mathbf{s}}\times\hat{\mathbf{k}}^{ref} r_{\perp}\right)\hat{\mathbf{s}}\right]\cdot\mathbf{E}^{inc} \\
&= \frac{1}{\eta_0}\left(\hat{\mathbf{n}}\times\hat{\mathbf{s}}\left(1-r_{\parallel}\right)\hat{\mathbf{p}} - \left[\hat{\mathbf{s}}\left(\hat{\mathbf{n}}\cdot\hat{\mathbf{k}}^{inc}\right) + \hat{\mathbf{s}}\left(\hat{\mathbf{n}}\cdot\hat{\mathbf{k}}^{ref}\right) r_{\perp}\right]\hat{\mathbf{s}}\right)\cdot\mathbf{E}^{inc}, \quad \text{since } \hat{\mathbf{n}}\cdot\hat{\mathbf{s}} = 0 \\
&= \frac{1}{\eta_0}\left(\hat{\mathbf{n}}\times\hat{\mathbf{s}}\left(1-r_{\parallel}\right)\hat{\mathbf{p}} - \left[\hat{\mathbf{s}}\left(\hat{\mathbf{n}}\cdot\hat{\mathbf{k}}^{inc}\right) - \hat{\mathbf{s}}\left(\hat{\mathbf{n}}\cdot\hat{\mathbf{k}}^{inc}\right) r_{\perp}\right]\hat{\mathbf{s}}\right)\cdot\mathbf{E}^{inc} \\
&= \frac{1}{\eta_0}\left[\hat{\mathbf{n}}\times\hat{\mathbf{s}}\left(1-r_{\parallel}\right)\hat{\mathbf{p}} - \hat{\mathbf{s}}\left(\hat{\mathbf{n}}\cdot\hat{\mathbf{k}}^{inc}\right)\left(1-r_{\perp}\right)\hat{\mathbf{s}}\right]\cdot\mathbf{E}^{inc} \\
&= \frac{1}{\eta_0}\hat{\mathbf{n}}\times\left[\hat{\mathbf{s}}\left(1-r_{\parallel}\right)\hat{\mathbf{p}} - \hat{\mathbf{s}}\times\hat{\mathbf{k}}^{inc}\left(1-r_{\perp}\right)\hat{\mathbf{s}}\right]\cdot\mathbf{E}^{inc} \\
&= \frac{1}{\eta_0}\hat{\mathbf{n}}\times\left[\hat{\mathbf{s}}\left(1-r_{\parallel}\right)\hat{\mathbf{p}} - \hat{\mathbf{p}}\left(1-r_{\perp}\right)\hat{\mathbf{s}}\right]\cdot\mathbf{E}^{inc} \\
&= \frac{1}{\eta_0}\ddot{\mathbf{J}}_S^{eq}\cdot\mathbf{E}^{inc}
\end{aligned}
\tag{241}
$$

and

$$
\begin{aligned}
\mathbf{M}_S^{eq} &= -\left[\hat{\mathbf{n}}\times\hat{\mathbf{s}}\left(1+r_{\perp}\right)\hat{\mathbf{s}} + \left(\hat{\mathbf{n}}\times\hat{\mathbf{p}} + \hat{\mathbf{n}}\times\hat{\mathbf{p}}^{ref} r_{\parallel}\right)\hat{\mathbf{p}}\right]\cdot\mathbf{E}^{inc} \\
&= -\left[\hat{\mathbf{n}}\times\hat{\mathbf{s}}\left(1+r_{\perp}\right)\hat{\mathbf{s}} + \left(\hat{\mathbf{n}}\times\hat{\mathbf{s}}\times\hat{\mathbf{k}}^{inc} + \hat{\mathbf{n}}\times -\hat{\mathbf{s}}\times\hat{\mathbf{k}}^{ref} r_{\parallel}\right)\hat{\mathbf{p}}\right]\cdot\mathbf{E}^{inc} \\
&= -\left(\hat{\mathbf{n}}\times\hat{\mathbf{s}}\left(1+r_{\perp}\right)\hat{\mathbf{s}} + \left[\hat{\mathbf{s}}\left(\hat{\mathbf{n}}\cdot\hat{\mathbf{k}}^{inc}\right) - \hat{\mathbf{s}}\left(\hat{\mathbf{n}}\cdot\hat{\mathbf{k}}^{ref}\right) r_{\parallel}\hat{\mathbf{p}}\right]\right)\cdot\mathbf{E}^{inc}, \quad \text{since } \hat{\mathbf{n}}\cdot\hat{\mathbf{s}} = 0 \\
&= -\left(\hat{\mathbf{n}}\times\hat{\mathbf{s}}\left(1+r_{\perp}\right)\hat{\mathbf{s}} + \left[\hat{\mathbf{s}}\left(\hat{\mathbf{n}}\cdot\hat{\mathbf{k}}^{inc}\right) + \hat{\mathbf{s}}\left(\hat{\mathbf{n}}\cdot\hat{\mathbf{k}}^{inc}\right) r_{\parallel}\hat{\mathbf{p}}\right]\right)\cdot\mathbf{E}^{inc} \\
&= -\left[\hat{\mathbf{n}}\times\hat{\mathbf{s}}\left(1+r_{\perp}\right)\hat{\mathbf{s}} + \hat{\mathbf{s}}\left(\hat{\mathbf{n}}\cdot\hat{\mathbf{k}}^{inc}\right)\left(1+r_{\parallel}\right)\hat{\mathbf{p}}\right]\cdot\mathbf{E}^{inc} \\
&= -\hat{\mathbf{n}}\times\left[\hat{\mathbf{s}}\left(1+r_{\perp}\right)\hat{\mathbf{s}} + \hat{\mathbf{s}}\times\hat{\mathbf{k}}^{inc}\left(1+r_{\parallel}\right)\hat{\mathbf{p}}\right]\cdot\mathbf{E}^{inc} \\
&= -\hat{\mathbf{n}}\times\left[\hat{\mathbf{s}}\left(1+r_{\perp}\right)\hat{\mathbf{s}} + \hat{\mathbf{p}}\left(1+r_{\parallel}\right)\hat{\mathbf{p}}\right]\cdot\mathbf{E}^{inc} \\
&= -\ddot{\mathbf{M}}_S^{eq}\cdot\mathbf{E}^{inc}
\end{aligned}
\tag{242}
$$

.

Equations (115)-(118) above repeat these PO results.

Appendix C. Using the method of stationary phase to solve the integrals with respect to the plane-wave spectrum representation

The plane-wave spectrum representation often results in rather complex integral expressions. In practice, one must employ mathematical techniques, such as the method of stationary phase (MoSP), to solve these complex integral expressions. The purpose of this appendix is to demonstrate how one uses the MoSP to reduce the integrals with respect the plane-wave spectrum representation into closed-form expressions.

Within the analysis given above, the plane-wave spectrum representation results in integral expressions which take the following form [cf. Eqs. (141)-(144)]:

$$\mathcal{I} = \int_{-\infty}^{\infty}\int_{-\infty}^{\infty}\int_{-\infty}^{\infty}\int_{-\infty}^{\infty} \vec{\vec{\mathbf{f}}}\, \mathrm{e}^{jk_0 g}\, dk_{x1}^{i} dk_{x2}^{i} dk_{u1}^{i} dk_{u2}^{i}\,, \tag{243}$$

where $\vec{\vec{\mathbf{f}}} = \vec{\vec{\mathbf{f}}}\left(k_{x1}^{i}, k_{x2}^{i}, k_{u1}^{i}, k_{u2}^{i}; x_1', x_2', y_1', y_2'\right)$ is a representative amplitude dyadic that contains all of the amplitude terms and $g = g\left(k_{x1}^{i}, k_{x2}^{i}, k_{u1}^{i}, k_{u2}^{i}; x_1', x_2', y_1', y_2'\right)$ is a phase function that contains all of the phase terms. In using the MoSP (cf. Section 2.4.3), Eq. (243) simplifies into the following closed-form expression:

$$\mathcal{I} = \left(\frac{2\pi}{k_0}\right)^2 \frac{\vec{\vec{\mathbf{f}}}_0}{\left|\mathrm{Det}\left\{\partial^2 g_0\right\}\right|^{1/2}} \exp\left[jk_0 g_0\right] \exp\left(j\frac{\pi}{4}\mathrm{sgn}\left\{\partial^2 g_0\right\}\right) \tag{244}$$

where $\vec{\vec{\mathbf{f}}}_0$ and g_0 are the amplitude dyadic and phase function evaluated at the critical points of the first kind, respectively. In general,

$$\partial^2 g = \begin{bmatrix} \dfrac{\partial^2 g}{\partial\left(k_{x1}^i\right)^2} & \dfrac{\partial^2 g}{\partial k_{x1}^i \partial k_{x2}^i} & \dfrac{\partial^2 g}{\partial k_{x1}^i \partial k_{u1}^i} & \dfrac{\partial^2 g}{\partial k_{x1}^i \partial k_{u2}^i} \\ \dfrac{\partial^2 g}{\partial k_{x2}^i \partial k_{x1}^i} & \dfrac{\partial^2 g}{\partial\left(k_{x2}^i\right)^2} & \dfrac{\partial^2 g}{\partial k_{x2}^i \partial k_{u1}^i} & \dfrac{\partial^2 g}{\partial k_{x2}^i \partial k_{u2}^i} \\ \dfrac{\partial^2 g}{\partial k_{u1}^i \partial k_{x1}^i} & \dfrac{\partial^2 g}{\partial k_{u1}^i \partial k_{x2}^i} & \dfrac{\partial^2 g}{\partial\left(k_{u1}^i\right)^2} & \dfrac{\partial^2 g}{\partial k_{u1}^i \partial k_{u2}^i} \\ \dfrac{\partial^2 g}{\partial k_{u2}^i \partial k_{x1}^i} & \dfrac{\partial^2 g}{\partial k_{u2}^i \partial k_{x2}^i} & \dfrac{\partial^2 g}{\partial k_{u2}^i \partial k_{u1}^i} & \dfrac{\partial^2 g}{\partial\left(k_{u2}^i\right)^2} \end{bmatrix}, \tag{245}$$

so that $\partial^2 g_0$ is a real symmetric non-degenerate matrix which is also evaluated at the critical points of the first kind. To determine the critical points of the first kind, one must first account for the phase function g.

In the analysis given above, the following common phase function results [cf. Eq. (149)]:

$$\begin{aligned} g = &\left[r_s + \left(\hat{\mathbf{y}}\cdot\hat{\mathbf{v}}\right) y_2'\right] k_{v2}^i - \left[r_s + \left(\hat{\mathbf{y}}\cdot\hat{\mathbf{v}}\right) y_1'\right] k_{v1}^i \\ &+ \frac{1}{k_0}\left(x_2' k_{x2}^i - x_1' k_{x1}^i\right) + \frac{\left(\hat{\mathbf{y}}\cdot\hat{\mathbf{u}}\right)}{k_0}\left(y_2' k_{u2}^i - y_1' k_{u1}^i\right), \\ &+ \left(\hat{\mathbf{x}}\cdot\hat{\mathbf{r}}_1 x_1' - \hat{\mathbf{x}}\cdot\hat{\mathbf{r}}_2 x_2'\right) + \left(\hat{\mathbf{y}}\cdot\hat{\mathbf{r}}_1 y_1' - \hat{\mathbf{y}}\cdot\hat{\mathbf{r}}_2 y_2'\right) \end{aligned} \tag{246}$$

where $$k_{v1,2}^i = \sqrt{k_0^2 - \left(k_{x1,2}^i\right)^2 - \left(k_{u1,2}^i\right)^2} = k_0^2\sqrt{1 - \left(\frac{k_{x1,2}^i}{k_0}\right)^2 - \left(\frac{k_{u1,2}^i}{k_0}\right)^2}\,. \tag{247}$$

Provided Eq. (246), one then computes the following first-order partial derivatives:

$$\frac{\partial g}{\partial k_{x1}^i} = -\frac{x_1'}{k_0} + \frac{k_{x1}^i\left[r_s + \left(\hat{\mathbf{y}}\cdot\hat{\mathbf{v}}\right) y_1'\right]}{k_0^2\sqrt{1 - \left(\frac{k_{x1}^i}{k_0}\right)^2 - \left(\frac{k_{u1}^i}{k_0}\right)^2}}, \tag{248}$$

$$\frac{\partial g}{\partial k_{x2}^i} = \frac{x_2'}{k_0} - \frac{k_{x2}^i \left[r_s + \left(\hat{\mathbf{y}} \cdot \hat{\mathbf{v}} \right) y_2' \right]}{k_0^2 \sqrt{1 - \left(\frac{k_{x2}^i}{k_0} \right)^2 - \left(\frac{k_{u2}^i}{k_0} \right)^2}}, \tag{249}$$

$$\frac{\partial g}{\partial k_{u1}^i} = -\frac{\left(\hat{\mathbf{y}} \cdot \hat{\mathbf{u}} \right) y_1'}{k_0} + \frac{k_{u1}^i \left[r_s + \left(\hat{\mathbf{y}} \cdot \hat{\mathbf{v}} \right) y_1' \right]}{k_0^2 \sqrt{1 - \left(\frac{k_{x1}^i}{k_0} \right)^2 - \left(\frac{k_{u1}^i}{k_0} \right)^2}}, \tag{250}$$

and

$$\frac{\partial g}{\partial k_{u2}^i} = \frac{\left(\hat{\mathbf{y}} \cdot \hat{\mathbf{u}} \right) y_2'}{k_0} - \frac{k_{u2}^i \left[r_s + \left(\hat{\mathbf{y}} \cdot \hat{\mathbf{v}} \right) y_2' \right]}{k_0^2 \sqrt{1 - \left(\frac{k_{x2}^i}{k_0} \right)^2 - \left(\frac{k_{u2}^i}{k_0} \right)^2}}. \tag{251}$$

By setting Eqs. (248)-(251) equal to zero and solving for $k_{x1,2}^i$ and $k_{u1,2}^i$, one then obtains four equations and four unknowns. Specifically,

$$\frac{\partial g}{\partial k_{x1,2}^i} = 0 \Rightarrow k_{x1,2}^i = \pm \frac{x_{1,2}' \sqrt{k_0^2 - \left(k_{u1,2}^i \right)^2}}{\sqrt{r_s^2 + x_{1,2}'^2 + \left(\hat{\mathbf{y}} \cdot \hat{\mathbf{v}} \right)^2 y_{1,2}'^2 + 2 r_s \left(\hat{\mathbf{y}} \cdot \hat{\mathbf{v}} \right) y_{1,2}'}} \tag{252}$$

and

$$\frac{\partial g}{\partial k_{u1,2}^i} = 0 \Rightarrow k_{u1,2}^i = \pm \frac{\left(\hat{\mathbf{y}} \cdot \hat{\mathbf{u}} \right) y_{1,2}' \sqrt{k_0^2 - \left(k_{x1,2}^i \right)^2}}{\sqrt{r_s^2 + \left(\hat{\mathbf{y}} \cdot \hat{\mathbf{u}} \right)^2 y_{1,2}'^2 + \left(\hat{\mathbf{y}} \cdot \hat{\mathbf{v}} \right)^2 y_{1,2}'^2 + 2 r_s \left(\hat{\mathbf{y}} \cdot \hat{\mathbf{v}} \right) y_{1,2}'}}. \tag{253}$$

These four unknowns are the critical points of the first kind, i.e., $k_{x1,2}^i$ and $k_{u1,2}^i$. By substituting Eq. (252) into Eq. (253) and vice versa, one then determines the critical points of the first kind as

$$k_{x1,2}^i \approx \frac{k_0}{r_s} x_{1,2}' \quad k_{u1,2}^i \approx \frac{k_0 \left(\hat{\mathbf{y}} \cdot \hat{\mathbf{u}} \right)}{r_s} y_{1,2}'. \tag{254}$$

Equation (156) above repeats this MoSP result.

In writing Eq. (254), one replaces $\pm\left|x'_{1,2}\right|$ and $\pm\left|y'_{1,2}\right|$ (which result from solving quadratic expressions) with $x'_{1,2}$ and $y'_{1,2}$. This result is physically intuitive based on the macro-scale scattering geometry given in Figure 9a. Furthermore, one assumes that

$$\sqrt{r_s^2 + x'^2_{1,2} + \left[\left(\hat{\mathbf{y}}\cdot\hat{\mathbf{u}}\right)^2 + \left(\hat{\mathbf{y}}\cdot\hat{\mathbf{v}}\right)^2\right] y'^2_{1,2} + 2r_s\left(\hat{\mathbf{y}}\cdot\hat{\mathbf{v}}\right) y'_{1,2}} \approx r_s \,. \tag{255}$$

This is analogous to saying that distance from source-plane origin to the surface-plane origin is much greater than half the surface length, i.e., $r_s \gg L$, which is typically the case for most directed-energy and remote-sensing engagement scenarios. To provide some idea of how much greater, letting $r_s = 5L$, $r_s = 25L$, and $r_s = 100L$ results in percentage errors of 18%, 4%, and 1%, respectively. These percentage errors result from setting $x'_{1,2} = y'_{1,2} = L$, $\hat{\mathbf{y}}\cdot\hat{\mathbf{v}} = \sin\left(\theta^i\right) = 1$, and $\hat{\mathbf{y}}\cdot\hat{\mathbf{v}} = -\cos\left(\theta^i\right) = 0$ in Eq. (255).

Provided Eqs. (248)-(251), one then computes the following second-order partial derivatives:

$$\frac{\partial^2 g}{\partial\left(k^i_{x1}\right)^2} = \frac{\left(k^i_{x1}\right)^2\left[r_s + \left(\hat{\mathbf{y}}\cdot\hat{\mathbf{v}}\right) y'_1\right]}{k_0^4\left[1 - \left(\frac{k^i_{x1}}{k_0}\right)^2 - \left(\frac{k^i_{u1}}{k_0}\right)^2\right]^{3/2}} + \frac{r_s + \left(\hat{\mathbf{y}}\cdot\hat{\mathbf{v}}\right) y'_1}{k_0^2\sqrt{1 - \left(\frac{k^i_{x1}}{k_0}\right)^2 - \left(\frac{k^i_{u1}}{k_0}\right)^2}}\,, \tag{256}$$

$$\frac{\partial^2 g}{\partial\left(k^i_{x2}\right)^2} = -\frac{\left(k^i_{x2}\right)^2\left[r_s + \left(\hat{\mathbf{y}}\cdot\hat{\mathbf{v}}\right) y'_2\right]}{k_0^4\left[1 - \left(\frac{k^i_{x2}}{k_0}\right)^2 - \left(\frac{k^i_{u2}}{k_0}\right)^2\right]^{3/2}} - \frac{r_s + \left(\hat{\mathbf{y}}\cdot\hat{\mathbf{v}}\right) y'_2}{k_0^2\sqrt{1 - \left(\frac{k^i_{x2}}{k_0}\right)^2 - \left(\frac{k^i_{u2}}{k_0}\right)^2}}\,, \tag{257}$$

$$\frac{\partial^2 g}{\partial\left(k^i_{u1}\right)^2} = \frac{\left(k^i_{u1}\right)^2\left[r_s + \left(\hat{\mathbf{y}}\cdot\hat{\mathbf{v}}\right) y'_1\right]}{k_0^4\left[1 - \left(\frac{k^i_{x1}}{k_0}\right)^2 - \left(\frac{k^i_{u1}}{k_0}\right)^2\right]^{3/2}} + \frac{r_s + \left(\hat{\mathbf{y}}\cdot\hat{\mathbf{v}}\right) y'_1}{k_0^2\sqrt{1 - \left(\frac{k^i_{x1}}{k_0}\right)^2 - \left(\frac{k^i_{u1}}{k_0}\right)^2}}\,, \tag{258}$$

$$\frac{\partial^2 g}{\partial\left(k_{u2}^i\right)^2}=-\frac{\left(k_{u2}^i\right)^2\left[r_s+\left(\hat{\mathbf{y}}\cdot\hat{\mathbf{v}}\right)y_2'\right]}{k_0^4\left[1-\left(\frac{k_{x2}^i}{k_0}\right)^2-\left(\frac{k_{u2}^i}{k_0}\right)^2\right]^{3/2}}-\frac{r_s+\left(\hat{\mathbf{y}}\cdot\hat{\mathbf{v}}\right)y_2'}{k_0^2\sqrt{1-\left(\frac{k_{x2}^i}{k_0}\right)^2-\left(\frac{k_{u2}^i}{k_0}\right)^2}}, \tag{259}$$

$$\frac{\partial^2 g}{\partial k_{x1}^i\partial k_{x2}^i}=\frac{\partial^2 g}{\partial k_{x1}^i\partial k_{u2}^i}=\frac{\partial^2 g}{\partial k_{u1}^i\partial k_{u2}^i}=\frac{\partial^2 g}{\partial k_{u1}^i\partial k_{x2}^i}=0\,, \tag{260}$$

$$\frac{\partial^2 g}{\partial k_{x1}^i\partial k_{u1}^i}=\frac{k_{x1}^i k_{u1}^i\left[r_s+\left(\hat{\mathbf{y}}\cdot\hat{\mathbf{v}}\right)y_1'\right]}{k_0^4\left[1-\left(\frac{k_{x1}^i}{k_0}\right)^2-\left(\frac{k_{u1}^i}{k_0}\right)^2\right]^{3/2}}\approx 0\,, \tag{261}$$

and

$$\frac{\partial^2 g}{\partial k_{x2}^i\partial k_{u2}^i}=-\frac{k_{x2}^i k_{u2}^i\left[r_s+\left(\hat{\mathbf{y}}\cdot\hat{\mathbf{v}}\right)y_2'\right]}{k_0^4\left[1-\left(\frac{k_{x2}^i}{k_0}\right)^2-\left(\frac{k_{u2}^i}{k_0}\right)^2\right]^{3/2}}\approx 0\,. \tag{262}$$

In Eqs. (261) and (262), one assumes that $k_0 \gg k_x^i$ and $k_0 \gg k_u^i$ (reasons discussed below); consequently, $\partial^2 g$ becomes a diagonal matrix upon substituting Eqs. (256)-(262) into Eq. (245). Subsequent evaluation of $\partial^2 g$ at the critical points of the first kind [cf. Eq. (254)] results in the following relationships:

$$\mathrm{Det}\left\{\partial^2 g_0\right\}=\frac{r_s^8\left[r_s+\left(\hat{\mathbf{y}}\cdot\hat{\mathbf{v}}\right)y_1'\right]^2\left[r_s+\left(\hat{\mathbf{y}}\cdot\hat{\mathbf{v}}\right)y_2'\right]^2}{k_0^8\left[x_1'^2+\left(\hat{\mathbf{y}}\cdot\hat{\mathbf{v}}\right)^2 y_1'^2-r_s^2\right]^2\left[x_2'^2+\left(\hat{\mathbf{y}}\cdot\hat{\mathbf{v}}\right)^2 y_2'^2-r_s^2\right]^2}\approx\frac{r_s^4}{k_0^8}\,, \tag{263}$$

and

$$\mathrm{sgn}\left\{\partial^2 g_0\right\}=\lambda_+\left\{\partial^2 g_0\right\}-\lambda_-\left\{\partial^2 g_0\right\}\approx 0\,, \tag{264}$$

where $\lambda_\pm\left\{\partial^2 g_0\right\}$ are the number of positive and negative eigenvalues of $\partial^2 g_0$. Equations (152)-(155) above use these relationships in combination with Eq. (244).

As discussed above in Section 4.3, the analysis assumes that $k_v^i \gg k_x^i$ and $k_v^i \gg k_u^i$. In so doing, the analysis also assumes that

$$k_{v1,2}^i \approx \begin{cases} k_0, & \text{in } \vec{\vec{\mathbf{f}}} \\ k_0 - \dfrac{\left(k_{x1,2}^i\right)^2}{2k_0} - \dfrac{\left(k_{u1,2}^i\right)^2}{2k_0}, & \text{in } g \end{cases}. \tag{265}$$

Thus, in evaluating the phase function g [cf. Eq. (246)] at the critical points of the first kind [cf. Eq. (254)], the following relationship results:

$$\begin{aligned} g_0 = {} & \frac{x_2'^2}{2r_s} - \frac{x_1'^2}{2r_s} + \frac{\left(\hat{\mathbf{y}}\cdot\hat{\mathbf{u}}\right)^2 y_2'^2}{2r_s} - \frac{\left(\hat{\mathbf{y}}\cdot\hat{\mathbf{u}}\right)^2 y_1'^2}{2r_s} + \left(\hat{\mathbf{y}}\cdot\hat{\mathbf{v}}\right) y_2' - \left(\hat{\mathbf{y}}\cdot\hat{\mathbf{v}}\right) y_1' \\ & + \left(\hat{\mathbf{x}}\cdot\hat{\mathbf{r}}_1 x_1' - \hat{\mathbf{x}}\cdot\hat{\mathbf{r}}_2 x_2'\right) + \left(\hat{\mathbf{y}}\cdot\hat{\mathbf{r}}_1 y_1' - \hat{\mathbf{y}}\cdot\hat{\mathbf{r}}_2 y_2'\right) \end{aligned}. \tag{266}$$

Equations (152)-(155) and subsequently Eq. (157) above use this relationship in combination with Eq. (244). With this in mind, the analysis evaluates the representative amplitude dyadic $\vec{\vec{\mathbf{f}}}$ [cf. Eqs. (145)-(148)] at the critical points of the first kind below in Appendix D.

Appendix D. Defining the dyadics that contain all of the amplitude and phase terms evaluated at the critical points of the first kind

In using the MoSP to simplify Eqs. (141)-(144), Eqs. (152)-(156) result. Inherent in Eq. (152)-(155) are the following dyadics:

$$\vec{\vec{\mathcal{L}}} = \int_{-L}^{L}\int_{-L}^{L}\int_{-L}^{L}\int_{-L}^{L} \vec{\vec{\mathbf{f}}}_0^{\mathcal{L}}\, \mathrm{e}^{jk_0 g_0}\, dx_1' dx_2' dy_1' dy_2' \,, \tag{267}$$

$$\vec{\vec{\mathcal{K}}} = \int_{-L}^{L}\int_{-L}^{L}\int_{-L}^{L}\int_{-L}^{L} \vec{\vec{\mathbf{f}}}_0^{\mathcal{K}}\, \mathrm{e}^{jk_0 g_0}\, dx_1' dx_2' dy_1' dy_2' \,, \tag{268}$$

$$\vec{\vec{\mathcal{M}}} = \int_{-L}^{L}\int_{-L}^{L}\int_{-L}^{L}\int_{-L}^{L} \vec{\vec{\mathbf{f}}}_0^{\mathcal{M}}\, \mathrm{e}^{jk_0 g_0}\, dx_1' dx_2' dy_1' dy_2' \,, \tag{269}$$

and

$$\vec{\vec{\mathcal{N}}} = \int_{-L}^{L}\int_{-L}^{L}\int_{-L}^{L}\int_{-L}^{L} \vec{\vec{\mathbf{f}}}_0^{\mathcal{N}}\, \mathrm{e}^{jk_0 g_0}\, dx_1' dx_2' dy_1' dy_2' \,, \tag{270}$$

where $\vec{\vec{\mathbf{f}}}_0^{\mathcal{L}}$, $\vec{\vec{\mathbf{f}}}_0^{\mathcal{K}}$, $\vec{\vec{\mathbf{f}}}_0^{\mathcal{M}}$, and $\vec{\vec{\mathbf{f}}}_0^{\mathcal{N}}$ are the amplitude dyadics evaluated at the critical points of the first kind, respectively, and g_0 is a common phase function which is also evaluated at the critical points of the first kind. Provided Eqs. (267)-(270), the purpose of this appendix is to explicitly define the dyadics $\vec{\vec{\mathcal{L}}}$, $\vec{\vec{\mathcal{K}}}$, $\vec{\vec{\mathcal{M}}}$, and $\vec{\vec{\mathcal{N}}}$ for different material substrates, i.e., dielectrics, conductors, and a perfect electrical conductor (PEC).

General problem for dielectrics

With some mathematical prowess, one establishes the dyadics given in Eqs. (267) -(270) as

$$\begin{aligned}\overleftrightarrow{\mathcal{L}} &= \begin{bmatrix} \mathcal{L}_{xx} & \mathcal{L}_{xy} & \mathcal{L}_{xz} \\ \mathcal{L}_{yx} & \mathcal{L}_{yy} & \mathcal{L}_{yz} \\ \mathcal{L}_{zx} & \mathcal{L}_{zy} & \mathcal{L}_{zz} \end{bmatrix} \\ &= \mathcal{L}_{\mathrm{ij}} \quad (\mathrm{i}=x,y,z;\ \mathrm{j}=x,y,z) \quad , \\ &= \frac{\mathrm{sgn}\left(\mathcal{L}_{\mathrm{ij}}\right)}{\Delta_1\Delta_2} \sum_{\mathrm{m}=x,u} \sum_{\mathrm{n}=x,u} \Lambda^{\mathrm{i}}_{\mathrm{m1}} \Lambda^{\mathrm{j}*}_{\mathrm{n2}} \Psi_{\mathrm{mn}} \end{aligned} \tag{271}$$

$$\begin{aligned}\overleftrightarrow{\mathcal{K}} &= \begin{bmatrix} \mathcal{K}_{xx} & \mathcal{K}_{xy} & \mathcal{K}_{xz} \\ \mathcal{K}_{yx} & \mathcal{K}_{yy} & \mathcal{K}_{yz} \\ \mathcal{K}_{zx} & \mathcal{K}_{zy} & \mathcal{K}_{zz} \end{bmatrix} \\ &= \mathcal{K}_{\mathrm{ij}} \quad (\mathrm{i}=x,y,z;\ \mathrm{j}=x,y,z) \quad , \\ &= \frac{\mathrm{sgn}\left(\mathcal{K}_{\mathrm{ij}}\right)}{\Delta_1\Delta_2} \sum_{\mathrm{m}=x,u} \sum_{\mathrm{n}=x,u} \Lambda^{\mathrm{i}}_{\mathrm{m1}} \Theta^{\mathrm{j}*}_{\mathrm{n2}} \Psi_{\mathrm{mn}} \end{aligned} \tag{272}$$

$$\begin{aligned}\overleftrightarrow{\mathcal{M}} &= \begin{bmatrix} \mathcal{M}_{xx} & \mathcal{M}_{xy} & \mathcal{M}_{xz} \\ \mathcal{M}_{yx} & \mathcal{M}_{yy} & \mathcal{M}_{yz} \\ \mathcal{M}_{zx} & \mathcal{M}_{zy} & \mathcal{M}_{zz} \end{bmatrix} \\ &= \mathcal{M}_{\mathrm{ij}} \quad (\mathrm{i}=x,y,z;\ \mathrm{j}=x,y,z) \quad , \\ &= \frac{\mathrm{sgn}\left(\mathcal{M}_{\mathrm{ij}}\right)}{\Delta_1\Delta_2} \sum_{\mathrm{m}=x,u} \sum_{\mathrm{n}=x,u} \Theta^{\mathrm{i}}_{\mathrm{m1}} \Lambda^{\mathrm{j}*}_{\mathrm{n2}} \Psi_{\mathrm{mn}} \end{aligned} \tag{273}$$

$$\begin{aligned}\overleftrightarrow{\mathcal{N}} &= \begin{bmatrix} \mathcal{N}_{xx} & \mathcal{N}_{xy} & \mathcal{N}_{xz} \\ \mathcal{N}_{yx} & \mathcal{N}_{yy} & \mathcal{N}_{yz} \\ \mathcal{N}_{zx} & \mathcal{N}_{zy} & \mathcal{N}_{zz} \end{bmatrix} \\ &= \mathcal{N}_{\mathrm{ij}} \quad (\mathrm{i}=x,y,z;\ \mathrm{j}=x,y,z) \quad . \\ &= \frac{\mathrm{sgn}\left(\mathcal{N}_{\mathrm{ij}}\right)}{\Delta_1\Delta_2} \sum_{\mathrm{m}=x,u} \sum_{\mathrm{n}=x,u} \Theta^{\mathrm{i}}_{\mathrm{m1}} \Theta^{\mathrm{j}*}_{\mathrm{n2}} \Psi_{\mathrm{mn}} \end{aligned} \tag{274}$$

and

In Eqs. (271)-(274), Ψ_{xx}, Ψ_{xu}, Ψ_{ux}, and Ψ_{uu} are the remaining integrals with respect to the parameterized rough surface [cf. Eq. (157)]. The analysis above determines closed-form solutions for these integrals in sub-section 4.3.1 for smooth-to-moderately rough

surfaces and in sub-section 4.3.2 for very rough surfaces. With this said, one determines the other parameters in Eqs. (271)-(274) as

$$\begin{aligned}
\operatorname{sgn}\left(\mathcal{L}_{\mathrm{ij}}\right) &= \begin{cases} -1 & \text{if } \mathcal{L}_{\mathrm{ij}} = \mathcal{L}_{xz},\, \mathcal{L}_{yz},\, \mathcal{L}_{zx}, \text{ or } \mathcal{L}_{zy} \\ 1 & \text{otherwise} \end{cases} \\
\operatorname{sgn}\left(\mathcal{K}_{\mathrm{ij}}\right) &= \begin{cases} -1 & \text{if } \mathcal{K}_{\mathrm{ij}} = \mathcal{K}_{xy},\, \mathcal{K}_{yy},\, \mathcal{K}_{zx}, \text{ or } \mathcal{K}_{zz} \\ 1 & \text{otherwise} \end{cases} \\
\operatorname{sgn}\left(\mathcal{M}_{\mathrm{ij}}\right) &= \begin{cases} -1 & \text{if } \mathcal{M}_{\mathrm{ij}} = \mathcal{M}_{xz},\, \mathcal{M}_{yx},\, \mathcal{M}_{yy}, \text{ or } \mathcal{M}_{zz} \\ 1 & \text{otherwise} \end{cases} \\
\operatorname{sgn}\left(\mathcal{N}_{\mathrm{ij}}\right) &= \begin{cases} -1 & \text{if } \mathcal{N}_{\mathrm{ij}} = \mathcal{N}_{xy},\, \mathcal{N}_{yx},\, \mathcal{N}_{yz}, \text{ or } \mathcal{N}_{zy} \\ 1 & \text{otherwise} \end{cases}
\end{aligned}, \tag{275}$$

$$\Delta_{1,2} = \left\{\left[\left(\hat{\mathbf{y}}\cdot\hat{\mathbf{v}}\right)\vartheta_{z1,2} - \left(\hat{\mathbf{z}}\cdot\hat{\mathbf{v}}\right)\vartheta_{y1,2}\right]^2 + \left[\left(\hat{\mathbf{y}}\cdot\hat{\mathbf{v}}\right)^2 + \left(\hat{\mathbf{z}}\cdot\hat{\mathbf{v}}\right)^2\right]\vartheta_{x1,2}^2\right\}\vartheta_{x1,2}, \tag{276}$$

$$\begin{aligned}
\Lambda_{x1,2}^{x} = &\left[\left(\hat{\mathbf{y}}\cdot\hat{\mathbf{v}}\right)^2\left(1+r_{\|1,2}\right) + \left(\hat{\mathbf{z}}\cdot\hat{\mathbf{v}}\right)^2\left(1+r_{\|1,2}\right) - \left(1+r_{\perp 1,2}\right)\right] \\
&\left[\left(\hat{\mathbf{y}}\cdot\hat{\mathbf{v}}\right)\vartheta_{z1,2} - \left(\hat{\mathbf{z}}\cdot\hat{\mathbf{v}}\right)\vartheta_{y1,2}\right]\left[\left(\hat{\mathbf{y}}\cdot\hat{\mathbf{v}}\right)\vartheta_{y1,2} + \left(\hat{\mathbf{z}}\cdot\hat{\mathbf{v}}\right)\vartheta_{z1,2}\right]\vartheta_{x1,2}
\end{aligned}, \tag{277}$$

$$\begin{aligned}
\Lambda_{u1,2}^{x} = &\left[\left(\hat{\mathbf{y}}\cdot\hat{\mathbf{v}}\right)\left(\hat{\mathbf{z}}\cdot\hat{\mathbf{u}}\right) - \left(\hat{\mathbf{y}}\cdot\hat{\mathbf{u}}\right)\left(\hat{\mathbf{z}}\cdot\hat{\mathbf{v}}\right)\right] \\
&\left[\left(1+r_{\perp 1,2}\right)\vartheta_{x1,2}^2 + \left(1+r_{\|1,2}\right)\left[\left(\hat{\mathbf{y}}\cdot\hat{\mathbf{v}}\right)\vartheta_{z1,2} - \left(\hat{\mathbf{z}}\cdot\hat{\mathbf{v}}\right)\vartheta_{y1,2}\right]^2\right], \\
&\left[\left(\hat{\mathbf{y}}\cdot\hat{\mathbf{v}}\right)\vartheta_{y1,2} + \left(\hat{\mathbf{z}}\cdot\hat{\mathbf{v}}\right)\vartheta_{z1,2}\right]
\end{aligned} \tag{278}$$

$$\begin{aligned}
\Lambda_{x1,2}^{y} = &\left(1+r_{\perp 1,2}\right)\vartheta_{z1,2}\left[\left(\hat{\mathbf{y}}\cdot\hat{\mathbf{v}}\right)\vartheta_{z1,2} - \left(\hat{\mathbf{z}}\cdot\hat{\mathbf{v}}\right)\vartheta_{y1,2}\right]^2 \\
&+\left\{\left(\hat{\mathbf{y}}\cdot\hat{\mathbf{v}}\right)\left(\hat{\mathbf{z}}\cdot\hat{\mathbf{v}}\right)\left[\left(\hat{\mathbf{y}}\cdot\hat{\mathbf{v}}\right)^2\left(1+r_{\|1,2}\right) + \left(\hat{\mathbf{z}}\cdot\hat{\mathbf{v}}\right)^2\left(1+r_{\|1,2}\right) - \left(1+r_{\perp 1,2}\right)\right]\vartheta_{y1,2}\right. \\
&\left.+\left[\left(\hat{\mathbf{z}}\cdot\hat{\mathbf{v}}\right)^4\left(1+r_{\|1,2}\right) + \left(\hat{\mathbf{y}}\cdot\hat{\mathbf{v}}\right)^2\left(\hat{\mathbf{z}}\cdot\hat{\mathbf{v}}\right)^2\left(1+r_{\|1,2}\right) + \left(\hat{\mathbf{y}}\cdot\hat{\mathbf{v}}\right)^2\left(1+r_{\perp 1,2}\right)\right]\vartheta_{z1,2}\right\}\vartheta_{x1,2}^2
\end{aligned}, \tag{279}$$

$$\begin{aligned}
\Lambda_{u1,2}^{y} = &\left[\left(\hat{\mathbf{y}}\cdot\hat{\mathbf{v}}\right)\left(\hat{\mathbf{z}}\cdot\hat{\mathbf{u}}\right) - \left(\hat{\mathbf{y}}\cdot\hat{\mathbf{u}}\right)\left(\hat{\mathbf{z}}\cdot\hat{\mathbf{v}}\right)\right] \\
&\left\{\left[\left(\hat{\mathbf{y}}\cdot\hat{\mathbf{v}}\right)\left(\hat{\mathbf{z}}\cdot\hat{\mathbf{v}}\right)\left(1+r_{\|1,2}\right)\vartheta_{y1,2} + \left(\hat{\mathbf{z}}\cdot\hat{\mathbf{v}}\right)^2\left(1+r_{\|1,2}\right)\vartheta_{z1,2} - \left(1+r_{\perp 1,2}\right)\vartheta_{z1,2}\right], \\
&\left[\left(\hat{\mathbf{y}}\cdot\hat{\mathbf{v}}\right)\vartheta_{z1,2} - \left(\hat{\mathbf{z}}\cdot\hat{\mathbf{v}}\right)\vartheta_{y1,2}\right] - \left(\hat{\mathbf{y}}\cdot\hat{\mathbf{v}}\right)\left(1+r_{\perp 1,2}\right)\vartheta_{x1,2}^2\right\}\vartheta_{x1,2}
\end{aligned} \tag{280}$$

$$\begin{aligned}\Lambda^{z}_{x1,2} &= \left(\hat{\mathbf{y}}\cdot\hat{\mathbf{v}}\right)^2\left(1+r_{\perp 1,2}\right)\vartheta_{y1,2}\vartheta^2_{z1,2}\\ &+\left(\hat{\mathbf{y}}\cdot\hat{\mathbf{v}}\right)\left(\hat{\mathbf{z}}\cdot\hat{\mathbf{v}}\right)\left[\left(\hat{\mathbf{y}}\cdot\hat{\mathbf{v}}\right)^2\left(1+r_{\|1,2}\right)+\left(\hat{\mathbf{z}}\cdot\hat{\mathbf{v}}\right)^2\left(1+r_{\|1,2}\right)-\left(1+r_{\perp 1,2}\right)\right]\vartheta^2_{x1,2}\vartheta_{z1,2}\\ &+\left[\left(\hat{\mathbf{y}}\cdot\hat{\mathbf{v}}\right)^4\left(1+r_{\|1,2}\right)+\left(\hat{\mathbf{y}}\cdot\hat{\mathbf{v}}\right)^2\left(\hat{\mathbf{z}}\cdot\hat{\mathbf{v}}\right)^2\left(1+r_{\|1,2}\right)+\left(\hat{\mathbf{z}}\cdot\hat{\mathbf{v}}\right)^2\left(1+r_{\perp 1,2}\right)\right]\vartheta^2_{x1,2}\vartheta_{y1,2}\\ &+\left(\hat{\mathbf{z}}\cdot\hat{\mathbf{v}}\right)^2\left(1+r_{\perp 1,2}\right)\vartheta^3_{y1,2}-2\left(\hat{\mathbf{y}}\cdot\hat{\mathbf{v}}\right)\left(\hat{\mathbf{z}}\cdot\hat{\mathbf{v}}\right)\left(1+r_{\perp 1,2}\right)\vartheta^2_{y1,2}\vartheta_{z1,2}\end{aligned}, \quad (281)$$

$$\begin{aligned}\Lambda^{z}_{u1,2} &= \left[\left(\hat{\mathbf{y}}\cdot\hat{\mathbf{v}}\right)\left(\hat{\mathbf{z}}\cdot\hat{\mathbf{u}}\right)-\left(\hat{\mathbf{y}}\cdot\hat{\mathbf{u}}\right)\left(\hat{\mathbf{z}}\cdot\hat{\mathbf{v}}\right)\right]\left\{\left(\hat{\mathbf{z}}\cdot\hat{\mathbf{v}}\right)\left[\left(1+r_{\perp 1,2}\right)-\left(\hat{\mathbf{y}}\cdot\hat{\mathbf{v}}\right)^2\left(1+r_{\|1,2}\right)\right]\vartheta^2_{y1,2}\right.\\ &+\left(\hat{\mathbf{z}}\cdot\hat{\mathbf{v}}\right)\left[\left(1+r_{\perp 1,2}\right)\vartheta^2_{x1,2}+\left(\hat{\mathbf{y}}\cdot\hat{\mathbf{v}}\right)^2\left(1+r_{\|1,2}\right)\vartheta^2_{z1,2}\right]\\ &\left.+\left(\hat{\mathbf{y}}\cdot\hat{\mathbf{v}}\right)\left[\left(\hat{\mathbf{y}}\cdot\hat{\mathbf{v}}\right)^2\left(1+r_{\|1,2}\right)-\left(\hat{\mathbf{z}}\cdot\hat{\mathbf{v}}\right)^2\left(1+r_{\|1,2}\right)-\left(1+r_{\perp 1,2}\right)\right]\vartheta_{y1,2}\vartheta_{z1,2}\right\}\vartheta_{x1,2}\end{aligned}, \quad (282)$$

$$\begin{aligned}\Theta^{x}_{x1,2} &= -\left\{\left(1-r_{\perp 1,2}\right)\left[\left(\hat{\mathbf{y}}\cdot\hat{\mathbf{v}}\right)\vartheta_{z1,2}-\left(\hat{\mathbf{z}}\cdot\hat{\mathbf{v}}\right)\vartheta_{y1,2}\right]^2\right.\\ &\left.+\left[\left(\hat{\mathbf{y}}\cdot\hat{\mathbf{v}}\right)^2+\left(\hat{\mathbf{z}}\cdot\hat{\mathbf{v}}\right)^2\right]\left(1-r_{\|1,2}\right)\vartheta^2_{x1,2}\right\}\left[\left(\hat{\mathbf{y}}\cdot\hat{\mathbf{v}}\right)\vartheta_{y1,2}+\left(\hat{\mathbf{z}}\cdot\hat{\mathbf{v}}\right)\vartheta_{z1,2}\right]\end{aligned}, \quad (283)$$

$$\begin{aligned}\Theta^{x}_{u1,2} &= \left[\left(\hat{\mathbf{y}}\cdot\hat{\mathbf{v}}\right)\left(\hat{\mathbf{z}}\cdot\hat{\mathbf{u}}\right)-\left(\hat{\mathbf{y}}\cdot\hat{\mathbf{u}}\right)\left(\hat{\mathbf{z}}\cdot\hat{\mathbf{v}}\right)\right]\\ &\left(r_{\|1,2}-r_{\perp 1,2}\right)\left[\left(\hat{\mathbf{y}}\cdot\hat{\mathbf{v}}\right)\vartheta_{z1,2}-\left(\hat{\mathbf{z}}\cdot\hat{\mathbf{v}}\right)\vartheta_{y1,2}\right]\left[\left(\hat{\mathbf{y}}\cdot\hat{\mathbf{v}}\right)\vartheta_{y1,2}+\left(\hat{\mathbf{z}}\cdot\hat{\mathbf{v}}\right)\vartheta_{z1,2}\right]\vartheta_{x1,2}\end{aligned}, \quad (284)$$

$$\begin{aligned}\Theta^{y}_{x1,2} &= -\left\{\left(\hat{\mathbf{y}}\cdot\hat{\mathbf{v}}\right)\left[\left(\hat{\mathbf{y}}\cdot\hat{\mathbf{v}}\right)^2+\left(\hat{\mathbf{z}}\cdot\hat{\mathbf{v}}\right)^2\right]\left(1-r_{\|1,2}\right)\vartheta^2_{x1,2}\right.\\ &+\left[\left(\hat{\mathbf{y}}\cdot\hat{\mathbf{v}}\right)^2\left(1-r_{\|1,2}\right)\vartheta_{z1,2}+\left(\hat{\mathbf{z}}\cdot\hat{\mathbf{v}}\right)^2\left(r_{\perp 1,2}-r_{\|1,2}\right)\vartheta_{z1,2}\right.\\ &\left.\left.-\left(\hat{\mathbf{y}}\cdot\hat{\mathbf{v}}\right)\left(\hat{\mathbf{z}}\cdot\hat{\mathbf{v}}\right)\left(1-r_{\perp 1,2}\right)\vartheta_{y1,2}\right]\left[\left(\hat{\mathbf{y}}\cdot\hat{\mathbf{v}}\right)\vartheta_{z1,2}-\left(\hat{\mathbf{z}}\cdot\hat{\mathbf{v}}\right)\vartheta_{y1,2}\right]\right\}\vartheta_{x1,2}\end{aligned}, \quad (285)$$

$$\begin{aligned}\Theta^{y}_{u1,2} &= -\left[\left(\hat{\mathbf{y}}\cdot\hat{\mathbf{v}}\right)\left(\hat{\mathbf{z}}\cdot\hat{\mathbf{u}}\right)-\left(\hat{\mathbf{y}}\cdot\hat{\mathbf{u}}\right)\left(\hat{\mathbf{z}}\cdot\hat{\mathbf{v}}\right)\right]\left\{\left(1-r_{\|1,2}\right)\vartheta_{z1,2}\left[\left(\hat{\mathbf{y}}\cdot\hat{\mathbf{v}}\right)\vartheta_{z1,2}-\left(\hat{\mathbf{z}}\cdot\hat{\mathbf{v}}\right)\vartheta_{y1,2}\right]^2\right.\\ &+\left[\left(\hat{\mathbf{y}}\cdot\hat{\mathbf{v}}\right)\left(\hat{\mathbf{z}}\cdot\hat{\mathbf{v}}\right)\left(r_{\|1,2}-r_{\perp 1,2}\right)\vartheta_{y1,2}+\left(\hat{\mathbf{y}}\cdot\hat{\mathbf{v}}\right)^2\left(1-r_{\|1,2}\right)\vartheta_{z1,2}\right.\\ &\left.\left.+\left(\hat{\mathbf{z}}\cdot\hat{\mathbf{v}}\right)^2\left(1-r_{\perp 1,2}\right)\vartheta_{z1,2}\right]\vartheta^2_{x1,2}\right\}\end{aligned}, \quad (286)$$

$$\begin{aligned}\Theta^{z}_{x1,2} &= \left\{\left[\left(\hat{\mathbf{y}}\cdot\hat{\mathbf{v}}\right)^2+\left(\hat{\mathbf{z}}\cdot\hat{\mathbf{v}}\right)^2\right]\left(1-r_{\|1,2}\right)\left[\left(\hat{\mathbf{z}}\cdot\hat{\mathbf{v}}\right)\vartheta^2_{x1,2}+\left(\hat{\mathbf{z}}\cdot\hat{\mathbf{v}}\right)\vartheta^2_{y1,2}-\left(\hat{\mathbf{y}}\cdot\hat{\mathbf{v}}\right)\vartheta_{y1,2}\vartheta_{z1,2}\right]\right.\\ &+\left(\hat{\mathbf{y}}\cdot\hat{\mathbf{v}}\right)\left(1-r_{\perp 1,2}\right)\left[\left(\hat{\mathbf{y}}\cdot\hat{\mathbf{v}}\right)\left(\hat{\mathbf{z}}\cdot\hat{\mathbf{v}}\right)\vartheta^2_{z1,2}-\left(\hat{\mathbf{y}}\cdot\hat{\mathbf{v}}\right)\left(\hat{\mathbf{z}}\cdot\hat{\mathbf{v}}\right)\vartheta^2_{y1,2}\right.\\ &\left.\left.+\left[\left(\hat{\mathbf{y}}\cdot\hat{\mathbf{v}}\right)^2-\left(\hat{\mathbf{z}}\cdot\hat{\mathbf{v}}\right)^2\right]\vartheta_{y1,2}\vartheta_{z1,2}\right]\right\}\vartheta_{x1,2}\end{aligned}, \quad (287)$$

$$\Theta_{u1,2}^{z} = -\left[\left(\hat{\mathbf{y}}\cdot\hat{\mathbf{v}}\right)\left(\hat{\mathbf{z}}\cdot\hat{\mathbf{u}}\right)-\left(\hat{\mathbf{y}}\cdot\hat{\mathbf{u}}\right)\left(\hat{\mathbf{z}}\cdot\hat{\mathbf{v}}\right)\right]\left\{\left(1-r_{\|1,2}\right)\vartheta_{y1,2}\left[\left(\hat{\mathbf{y}}\cdot\hat{\mathbf{v}}\right)\vartheta_{z1,2}-\left(\hat{\mathbf{z}}\cdot\hat{\mathbf{v}}\right)\vartheta_{y1,2}\right]^{2}\right.$$
$$+\left[\left(\hat{\mathbf{y}}\cdot\hat{\mathbf{v}}\right)\left(\hat{\mathbf{z}}\cdot\hat{\mathbf{v}}\right)\left(r_{\|1,2}-r_{\perp 1,2}\right)\vartheta_{z1,2}+\left(\hat{\mathbf{z}}\cdot\hat{\mathbf{v}}\right)^{2}\left(1-r_{\|1,2}\right)\vartheta_{y1,2}\right. \quad ,(288)$$
$$\left.\left.+\left(\hat{\mathbf{y}}\cdot\hat{\mathbf{v}}\right)^{2}\left(1-r_{\perp 1,2}\right)\vartheta_{y1,2}\right]\vartheta_{x1,2}^{2}\right\}$$

and
$$\vartheta_{x1,2} = \hat{\mathbf{x}}\cdot\hat{\mathbf{r}}_{1,2} \quad \vartheta_{y1,2} = \hat{\mathbf{y}}\cdot\hat{\mathbf{r}}_{1,2} - \hat{\mathbf{y}}\cdot\hat{\mathbf{v}} \quad \vartheta_{z1,2} = \hat{\mathbf{z}}\cdot\hat{\mathbf{r}}_{1,2} - \hat{\mathbf{z}}\cdot\hat{\mathbf{v}}\,. \tag{289}$$

In Eqs. (277)-(288), $r_{\perp 1,2}$ and $r_{\|1,2}$ are the perpendicular and parallel Fresnel reflection coefficients for two separate observation points, respectively. Referencing the micro-scale scattering geometry given in Figure 9b, one derives these coefficients as [14]

$$r_{\perp 1,2} = \frac{\eta\cos\left(\theta_{1,2}^{i}\right)-\eta_{0}\cos\left(\theta_{1,2}^{t}\right)}{\eta\cos\left(\theta_{1,2}^{i}\right)+\eta_{0}\cos\left(\theta_{1,2}^{t}\right)} = \frac{n_{0}\cos\left(\theta_{1,2}^{i}\right)-n\sqrt{1-\frac{n_{0}^{2}}{n^{2}}\sin^{2}\left(\theta_{1,2}^{i}\right)}}{n_{0}\cos\left(\theta_{1,2}^{i}\right)+n\sqrt{1-\frac{n_{0}^{2}}{n^{2}}\sin^{2}\left(\theta_{1,2}^{i}\right)}} \tag{290}$$

and
$$r_{\|1,2} = \frac{-\eta_{0}\cos\left(\theta_{1,2}^{i}\right)+\eta\cos\left(\theta_{1,2}^{t}\right)}{\eta_{0}\cos\left(\theta_{1,2}^{i}\right)+\eta\cos\left(\theta_{1,2}^{t}\right)} = \frac{-n\cos\left(\theta_{1,2}^{i}\right)+n_{0}\sqrt{1-\frac{n_{0}^{2}}{n^{2}}\sin^{2}\left(\theta_{1,2}^{i}\right)}}{n\cos\left(\theta_{1,2}^{i}\right)+n_{0}\sqrt{1-\frac{n_{0}^{2}}{n^{2}}\sin^{2}\left(\theta_{1,2}^{i}\right)}}, \tag{291}$$

where
$$\cos\left(\theta_{1,2}^{i}\right) = -\hat{\mathbf{k}}_{1,2}^{i}\cdot\hat{\mathbf{n}}_{1,2}' \approx -\frac{1}{\left|\mathbf{n}_{1,2}\right|}\left[\left(\hat{\mathbf{y}}\cdot\hat{\mathbf{v}}\right)\frac{\vartheta_{y1,2}}{\vartheta_{z1,2}}+\left(\hat{\mathbf{z}}\cdot\hat{\mathbf{v}}\right)\right], \tag{292}$$

$$\sin^{2}\left(\theta_{1,2}^{i}\right) = 1-\cos^{2}\left(\theta_{1,2}^{i}\right) \approx 1-\frac{1}{\left|\mathbf{n}_{1,2}\right|^{2}}\left[\left(\hat{\mathbf{y}}\cdot\hat{\mathbf{v}}\right)\frac{\vartheta_{y1,2}}{\vartheta_{z1,2}}+\left(\hat{\mathbf{z}}\cdot\hat{\mathbf{v}}\right)\right]^{2}, \tag{293}$$

and
$$\left|\mathbf{n}_{1,2}\right| \approx \sqrt{1+\frac{\vartheta_{x1,2}^{2}}{\vartheta_{z1,2}^{2}}+\frac{\vartheta_{y1,2}^{2}}{\vartheta_{z1,2}^{2}}} \tag{294}$$

In writing Eqs. (290) and (291), one must assume that the medium below the statistically rough surface S is nonmagnetic with index of refraction n[21]. Above, the medium is free space with index of refraction $n_0 = 1$. One also uses the law of refraction, i.e., $n\sin\left(\theta^t\right) = n_0 \sin\left(\theta^i\right)$, which is a direct result from the geometrical-optics approximation [22]. Note that these assumptions are valid at optical wavelengths for dielectric materials [20].

Specialization to conductors

For a very good conductor, the conductivity approaches infinity, $\sigma \to \infty$ [14]. As such, the tangential incident electric field approximates to zero all along the surface of the conducting material, i.e., $\hat{\mathbf{n}} \times \mathbf{E}^i \approx 0$, and only the electric equivalent surface current density $\mathbf{J}$ radiates when using the PO approximation. This says that only the dyadic $\vec{\mathcal{N}}$ exists, i.e., $\vec{\mathcal{L}} \approx \vec{\mathcal{K}} \approx \vec{\mathcal{M}} \approx 0$, and the analysis simplifies greatly from that of dielectrics. Furthermore, $\theta_{1,2}^t \approx 0$ in Eqs. (290) and (291) [14]. Based on this knowledge,

$$r_{\perp 1,2} = \frac{n_0 \cos\left(\theta_{1,2}^i\right) - n\cos\left(\theta_{1,2}^t\right)}{n_0 \cos\left(\theta_{1,2}^i\right) + n\cos\left(\theta_{1,2}^t\right)} \approx \frac{n_0 \cos\left(\theta_{1,2}^i\right) - n}{n_0 \cos\left(\theta_{1,2}^i\right) + n} \tag{295}$$

and

$$r_{\parallel 1,2} = \frac{-n\cos\left(\theta_{1,2}^i\right) + n_0 \cos\left(\theta_{1,2}^t\right)}{n\cos\left(\theta_{1,2}^i\right) + n_0 \cos\left(\theta_{1,2}^t\right)} \approx \frac{-n\cos\left(\theta_{1,2}^i\right) + n_0}{n\cos\left(\theta_{1,2}^i\right) + n_0}. \tag{296}$$

---

21. Within a nonmagnetic medium the permeability becomes that of free space, i.e., $\mu \approx \mu_0$, and the index of refraction n and impedance η simplify, such that $n = \sqrt{\varepsilon\mu/(\varepsilon_0\mu_0)} \approx \sqrt{\varepsilon/\varepsilon_0}$ and $\eta = \sqrt{\mu/\varepsilon} \approx \sqrt{\mu_0/\varepsilon}$ (cf. Footnote 2, p. 5) [14].

Note that these approximations are typically valid at optical wavelengths for conducting materials. The analysis explores this validity further in Appendix E below.

Specialization to a perfect electrical conductor

In general, a PEC has infinite conductivity, $\sigma = \infty$, and the tangential electric field becomes zero all along its surface, i.e., $\hat{\mathbf{n}} \times \mathbf{E}^{ext} = 0$ [14]. Based on this knowledge, $r_{\|1,2} = -1$ and $r_{\perp 1,2} = -1$ in Eqs. (290) and (291). This gives rise to a perfectly reflecting surface, and the analysis simplifies even more from that of conductors. For a PEC, only the dyadic $\overleftrightarrow{\mathcal{N}}$ exists within the analysis, i.e., $\overleftrightarrow{\mathcal{L}} = \overleftrightarrow{\mathcal{K}} = \overleftrightarrow{\mathcal{M}} = 0$. Moreover, the dyadic $\overleftrightarrow{\mathcal{N}}$ simplifies [cf. Eq. (274)], such that

$$\begin{aligned} \overleftrightarrow{\mathcal{N}} &= \begin{bmatrix} \mathcal{N}_{xx} & \mathcal{N}_{xy} & \mathcal{N}_{xz} \\ \mathcal{N}_{yx} & \mathcal{N}_{yy} & \mathcal{N}_{yz} \\ \mathcal{N}_{zx} & \mathcal{N}_{zy} & \mathcal{N}_{zz} \end{bmatrix} \\ &= \mathcal{N}_{\mathrm{ij}} \quad (\mathrm{i} = x, y, z;\ \mathrm{j} = x, y, z) \quad , \\ &= \frac{4 \operatorname{sgn}\left(\mathcal{N}_{\mathrm{ij}}\right)}{\vartheta_{z1} \vartheta_{z2}} \sum_{\mathrm{m}=x,u} \sum_{\mathrm{n}=x,u} \Xi^{\mathrm{i}}_{\mathrm{m}1} \Xi^{\mathrm{j}}_{\mathrm{n}2} \Psi_{\mathrm{mn}} \end{aligned} \tag{297}$$

where
$$\operatorname{sgn}\left(\mathcal{N}_{\mathrm{ij}}\right) = \begin{cases} -1 & \text{if } \mathcal{N}_{\mathrm{ij}} = \mathcal{N}_{xy}, \mathcal{N}_{yx}, \mathcal{N}_{yz}, \text{ or } \mathcal{N}_{zy} \\ 1 & \text{otherwise} \end{cases} , \tag{298}$$

$$\Xi^{x}_{x1,2} = \left(\hat{\mathbf{y}} \cdot \hat{\mathbf{v}}\right) \vartheta_{y1,2} + \left(\hat{\mathbf{z}} \cdot \hat{\mathbf{v}}\right) \vartheta_{z1,2} , \tag{299}$$

$$\Xi^{x}_{u1,2} = 0 , \tag{300}$$

$$\Xi^{y}_{x1,2} = \left(\hat{\mathbf{y}} \cdot \hat{\mathbf{v}}\right) \vartheta_{x1,2} , \tag{301}$$

$$\Xi^{y}_{u1,2} = \left[\left(\hat{\mathbf{y}} \cdot \hat{\mathbf{v}}\right)\left(\hat{\mathbf{z}} \cdot \hat{\mathbf{u}}\right) - \left(\hat{\mathbf{y}} \cdot \hat{\mathbf{u}}\right)\left(\hat{\mathbf{z}} \cdot \hat{\mathbf{v}}\right)\right] \vartheta_{z1,2} , \tag{302}$$

$$\Xi^{z}_{x1,2} = -\left(\hat{\mathbf{z}} \cdot \hat{\mathbf{v}}\right) \vartheta_{x1,2} , \tag{303}$$

and $$\Xi^{z}_{u1,2} = \left[\left(\hat{\mathbf{y}} \cdot \hat{\mathbf{v}} \right) \left(\hat{\mathbf{z}} \cdot \hat{\mathbf{u}} \right) - \left(\hat{\mathbf{y}} \cdot \hat{\mathbf{u}} \right) \left(\hat{\mathbf{z}} \cdot \hat{\mathbf{v}} \right) \right] \vartheta_{y1,2} . \tag{304}$$

Note that these assumptions are valid at optical wavelengths for a perfectly conducting material.

Appendix E. Examining the validity of the approximations used when specializing to conductors

The purpose of this appendix is to explore the validity of the approximations made when specializing to conductors. For example, Figure 24 plots the relationships found Eqs. (295) and (296) for a typical in-plane scattering geometry, where $\mathbf{r} = \mathbf{r}_{1,2}$, $\phi^s = 90^\circ$, $\theta^i = 45^\circ$, and $\lambda_0 = 1.064$ μm. The conductors studied in this example are titanium (Ti), aluminum (Al), nickel (Ni), and silver (Ag), which have the following complex indices of refraction: $n_{\mathrm{Ti}} = 3.388 - j3.331$, $n_{\mathrm{Al}} = 1.376 - j10.21$, $n_{\mathrm{Ni}} = 1.376 - j10.21$, and $n_{\mathrm{Ag}} = 0.2342 - j7.214$ [143]. Note that this example maintains average percentage errors much less than one for all of the conductors studied.

Figure 25 shows results for a tactical engagement scenario with anisotropic beam parameters, so that $A_u = A_x$, $B_{xu} = B_{ux} = 0$, $w_s = 2.54/2$ cm, $\ell_{xx} = 0.5w_s$, $\ell_{uu} = 0.25w_s$, $\lambda_0 = 1.064$ μm, $n_{\mathrm{Al}} = 1.376 - j10.21$, $r_s = r_{1,2} = 10$ km, $\theta^i = 45^\circ$, $\ell_h = 100\lambda_0$, and $\sigma_h = 10\lambda_0$. This setup corresponds with unpolarized partially coherent illumination at non-normal incidence of a very rough conducting surface. As such, the approximations leading up to Eqs. (295) and (296) are typically valid when considering the magnitude of the scattered spectral degree of coherence (SDoC) (Figure 25a), the normalized scattered spectral density (SD) (Figure 25b), and the scattered degree of polarization (DoP) (Figure 25c) with conductors. The results displayed here show exact agreement with respect to the scattered SDoC and SD but not the scattered DoP. Thus, as a rule of thumb, one should use the analysis contained in the general problem to avoid errors in the results.

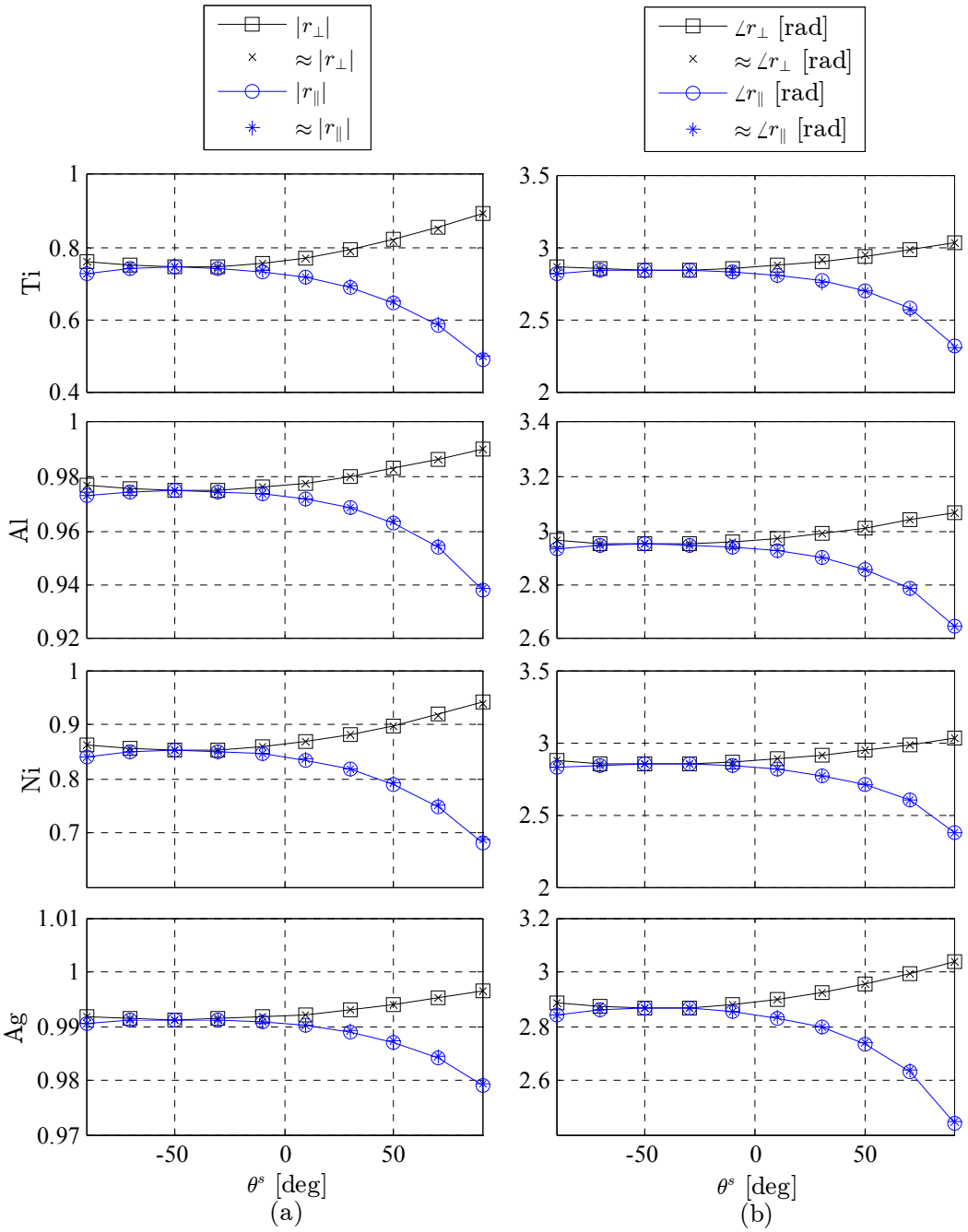

Figure 24. Assessment of the approximations used with the parallel and perpendicular Fresnel reflection coefficients for titanium (Ti), aluminum (Al), nickel (Ni), and silver (Ag). (a) depicts the amplitude, whereas (b) depicts the phase as a function of a single polar angle.

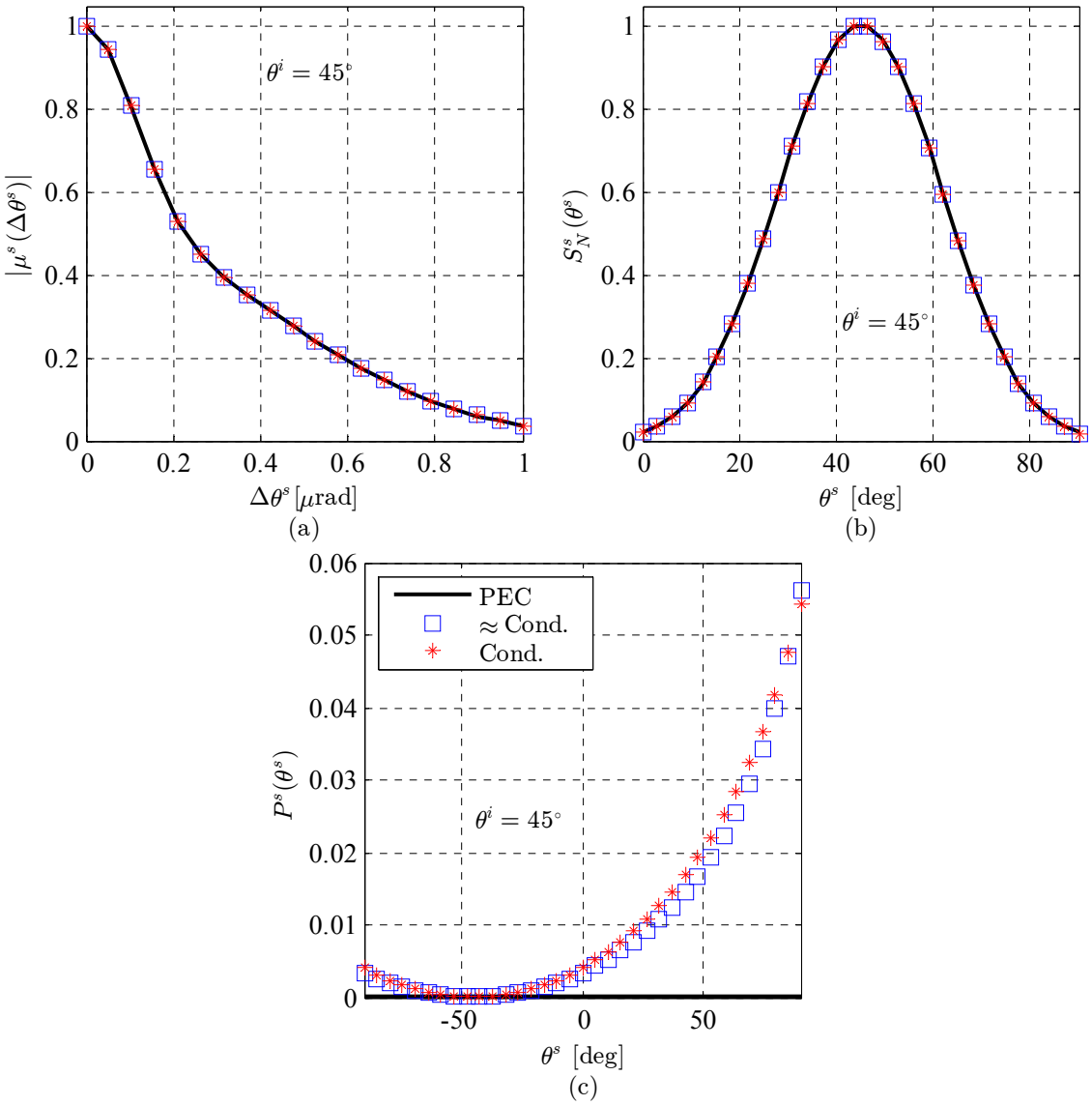

Figure 25. Assessment of the approximations used when specializing to conductors. (a) shows the magnitude of the scattered spectral degree of coherence as a function of the difference between two polar angles, whereas (b) shows the scattered normalized spectral density and (c) shows the scattered degree of polarization as a function of a single polar angle. Note that the analysis includes results for a perfect electrical conductor (PEC) for comparison purposes.

References

1. J. Hecht, "Short History of laser development," Opt. Eng. **49**, 091002 (2010).

2. J. Cook, "High-energy laser weapons since the early 1960s," Opt. Eng. **52**, 021007 (2012).

3. G. A. Perram, S. J. Cusumano, R. L. Hengehold, and S. T. Fiorino, *An Introduction to Laser Weapon Systems*, (Directed Energy Professional Society, 2010).

4. P. Merritt, *Beam Control for Laser Systems*, (Directed Energy Professional Society, 2011).

5. R. A. Motes, S. A. Shakir, and R. W. Berdine, *Introduction to High Power Fiber Lasers, 2nd ed.* (Directed Energy Professional Society, 2013)

6. D. Scott and D. Robie, "Directed Energy A Look into the Future," Air and Space Power Journal **23**, 6-12 (2009).

7. H. D. Kiel, "Is this the time for a high-energy laser weapon program?," Opt. Eng. **52**, 021008 (2012).

8. M. F. Spencer and M. W. Hyde IV, "Rough surface scattering for active-illumination systems," SPIE Newsroom (2013). http://spie.org/x94811.xml

9. M. F. Spencer and M. W. Hyde IV, "The scattering of partially coherent electromagnetic beam illumination from a statistically rough perfectly reflecting surface," Proc. 16th Annual Directed Energy Symposium **13-Symp-089** (2014).

10. M. W. Hyde, S. Basu, S. J. Cusumano and M. F. Spencer, "Scalar wave solution for the scattering of a partially coherent beam from a statistically rough metallic surface," Proc. SPIE **8550** (2012).

11. M.W. Hyde IV, S. Basu, M. F. Spencer, S. J. Cusumano, and S. T. Fiorino, "Physical optics solution for the scattering of a partially-coherent wave from a statistically rough material surface," Opt. Express **21** 6807–6825 (2013).

12. E. Wolf, "Unified theory of coherence and polarization of random electromagnetic beams," Phys. Lett. A **312**, 263-267 (2003).

13. E. Wolf, *Introduction to the Theory of Coherence and Polarization of Light* (Cambridge, 2007).

14. C. A. Balanis, *Advanced Engineering Electromagnetics, 2nd ed.* (Wiley, 2012).

15. S. A. Schelkunoff, "Some equivalence theorems of electromagnetics and their application to radiation problems," Bell Systems Tech. J. **15**, 92-112 (1936).

16. C. Huygens, *Traite de la Lumiere* (Leyeden, 1690).

17. E. Hecht, *Optics, 4th ed* (Addison Wesley, 2002).

18. M. J. Havrilla, "Course Notes for EENG-630 Applications of Electromagnetic Theory (High Frequency Electromagnetics)," Air Force Institute of Technology, Wright Patterson Air Force Base, OH (2005).

19. A. F. Peterson, S. L. Ray and R. Mittra, *Computational Methods for Electromagnetics* (IEEE Press, 1998).

20. B. A. Saleh and M. C. Teich, *Fundementals of Photonics, 2nd ed*. (Wiley, 2007).

21. R. F. Harrington, *Field Computation by Moment Methods* (Macmillan, 1993).

22. P. Beckmann, *The Depolarization of Electromagnetic Waves* (Golem Press, 1968).

23. M. Born and E. Wolf, *Principles of Optics, 7th Expanded ed.* (Cambridge, 2006).

24. J. W. Goodman, *Introduction to Fourier Optics, 3rd ed.*, (Roberts and Company, 2005).

25. T. B. Hansen and A. D. Yaghjian, *Plane-Wave Theory of Time-Domain Fields Near Field Scanning Applications* (IEEE Press, 1999).

26. L. Mandel and E. Wolf, *Optical Coherence and Quantum Optics* (Cambridge, 1995).

27. A. Ishimaru, *Electromagnetic Wave Propagation, Radiation, and Scattering* (Prentice Hall, 1990).

28. I. G. Avramidi, "Lecture Notes on Asymptotic Expansions," New Mexico Insitute of Mining and Technology, Socorro, NM, (2000). http://infohost.nmt.edu/~iavramid/notes/asexp.pdf.

29. J. W. Goodman, *Statistical Optics* (Wiley, 1985).

30. E. Collett, *Polarized Light in Fiber Optics*, (PolaWave Group, 2003).

31. L. Rayleigh, *The Theory of Sound, 2nd ed.* (MacMillan, 1896).

32. L. Rayleigh, "Polish," Nature **64**, 385-388 (1901).

33. L. Rayleigh, "On the dynamical theory of gratings," Proc. of the Royal Soc. A **79**, 399-416 (1907).

34. J. C. Stover, *Optical Scattering Measurements and Analysis, 3rd ed.* (SPIE Press, 2012).

35. F. T. Ulaby, R. K. Moore and A. K. Fung, *Microwave Remote Sensing: Active and Passive* (Artech, 1986).

36. P. Beckmann and A. Spizzichino, *The Scattering of Electromagnetic Waves form Rough Surfaces* (Pergamon Press, 1963).

37. A. Ishimaru, *Wave Propagation and Scattering in Random Media* (Academic Press, 1978).

38. J. A. Ogilvy, *Theory of Wave Scattering From Random Rough Surfaces*, (IOP, 1991).

39. A. G. Voronovich, *Wave Scattering from Rough Surfaces, 2nd. ed*. (Springer, 1999).

40. K. F. Warnick and W. C. Chew, "Numerical simulation methods for rough surface scattering," Waves Random Media **11**, R1-R30 (2001).

41. T. M. Elfouhaily and C.-A. Guérin, "A critical survey of approximate scattering wave theories from random rough surfaces," Waves Random Media **14**, R1-R40 (2004).

42. M. Nieto-Vesperinas, *Scattering and Diffraction in Physical Optics, 2nd ed*. (World Scientific, 2006).

43. A. A. Maradudin, ed., *Light Scattering and Nanoscale Surface Roughness* (Springer, 2007).

44. A. K. Fung and K. S. Chen, *Microwave Scattering and Emission Models for Users* (Artech, 2010).

45. F. E. Nicodemus, "Reflectance nomenclature and directional reflectance and emissivity," Appl. Opt. **9**, 767-773 (1965).

46. M. W. Hyde, J. D. Schmidt and M. J. Havrilla, "A geometrical optics polarimetric bidirectional reflectance distribution function for dielectric and metallic surfaces," Opt. Express **17**, 22138-22153 (2009).

47. B. W. Hapke, "A theoretical photometric function for the lunar surface," J. Geophys. Res. **68**, 349–364 (1963).

48. K. E. Torrance and E. M. Sparrow, "Theory for off-specular reflection from roughened surfaces," J. Opt. Soc. Am. **57**, 1105–1114 (1967).

49. R. G. Priest and S. R. Meier, "Polarimetric microfacet scattering theory with applications to absorptive and reflective surfaces," Opt. Eng. **41**, 988–993 (2002).

50. M. W. Hyde, "Determining the Index of Refraction of an Unknown Object using Passive Polarimetric Imagery Degraded by Turbulence," PhD Dissertation, Air Force Institute of Technology, Wright Patterson Air Force Base, OH (2010). www.dtic.mil/cgi-bin/GetTRDoc?AD=ADA526413

51. X. D. He, K. E. Torrance, F. X. Sillion and D. P. Greenberg, "A comprehensive physical model for light reflection," SIGGRAPH Comp.Graphics **25**, 175-186, (1991).

52. Y. Sun, “Statistical ray method for deriving reflection models of rough surfaces,” J. Opt. Soc. Am. A **24**, 724–744 (2007).

53. J. E. Harvey and R. V. Shack, “Light-Scattering Characteristics of Optical Surfaces,” Technical Report, Optical Sciences Center, University of Arizona, Tucson, AZ (1975). http://www.dtic.mil/dtic/tr/fulltext/u2/a095132.pdf

54. J. E. Harvey and R. V. Shack, “Aberrations of diffracted wave fields,” App. Opt. **17**, 3003-3009 (1978).

55. J. E. Harvey, “Fourier treatment of near-field scalar diffraction theory,” Am. J. Phys. **47**, 974-980 (1979).

56. J. E. Harvey, E. C. Moran and W. P. Zmek, “Transfer function characterization of grazing incidence optical systems,” Applied Optics **27**, 1527-1533 (1988).

57. A. Krywonos, “Predicting Surface Scatter Using a Linear Systems formulation of Non-Paraxial Scalar Diffraction,” PhD Dissertation, College of Optics and Photonics, University of Central Florida, Orlando, FL (2006). http://etd.fcla.edu/CF/CFE0001446/Krywonos_Andrey_200612_PhD.pdf

58. A. Krywonos, J. E. Harvey and N. Choi, “Linear systems formulation of scattering theory for rough surfaces with arbitrary incident and scattering angles,” J. Opt. Soc. Am. A **28**, 1121-1138 (2011).

59. N. Choi and J. E. Harvey, “Image degradation due to surface scatter in the presence of aberrations,” Applied Optics **51**, 535-546 (2012).

60. J. E. Harvey, “Parametric analysis of the effect of scattered light upon the modulation transfer function,” Opt. Eng. **52**, 073110 (2013).

61. N. Choi and J. E. Harvey, “Numerical validation of the generalized Harvey-Shack surface scatter theory,” Opt. Eng. **52**, 115103 (2013).

62. S. O. Rice, “Reflection of electromagnetic wave by slightly rough surfaces,” Commun. Pure Appl. Mathematics **4**, 351-378 (1951).

63. D. R. Jackson, D. P. Winebrenner and A. Ishimaru, “Comparison of perturbation theories for rough-surface scattering,” J. Acoust. Soc. Am. **83**, 961-969 (1988).

64. M. E. Knotts, T. R. Michel and K. A. O'Donnell, “Angular correlation functions of polarized intensities scattered from a one-dimensionally rough surface,” J. Opt. Soc. Am. A **9**, 1822-1831 (1992).

65. R. E. Collin, “Scattering of an Incident Gaussian Beam by a Perfectly Conducting Rough Surface,” IEEE Trans. Antennas Propag. **42**, 70-74 (1994).

66. A. Ishimaru, C. Le, Y. Kuga, L. A. Sengers and T. K. Chan, “Polarimetric scattering theory for high slope rough surfaces," Prog. Electromagn. Res. **14**, 1-36 (1996).

67. G. Guo, S. Li and Q. Tan, "Statistical Properties of Laser Speckles Generated from Far Rough Surfaces," Int. J. Infrared and Millimeter Waves **22**, 1177-1191 (2001).

68. M. J. Wang, Z. S. Wu and Y. L. Li, "Investigation of the scattering characteristics of Gaussian beam from two dimensional dielectric rough surfaces based on the Kirchhoff approximation," Prog. Electromagn. Res. B **4**, 223-235 (2008).

69. A. Taflove and S. C. Hagness, *Computational Electrodynamics the Finite-Difference Time-Domain Method, 3rd ed.* (Artech House Publishers, 2005).

70. A. Elsherbeni and V. Demir, *The Finite Difference Time Domain Method for Electromagnetics: With MATLAB Simulations*, (SciTech Publishing, Inc., 2009).

71. J. L. Volakis, A. Chatterjee and L. C. Kempel, *Finite Element Method Electromagnetics: Antennas, Microwave Circuits, and Scattering Applications* (IEEE Press, 1998).

72. J. Jin, *The Finite Element Method in Electromagnetics* (Wiley, 2002).

73. E. Bahar, "Coupling Between Guided Surface Waves, Lateral-Waves, and the Radiation Fields by Rough Surfaces-Full Wave Solutions," IEEE Trans. Microwave Theory and Techniq. **25**, 923-931 (1977).

74. E. Bahar, "Full Wave and Physical Optics Solutions for Scattered Radiation Fields by Rough Surfaces-Energy and Reciprocity Relationships," IEEE Trans. Antennas and Propag. **26**, 603-614 (1978).

75. E. Bahar, "Full-Wave Solutions of the Scattered Radiation Fields from Rough Surfaces with Arbitrary Slope and Frequency," IEEE Trans. Antennas Propag. **28**, 11-21 (1980).

76. E. Bahar, "Full-Wave Solutions for the Depolarization of the Scattered Radiation Fields by Rough Surfaces of Arbitrary Slope," IEEE Trans. Antennas Propag. **29**, 443-454 (1981).

77. R. Axline and A. K. Fung, "Numerical Computation of Scattering from a Perfectly Conducting Random Surface," IEEE Trans. Antennas Propag. **26,** 482-488 (1978).

78. E. I. Thorsos, "The validity of the Kirchhoff approximation for rough surface scattering using a Gaussian roughness spectrum," J. Accoust. Soc. Am. **83**, 78-92 (1988).

79. R. E. Collin, "Electromagnetic Scattering from Perfectly Conducting Rough Surfaces (A New Full Wave Method)," IEEE Trans. Antennas Propag. **40**, 1466-1477 (1992).

80. R. E. Collin, "Electromagnetic Scattering from Perfectly Conducting Rough Surfaces (A New Full Wave Method)," IEEE Trans. Antennas and Propag. **40**, pp. 1466-1477 (1992).

81. R. E. Collin, “Full wave theories for rough surface scattering: An updated assesment,” Radio Science **29**, 1237-1254 (1994).

82. R. B. Holmes, “Mean and variance of energy reflected from a diffuse object illuminated by radiation with partial temporal coherence,” J. Opt. Soc. Am. A **20**, 1194-1200 (2003).

83. D. J. Wheeler and J D. Schmidt, “Coupling of Gaussian Schell-model beams into single-mode optical fibers,” J. Opt. Soc. Am. A **28**,1224-1238 (2011).

84. G. A. Tyler, “Accommodation of speckle in object-based phasing,” J. Opt. Soc. Am. A **29**, 722-733 (2012).

85. M. W. Hyde, A. E. Bogle, and M. J. Havrilla, “Scattering of a partially-coherent wave from a material circular cylinder,” Opt. Express **21**, 32327-32339 (2013).

86. J. Dainty, “Some statistical properties of random speckle patterns in coherent and partially coherent illumination,” Optica Acta **17**, 761-772 (1970).

87. H. Fujii and T. Asakura, “A contrast variation of image speckle intensity under illumination of partially coherent light,” Opt. Commun. **12**, 32–38 (1974).

88. H. Fujii and T. Asakura, “Statistical properties of image speckle patterns in partially coherent light,” Nouvelle Revue d'Optique **6**, 5-14 (1975).

89. H. M. Pedersen, “The roughness dependence of partially developed, monochromatic speckle patterns,” Opt. Commun. **12**, 156–159 (1974).

90. J. W. Goodman, “Statistical properties of laser speckle patterns,” in “Laser Speckle and Related Phenomena,” vol. 9 of *Topics in Applied Physics*, J. C. Dainty, ed. (Springer-Verlag, 1975, p. 9–75).

91. G. Parry, “Speckle patterns in partially coherent light,” in “Laser Speckle and Related Phenomena,” vol. 9 of *Topics in Applied Physics*, J. C. Dainty, ed. (Springer-Verlag, 1975, p. 77–121).

92. T. Yoshimura, K. Kato and K. Nakagawa, “Surface-roughness dependence of the intensity correlation function under speckle-pattern illumination,” J. Opt. Soc. Am. A **7**, 2254–2259 (1990).

93. J. W. Goodman, *Speckle Phenomena in Optics: Theory and Applications* (Roberts and Company, 2007).

94. A. C. Schell, “The multiple plate antenna,” PhD Dissertation, Massachusetts Institute of Technology, Cambridge, MA (1961). http://dspace.mit.edu/bitstream/handle/1721.1/35013/31850641.pdf?sequence=1

95. A. C. Schell, “A technique for the determination of the radiation pattern of a partially coherent aperture,” IEEE Trans Antennas Prop. **15**, 187-188 (1967).

96. O. Korotkova, M. Salem and E. Wolf, "Beam conditions for radiation generated by an electromagnetic Gaussian Schell-model source," Opt. Lett. **29**, 1173-1175 (2004).

97. H. Roychowdhury and O. Korotkova, "Realizability conditions for electromagnetic Gaussian Schell-model sources," Opt. Commun. **249**, 379–385 (2005).

98. F. Gori, M. Santarsiero, R. Borghi, V. Ramirez-Sanchez, "Realizability conditions for electromagnetic Schell-model sources," J. Opt. Soc. Am. A **25**, 1016-1021 (2008).

99. G. G. F. Piquero, P. Romanini, M. Santarsiero, R. Borghi and A. Mondello, "Synthesis of partially polarized Gaussian Schell-model sources," Opt. Commun. **208**, 9-16 (2002).

100. T. Leskova, A. A. Maradudin and J. Munoz-Lopez, "The design of one-dimensional randomly rough surfaces that act as Collett–Wolf sources," Opt. Commun. **26,** 123-133 (2004).

101. T. Shirai, O. Korotkova and E. Wolf, "A method of generating electromagnetic Gaussian Schell-model beams," J. Opt. A: Pure Appl. Opt. **7**, 232-237 (2005).

102. G. J. Gbur, "Simulating fields of arbitrary spatial and temporal coherence," Opt. Express **14**, 7567-7578 (2006).

103. X. Xiao and D. Voelz, "Wave optics simulation approach for partial spatially coherent beams," Opt. Express **14**, 6986-6992 (2006).

104. D. J. Wheeler and J. D. Schmidt, "Spatial coherence function of partially coherent Gaussian beams in atmospheric turbulence," Appl. Opt. **50**, 3907-3917 (2011).

105. O. Korotkova, B. G. Hoover, V. L. Gamiz and E. Wolf, "Coherence and polarization properties of far-fields generated by quasi-homogeneous electromagnetic sources," J. Opt. Soc. Am. A **22**, 2547-2556 (2005).

106. O. Korotkova and E. Wolf, "Changes in the state of polarization of a random electromagnetic beam on propagation," Opt. Commun. **246**, 35-43 (2005).

107. O. Korotkova, T. D. Visser and E. Wolf, "Polarization properties of stochastic electromagnetic beams," Opt. Commun. **281**, 515–520 (2007).

108. O. Korotkova, L. C. Andrews and R. L. Phillips, "Model for a partially coherent Gaussian beam in atmospheric turbulence with application in lasercom," Opt. Eng. **43**, 330-341 (2004).

109. M. Salem, O. Korotkova, A. Dogariu and E. Wolf, "Polarization changes in partially coherent electromagnetic beams propagating through turbulent atmosphere," Wave Random Media **14**, 513–523 (2004).

110. O. Korotkova, M. Salem, A. Dogariu and E. Wolf, "Changes in the polarization ellipse of random electromagnetic beams propagating through the turbulent atmosphere," Wave Random Media **5**, 353-364 (2005).

111. O. Korotkova, S. Sahin and E. Shchepakina, "Multi-Gaussian Schell-model beams," J. Opt. Soc. Am. A, **29**, 2159-2164 (2012).

112. Z. Tong and O. Korotkova, "Electromagnetic nonuniformly correlated beams," J. Opt. Soc. Am. A **29**, 2154-2158 (2012).

113. A. Maradudin, E. Mendez, T. Leskova, *Designer Surfaces* (Elsevier, 2008).

114. G. Gbur and T. D. Visser, "The Structure of Partially Coherent Fields," Progress in Optics **55**, 285-341 (2010).

115. O. Korotkova, *Random Light Beams: Theory and Applications* (CRC Press, 2013).

116. W. H. Carter and E. Wolf, "Scattering from quasi-homogeneous media," Opt. Commun. **67**, 85-90 (1988).

117. E. Wolf, J. T. Foley and F. Gori, "Frequency shifts of spectral lines produced by scattering from spatially random media,"J. Opt. Soc. Am. A **6**, 1142-1149 (1989).

118. F. Gori, C. Palma and M. Santarsiero, "A scattering experiment with partially coherent light," Opt. Commun. **74**, 353–356 (1990).

119. D. G. Fischer and E. Wolf, "Inverse problems with quasi-homogeneous random media," J. Opt. Soc. Am. A **11**, 1128-1135 (1994).

120. T. Shiraia and T. Asakura, "Multiple light scattering from spatially random media under the second-order Born approximation," Opt. Commun. **123**, 234-249 (1996).

121. A. Dogariu and E. Wolf, "Spectral changes produced by static scattering on a system of particles," Opt. Lett. **23**, 1340-1342 (1998).

122. G. Gbur and E. Wolf, "Determination of density correlation functions from scattering of polychromatic light," Opt. Commun. **168**, 39–45 (1999).

123. T. D. Visser, D. G. Fischer and E. Wolf, "Scattering of light from quasi-homogeneous sources by quasi-homogeneous media," J. Opt. Soc. Am. A **23**, 1631-1638 (2006).

124. J. Li, Y. Chen, S. Xu, Y. Wang, M. Zhou, Q. Zhou, Y. Xin and F. Chen, "Condition for invariant spectral degree of coherence of an electromagnetic plane wave on scattering," Opt. Commun. **284**, 724–728 (2011).

125. T. Wang and D. Zhao, "Stokes parameters of an electromagnetic light wave on scattering," Opt. Commun. **285**, 893-895 (2012).

126. D. Zhao and T. Wang, "Direct and Inverse Problems in the Theory of Light Scattering," Progress in Optics **57**, 261-308 (2012).

127. B. G. Hoover and V. L. Gamiz, "Coherence solution for bidirectional reflectance distributions of surfaces with wavelength-scale statistics," J. Opt. Soc. Am. A **23**, 314-328 (2006).

128. L. C. Andrews and R. L. Phillips, *Laser beam propagation through random media* (SPIE Press, 2005).

129. O. Korotkova, *Partially Coherent Beam Propagation in Turbulent Atmosphere with Applications*, (VDM Verlag, 2009).

130. R. S. Hansen, H. T. Yura and S. G. Hanson, "First-order speckle statistics: an analytic analysis using ABCD matrices," J. Opt. Soc. Am. A **14**, 3093-3098 (1997).

131. H. Yura and S. G. Hanson, "Variance of intensity for Gaussian statistics and partially developed speckle in complex ABCD optical systems," Opt. Commun. **228**, 263-270 (2003).

132. G. Wu and Y. Cai, "Detection of a semirough target in turbulent atmosphere by a partially coherent beam," Opt. Lett. **36**, 1939-1941 (2011).

133. Y. Cai, O. Korotkova, H. T. Eyyuboglu, and Y. Baykal, "Active laser radar systems with stochastic electromagnetic beams in turbulent atmosphere," Opt. Exp. **16**, 15834-46 (2008).

134. O. Korotkova, Y. Cai, and E. Watson, "Stochastic electromagnetic beams for LIDAR systems operating through turbulent atmosphere," Appl. Phys. B **94**, 681-690.

135. S. Sahin, Z. Tong, O. Korotkova, "Sensing of semi-rough targets embedded in atmospheric turbulence by means of stochastic electromagnetic beams," Opt. Commun. **283**, 4512-4518 (2010).

136. A. S. Ostrovsky, *Coherent-Mode Representations in Optics* (SPIE Press, 2006).

137. J. Huttunen, A. T. Friberg and J. Turunen, "Scattering of partially coherent electromagnetic fields by microstructured media," Phys. Rev. E **52**, 3081-3092 (1995).

138. C. A. Mack, "Analytic form for the power spectral density in one, two, and three dimensions," J. Micro/Nanolithogr. MEMS MOEMS **10**, 040501 (2011).

139. S. Basu, M. W. Hyde IV, S. J. Cusumano, M. A. Marciniak, and S. T. Fiorino, "Validity of using a Gaussian Schell model for extended beacon studies," Proc. SPIE **8380** (2012).

140. S. Basu, M. W. Hyde IV, S. J. Cusumano, M. A. Marciniak, and S. T. Fiorino, "Examining the validity of using Gaussian Schell-model source to model the

scattering of a fully coherent Gaussian beam from a rough impedance surface," Opt. Eng. **52**, 038001 (2012).

141. S. Chatterjee, V. C. Vani, and R. K. Banyal, "Intensity profile of light scattered from a rough surface," Appl. Opt. **52**, 6000-6010 (2013).

142. LabSphere, Inc., "A Guide to reflectance coatings and materials" (LabSphere, Inc., 2012). http://www.labsphere.com/uploads/technical-guides/a-guide-to-reflectance-materials-and-coatings.pdf

143. M. N. Polyanskiy, "Refractive index database" (RefractiveIndex.Info, 2014). http://refractiveindex.info

144. KLA-Tencor Corporation, "Alpha-step IQ Surface Profiler" (KLA-Tencor Corporation, 2012). http://www.kla-tencor.com/surface-profiling/alpha-step-iq.html

145. H. T. Yura and S. G. Hanson, "Digital simulation of an arbitrary stationary stochastic process by spectral representation," J. Opt. Soc. Am. A **28**, 675-685 (2011).

146. J. C. Vap, S. E. Nauyoks, and M. A. Marciniak, "Optimization of a dual-rotating-retarder polarimeter as applied to a tunable infrared Mueller-matrix scatterometer," Meas. Sci. Technol. **24**, 055901 (2013).

147. D. H. Goldstein, *Polarized Light, 3rd ed.* (CRC Press, 2012).

148. T. A. Germer amd C. C. Asmail, "Goniometric optical scatter instrument for out-of-plane ellipsometry measurements," Rev. Sci. Instrum. **70**, 3688-3695 (1999).

149. T. Voipio, T. Setala, and A. T. Friberg, "Partial polarization theory of pulsed optical beams," J. Opt. Soc. Am. A **30**, 71-81 (2013).

150. M. J. Kim, J. C. Dainty, A. T. Friberg, and A. J. Sant, "Experimental study of enhanced backscattering from one- and two-dimensional random rough surfaces," J. Opt. Soc. Am. A **7**, 569-577 (1990).

REPORT DOCUMENTATION PAGE

Form Approved
OMB No. 0704–0188

1. REPORT DATE (DD–MM–YYYY)	2. REPORT TYPE	3. DATES COVERED *(From — To)*
19-06-2014	Dissertation	March 2011 – June 2014

4. TITLE AND SUBTITLE
The Scattering of Partially Coherent Electromagnetic Beam Illumination from Statistically Rough Surfaces

5a. CONTRACT NUMBER
5b. GRANT NUMBER
5c. PROGRAM ELEMENT NUMBER

6. AUTHOR(S)
Spencer, Mark, F., Mr.

5d. PROJECT NUMBER
JON 14G451A
5e. TASK NUMBER
5f. WORK UNIT NUMBER

7. PERFORMING ORGANIZATION NAME(S) AND ADDRESS(ES)
Air Force Institute of Technology
Graduate School of Engineering and Management (AFIT/EN)
2950 Hobson Way
Wright-Patterson AFB OH 45433-7765

8. PERFORMING ORGANIZATION REPORT NUMBER
AFIT-ENG-DS-14-J-7

9. SPONSORING / MONITORING AGENCY NAME(S) AND ADDRESS(ES)
Air Force Office of Scientific Research
Julie Moses
875 N Randolph St.
Arlington, VA 22203
(703) 696-9586, julie.moses@us.af.mil

10. SPONSOR/MONITOR'S ACRONYM(S)
AFOSR/RTB
11. SPONSOR/MONITOR'S REPORT NUMBER(S)

12. DISTRIBUTION / AVAILABILITY STATEMENT
Distribution Statement A. Approved for Public Release; Distribution Unlimited

13. SUPPLEMENTARY NOTES

14. ABSTRACT
Much of the rough surface scattering theory developed to date considers only the effects of fully coherent and fully incoherent illumination in the formation of solutions—a problem studied in earnest since the late 1800's. In response, this dissertation extends the theory currently available in modeling rough surface scattering to include the effects of partially coherent illumination. Such illumination plays a pivotal role in our understanding of active-illumination systems, similar to those found in directed-energy and remote-sensing applications, which use the light scattered from distant targets for tactical purposes. Specifically, this dissertation uses the physical optics approximation (Kirchhoff boundary conditions) to determine a 3D vector solution for the far-field scattering of electromagnetic beam illumination with partial spatial coherence from statistically rough surfaces. The analysis considers three different material substrates: dielectrics, conductors, and a perfect electrical conductor. It also makes use of a Gaussian Schell-model form for the incident-field cross-spectral density matrix. In so doing, this dissertation develops closed-form expressions for the scattered field cross-spectral density matrix with two analytical forms—one applicable to smooth-to-moderately rough surfaces and the other applicable to very rough surfaces. The analysis shows that these closed-form expressions are, in general, complicated functions of both the source (size and coherence properties) and surface parameters (surface height standard deviation and correlation length). Under appropriate conditions, the analysis also compares the 3D vector solution to previously validated solutions and empirical measurements. The results show good agreement.

15. SUBJECT TERMS
Rough Surface Scattering, Coherence Theory, Statistical Optics, Electromagnetics, Gaussian Schell-Model Form

16. SECURITY CLASSIFICATION OF:			17. LIMITATION OF ABSTRACT	18. NUMBER OF PAGES	19a. NAME OF RESPONSIBLE PERSON
a. REPORT	b. ABSTRACT	c. THIS PAGE	UU	153	Milo W. Hyde IV, Maj, USAF, PhD, AFIT/ENG
U	U	U			19b. TELEPHONE NUMBER (Include Area Code) (937) 255-3636 x 4371; milo.hyde@afit.edu